UNIVERSITY OF CALIFORNIA

Santa Barbara

Bioinspired Assembly of Functional Polymers into Well-Defined Materials

A dissertation submitted in partial satisfaction of the
requirements for the degree Doctor of Philosophy
in Materials

by

Cynthia Xin Yi Wang

Committee in charge:

Professor Craig J. Hawker, Chair

Professor Glenn H. Fredrickson

Professor Michael L. Chabinyc

Professor Omar A. Saleh

June 2016

The dissertation of Cynthia Xin Yi Wang is approved.

Michael L. Chabinyc

Glenn H. Fredrickson

Omar A. Saleh

Craig J. Hawker, Committee Chair

May 2016

Bioinspired Assembly of Functional Polymers into Well-Defined Materials

ACKNOWLEDGEMENTS

To begin, I thank my advisor, Professor Craig Hawker for his guidance, patience, and steadfast support over years. I am also grateful to my committee for their valuable insight and time, Professors: Glenn Fredrickson, Michael Chabinyc, and Omar Saleh, as well as previous members of my committee, Professors: Tom Soh, Ed Kramer and Javier Read de Alaniz.

My research would not have been possible without the support of the Hawker Lab, collaborators in the Soh and Morse Lab, CNSI staff and MRL staff. I am indebted to Daniel Klinger, our project leader who advocated my work and pushed me to grow. Thank you to: Stephan Kraemer who was instrumental in all the nanofootball related microscopy and elemental analysis; Stefanie Utech and Chrysafis Andreou, for their microfluidic tutelage; Bernie Schmidt, Jeff Gopez and Matt Menyo for fluffy, purified polymers; Peter Mage and Faye Fong for sharing their microscope; as well as Pontus Lundberg, Eric Pressly, Se Gyu Jang and Nate Lynd for showing me the ropes (and Schlenk lines) when I first arrived.

I'm going to miss the incredible work environment at UCSB. I had the privilege to share a lab with the awesome PSBN crew and work alongside diligent students, Tyler Brown, Isabel Arias, Ashley Davalos, Phillip Hicks, and Brigitte Lamers. My immense gratitude to many colleagues: Frank, Revital, Jimmy, Christian, Abby, Jia, David, Nic, Yingdong, for their advice and time. To Kaila, thank you for brightening up our workspace with your orchids, mint plant, and sunny outlook. Sharing an office with Mathijs, Satoshi, and Abi was just as wonderful. Finally, to my friends and family, thank you for keeping me afloat when I felt unmoored by graduate school and for celebrating my personal victories. -C

Curriculum Vitae

Cynthia Xin Yi Wang

Education

2011–2016	Ph.D., Materials, University of California, Santa Barbara Advisor: Craig J. Hawker
2007–2011	B.S., Bioengineering, University of California, Los Angeles

Professional Employment

2011–2016	Graduate Student Researcher University of California, Santa Barbara Advisor: Craig J. Hawker
2012	Summer Visiting Researcher Washington University, St. Louis Advisor: Yongjian Liu
2011	Teaching Assistant University of California, Santa Barbara Instructor: Ram Seshadri
2009–2011	Undergraduate Researcher University of California, Los Angeles Advisor: Andrea M. Kasko
2007, 2008	Summer Intern Intel Corporation, Folsom, CA

Publications

Wang, C. X.; Utech, S.; Gopez, J. D.; Mabesoone, M. F. J.; Hawker, C. J.; Klinger, D. "Non-Covalent Microgel Particles Containing Functional Payloads: Coacervation of PEG-Based Triblocks via Microfluidics." *ACS Appl. Mater. Interfaces*, **2016**, *8*, 16914–16921.

Wang, C. X.; Braendle, A.; Menyo, M. S.; Pester, C. W.; Perl, E. E.; Arias, I.; Hawker, C. J.; Klinger, D. "Catechol-based layer-by-layer assembly of composite coatings: a versatile platform to hierarchical nano-materials," *Soft Matter*, **2015**, *11*, 6173–6179.

Klinger, D.; **Wang, C. X**.; Connal, L. A.; Audus, D. J.; Jang, S. G.; Kraemer, S.; Killops, K. L.; Fredrickson, G. H.; Kramer, E. J.; Hawker, C. J. "A Facile Synthesis of Dynamic, Shape-Changing Polymer Particles," *Angewandte Chemie International Edition,* **2014**, *53*, 7018–22.

Luehmann, H. P.; Pressly, E. D.; Detering, L.; **Wang**, C.; Pierce,R.; Woodard, P. K.; Gropler, R. J.; Hawker, C. J.; Liu, Y. "PET/CT Imaging of Chemokine Receptor CCR5 in Vascular Injury Model Using Targeted Nanoparticle," *Journal of Nuclear Medicine*, **2014**, *55*, 629–634.

ABSTRACT

Bioinspired Assembly of Functional Polymers into Well-Defined Materials

by

Cynthia X. Wang

From the robust underwater adhesion of marine mussels to rapid camouflage in cephalopods, the chemical and structural motifs found in marine organisms are instructive for rational design of synthetic nanomaterials. This dissertation describes the development of three bioinspired assembly methods of synthetic copolymers into hierarchically structured constructs for photonic and therapeutic applications.

First, a catechol-based dip coating platform has been developed for the facile preparation of composite films from aqueous solutions. The sequential layer-by-layer assembly of a mussel inspired polymeric binder with oxide nanoparticles — SiO_2 and TiO_2 — utilizes the exceptional adhesion properties of catechol moieties. This modular assembly of well-defined building blocks demonstrates tunability over film thickness and refractive indices, enabling the preparation of multilayered optical coatings such as Bragg stacks.

To prepare responsive, internally structured particles for photonic applications, block copolymers (BCPs) were assembled in droplets. In this system, pH responsive ellipsoidal particles were designed to emulate the structure of the light reflective cells used by squid for

dynamic coloration. Functional surfactants were used to direct the assembly of lamellar forming polystyrene-*b*-poly(2-vinylpyridine) (PS-P2VP) within emulsion droplets to achieve axially stacked lamellae after solvent evaporation. Selective cross-linking of the P2VP domain leads to pH sensitive hydrogel domains connecting glassy PS discs. This ability to tune the refractive index contrast between the two alternating BCP domains, suggests progress towards colloidal Bragg reflectors for photonic materials.

In the final system, well-defined microgels were produced using a microfluidic device in combination with coacervate-driven crosslinking of poly(ethylene-oxide) based ionic triblock copolymers. This strategy enables the additional incorporation of charged cargo into the microgel. When the payload functional group and the microgel dimensions are varied, distinct cargo release profiles are observed. This mild and non-covalent assembly method represents a promising new approach to produce tunable BCP microgels as scaffolds for colloidal biomaterials in therapeutics and regenerative medicine.

TABLE OF CONTENTS

LIST OF FIGURES

1 Introduction

The exciting physical properties that arise from the confinement of material into nanoscale dimensions have led to many technological breakthroughs. For instance, quantum dots for brighter, sleeker displays[1] and hemostatic aluminosilicate nanoparticles in Quikclot gauze.[2] Over the past two decades, dispersed nanoparticles have been introduced into many commercial products: from silver zeolite in antimicrobial food packaging[3] to carbon nanotube reinforced bicycle frames.[4] In order to achieve next generation therapeutics, communication devices, and alternative energy platforms, it is necessary to shift colloidal nanomaterials from their current role as dispersed additives within a bulk phase (e.g. packaging, sunscreen) into dynamic, hierarchically structure systems.

To address this need, the development of new colloidal assembly methods along with the fabrication of modular synthetic building blocks is essential. The scientific community has long strived for well-defined colloidal materials in terms of composition, geometry, and surface properties. While solution based colloidal synthetic methods have enabled access to increasingly intricate nanostructures,[1,5] however, most engineering capabilities remain far from the level of precision of cellular machinery within living systems. Drawing from biological structural and chemical motifs, material scientists have the opportunity to fabricate bioinspired materials[6] through new material combinations that may not be accessible to natural systems.

The self-organizing structural elements used by living systems to assemble complex architectures and integrate function over multiple length scales[6,7] may provide insight to better engineer thin films and nanoparticles for advanced materials. Controlled materials assembly with long range periodicity is especially relevant for photonic applications, medical diagnostics, and tissue engineering.[8] To fulfill these needs, synthetic polymeric materials serve as ideal building block for dynamic hierarchically structured assemblies due to their chemical versatility, ease of (solution based) processing, and ability to self-assemble on the nanoscale.[9]

This dissertation describes the development of new bioinspired methods for interfacial engineering and assembly of polymers into composite coatings and responsive colloids.

1.1 Structural color

Photonic crystals involve periodic arrangements of matter in which light is selectively reflected or propagated through interactions with a dielectric material. Constructive interference of specific wavelengths of light by photonic crystals results in iridescence or opalescence also referred to as structural color. This is in contrast to the mechanism of color for pigments (or dyes) in which absorption of specific light wavelengths lead to the transmission and reflection (or emission) of the complementary hue.

Photonic crystals can be divided into three main classes based on their degree of confinement (1D, 2D and 3D crystals) which are relevant for optical coatings, waveguides and angle independent display applications respectively. Another key concept for understanding the assembly criteria for synthetic photonic films and colloids is the optics of Bragg reflectors (1D photonic crystals).

1.1.1 Bragg stacks

Bragg stacks are the simplest example of one dimensional (1D) periodic variation in dielectric media consisting of alternating layers of high and low refractive index material. The optical thickness of each layer (product of the refractive index, *n*, and thickness, *d*, of each layer) determines the wavelength of reflected light. And the first-order reflected wavelength, λ_{max}, for a Bragg stack is given by Eqn 1:[10]

$$\lambda_{max} = 2\,(n_L d_L + n_H d_H) \qquad (1)$$

The refractive index contrast between the layers influences the amount of incident light reflected at each interface between the layers. The reflectivity, R, also increases with the number of bilayers (N), as shown in Eqn 2:[11]

$$R = \left[\frac{n_o - n_S\left(n_L/n_H\right)^{2N}}{n_o + n_S\left(n_L/n_H\right)^{2N}}\right]^2 \qquad (2)$$

where n_o denotes the refractive index of the surrounding environment (initial media) and n_S of the substrate or backing of the Bragg stack film.

These relationships enable predictive design of dynamic Bragg stacks[12] that would be valuable for many applications ranging from environmental sensing[13] to switchable displays.[14] Bragg stack films with switchable optical response have been demonstrated via infiltration of solvent[15] or selective adsorption/desorption of analyte into porous inorganic TiO_2/SiO_2 layers

While polymeric Bragg stacks offer more opportunities to incorporate stimuli-responsive functional groups or networks,[16] one disadvantage of these materials is the low refractive index contrast for most organic precursors. Many bilayers are typically required to achieve high reflectance intensity. For this reason, inorganic fillers with high refractive index are added to enhance the refractive index contrast. However, blending these two disparate components into a uniform film creates additional processing challenges to overcome such as aggregation of nanoparticles. The development of a modular and simple strategy to assemble well-defined hybrid Bragg stacks would be very valuable. Natural examples of structural colors in nature may provide instructive design principles for rational design of photonic materials from synthetic building blocks.

1.1.2 Dynamic intracellular Bragg stacks in squid

Living organisms have evolved the ability to manipulate light and color through hierarchically structured assemblies.[17] Iridophore cells[18] in cephalopods are one notable example. To survive the open waters, cephalopods such as the mimic octopus, cuttlefish and squid, may disguise themselves to blend into their surroundings or signal aggression toward predators.[18,19] In particular, squid skin contains iridophore cells that consists of high refractive index protein platelets layers alternating with low refractive index extracellular matrix. The reversible condensation of recombinant reflectin protein and tunable optical response of iridophores to chemical stimuli by Morse and co workers demonstrates the potential for self-assembly of “soft optical materials”.[18]

1.2 Thin film coatings

Coatings provide a simple route to dramatically alter surface properties. Illustrative examples include the stain repellent properties of fabric sprayed with scotch guard and high clarity spectacles lenses coated with a layer of antireflective oxide. The lifetime and performance of such coatings are determined by the mechanical integrity and tunability of the coating components. While inorganic coatings provide more impermeable barriers than polymeric coatings, these are more susceptible to brittle fracture[20] and often require complex equipment such as a chemical or physical vapor deposition chambers.[21] In order to produce flexible yet robust materials, nanocomposites films[22] combining a polymer host with colloidal inorganic nanoparticles to achieve desired optical, magnetic, or catalytic properties, are of general interest.

1.2.1 Assembling multilayered hybrid films

In nanocomposite fabrication, the main obstacle toward achieving uniform dispersion of nanoparticles within a polymer matrix is colloidal aggregation.[22] To overcome this, methods to prepare hybrid films include direct blending of tailored nanoparticles with polymer,[23] templating approaches involving infiltration of polymer into inorganic mesocrystals,[24] and in-situ reduction of nanoparticles into a polymer matrix.[25] A simpler and more versatile alternative to prepare multilayered hybrid films is layer-by-layer (LbL) assembly.[26]

In LbL assembly, the sequential immersion of a sample in a nanoparticle dispersion and a polymer binder solution enables programmable deposition of composite films onto a substrate. Pioneered by Decher et al to prepare multilayered polyelectrolyte coatings, [27] Lbl assembly has expanded to also incorporate of charged nanoparticles,[28] biomolecules[29] and other materials to create functional thin films.

Film thickness, porosity, refractive index and other factors for LbL assembly can be tuned by varying (a) the film components, (b) the number of layers assembled, (c) deposition method (spray drying,[30] solution immersion,[31,32] spin coating [15,33,34] and/or (d) deposition conditions such as pH and temperature. Linear increase in film thickness with increasing number of immersion cycles is often reported. Interestingly some highly hydrated polymer system such as assembly of PEG based films exhibit exponential growth attributed to highly textured and swollen polymer conformation.[35] For the assembly of electrostatic components, in the first step, the driving force for a polyelectrolyte to adsorb to a charged surface includes the entropic gain for the system as counterions are liberated. While the materials are typically selected based on electrostatic pairing,[27,34,36,37] charge imbalanced assemblies have also been observed. However, this process cannot be carried out to coat neutral or hydrophobic surfaces without the use of surface pre-treatments such as UV ozone[38] or plasma cleaning.[39]

1.2.2 Substrate independent LbL

Inspired by the adhesive chemistry of mussel foot proteins[40,41] that contain catechol-containing peptides as binders,[42] Messersmith and coworkers demonstrated functionalization of substrates by immersion into catechol based solutions[43] and a subsequent report from the same group utilizaed the catechol coating as a base layer, in a strategy termed “substrate-independent LbL”. The reactivity of catechol functional groups within the assembled films has enabled generation of metallic nanoparticles such as silver or titania within a polymer matrix to produce antifouling membranes. While these methods enable the preparation of nanocomposite films, they are limited to or electrostatic pairing of components. Hydrogen bonding based Lbl systems are being explored but these are more suited for degradable films and not robust nanocomposites. Other examples of non-electrostatic interactions include biological recognition,[44] and charge transfer complexes.[27]

The development of a modular catechol based LbL strategy to assemble nanocomposite films from non-ionic building blocks would significantly expand the current scope of LbL film components as well as the range of substrates that could be functionalized using LbL. The multifunctional catechol group would provide two advantages, firstly ability to incorporate a variety of inorganic components as well as anchor to different surfaces. Catechol moieties can under many different reactions including self-crosslinking to enhance film stability,[24] coordination to SiO_2 by hydrogen bonding[45] and the formation of metal transfer complexes to coordinate with metal oxide surfaces such as Fe_2O_3[46] and TiO_2.[47] While these interactions occur under different pH conditions, it should still be feasible to use a single catechol based polymer to anchor coatings onto different substrates and bind different metal oxide nanoparticles to construct robust, multifunctional composite films. Chapter 2 presents an aqueous LbL strategy based on neutral, catechol-functionalized polyacrylamide for controlled deposition of SiO_2 and TiO_2 nanoparticles onto a variety of substrates.

1.3 Colloidal dispersions

The production of polymeric colloids by simple and affordable solution strategies provide access to complex architectures for emerging applications in medicine and photonics. Techniques include emulsion polymerization[48] membrane extrusion,[49] phase separation[50] and precipitation[51]. This section reviews recent examples of block copolymer based particles and microgels.

1.3.1 Structured microparticles

The self-assembly of block copolymers (BCPs) makes them promising building block for functional microparticles. BCPs consist of covalently bonded immiscible segments which gives rise to periodic nanostructured domains.[52] Macroscale phase separation between segments is suppressed by their connectivity and instead microphase separation between the block domains is observed. The equilibrium domain dimensions are determined by a balance between the enthalpy driven segregation of the segments that increases the domain spacing versus the entropic cost of chain stretching (favoring more collapsed chains, thus finer domain spacing).[52]

In the case of bulk assemblies of linear copolymers, equilibrium morphology phase diagrams have been constructed based on the volume fraction of each block, molecular weight (degree of polymerization), and interaction parameter between segments.[52] In order of decreasing symmetry of block volume fractions, AB diblock copolymer configurations range from lamellar formation, complex gyroid phase, cylinders in a continuous phase and finally spherical features.[53] Linear ABC triblock copolymers can access even more configurations such as the formation of spheres or rings of the B phase between cylindrical A features in a continuous C phase. Multicompartment particles have been reported through assembly of linear triblocks copolymers in solution.

Besides BCP composition, the morphology of phase separated assemblies can be also be tuned through control over the polymer architecture such as linear diblock, linear triblock, branched, comb, miktoarm, number of blocks etc. In addition, physical confinement and interfacial engineering can influence phase separation of BCPs within droplets. A seminal report by Shimomura and co-workers on the fabrication of self-assembled BCP nanoparticles in aqueous suspensions in 2005 produced onion-like colloids from lamellar forming poly(styrene)-*b*-poly(isoprene) (PS-PI).[51] Transmission electron microscopy confirmed that the radial lamellar morphology extended throughout the particle. This aqueous assembly of preformed polymers provided a versatile alternative to emulsion polymerization. Prior to 2005, only the core-shell particle morphology had been reported through emulsion based block copolymer synthesis.[48,54]

Building on a similar evaporative selective solvent strategy, Jeon et al. directed the particle inner morphology and shape by tuning the chemistry at the "mobile" interface between the particle and surrounding media.[55] Using a mixture of PS-*b*-PEO surfactant and PBD-*b*-PEO surfactant, they produced ellipsoidal particles with axially stacked lamellae. Onion-like particles with an outer PS layer could also be produced using just PS-*b*-PEO surfactant.[55] In a related strategy, PS-coated gold nanoparticles as surfactants in combination with cetyltriammonium bromide (CTAB) directed the assembly of symmetric poly(styrene-b-2vinylpyridine), (PS-*b*-P2VP) into similar diblock ellipsoids.[56] While it was initially proposed that the anisotropic particle surface tension contributed to the formation of ellipsoids in these systems, a theoretical model developed by Jang et al. attributes the particle elongation to the enthalpic contribution of a reduced PS-*b*-P2VP interface; overriding surface tension and entropic forces that oppose particle deformation and polymer chain stretching.[56] Ellipsoids with similar morphology have also been prepared from PS-*b*-P4VP using a surfactant 3-n-pentadecyphenol (PDP) that hydrogen-bonds to the 4-vinyl pyridine moiety.[57] The use of functional surfactants to orient the BCP domains either in the radial or axial orientation relative to the interface is one powerful example of spatial control over domain arrangement. The inner morphology of BCP based particles can also be controlled via crosslinking strategies and crystallization of metallopolymer such as ferrocene containing derivatives.[58,59]

To illustrate the latter, colloidal assembly of lamella forming poly(ferrocenylsilane)-*b*-poly(2-vinylpyridine) (PFS-*b*-P2VP) has been observed to be dominated by the crystallization of the ferrocene derivative, driving formation of cylindrical structures instead of the expected lamellae assembly.[59] "Living crystallization" of platelet forming PFS block copolymer derivatives can create arbitrary two dimensional structures such as double headed spears.[58] Addressing the crosslinking strategy, selective crosslinking of a domain within BCP particles would provide access to complex architectures and potentially reversible swelling behavior analogous to crosslinked PS-*b*-P2VP diblock copolymer thin films. For instance, PS- *b*-P2VP films crosslinked with dibromobutane and quarternized with dibromoethane can undergo dramatic volume changes as large as 5 fold increase in thickness.[16] While selective crosslinking strategies for block copolymer particles have been reported, these are focused on stabilizing assemblies[60] and do not pursue reversible shape changes. Chapter 3 covers the selective crosslinking of P2VP domains within PS-P2VP ellipsoids to achieve pH responsive shape changing particles.

Hierarchical assemblies of block copolymers based system for photonic applications are also possible through kinetic pathway assemblies and complex emulsions techniques. With reference to kinetically trapped particles, blends of diblock copolymers with distinct molecular geometries (and solvent preference) were kinetically trapped into "multigeometry" nanoparticles such as bilayer discs with spherical edge caps using solvent mixing to achieve local segregation; but not uniform/global equilibrium phase separation within a droplet/particle.[61] Regarding the complex emulsions, Park et al. prepared photonic pigments through complex assemblies of polystyrene/poly(N-isopropylacrylamide-co-acrylic-acid) PS-p(NiPAm-*co*-AAc).[62]

Dense amorphous packings of core–shell PS/p(NiPAm-*co*-AAc)) particles are encapsulated within a large microcapsule (~100 micron) composed of ethoxylated trimethylolpropane triacrylate. These particles exhibit isotropic structural coloration. The microcapsule color can be controlled by either the shell thickness (130–210 nm) or interparticle spacing. However, this elaborate multistep procedure does not produce anisotropic particles preventing subsequent particle alignment. We pursue a simplified method to prepare anisotropic particles, containing internal lamellae morphology, as potential colloidal Bragg reflectors, in Chapter 4.

1.3.2 Microgels

Microgels are internally crosslinked colloidal particles.[63] Notably, the unique combination of the internal network with the ability to independently manipulate microgel particles makes them attractive biomaterial scaffolds, delivery vehicles as well as model systems.

The particle conformation is influenced by the method of preparation and degree of swelling. The degree of swelling is influenced by entropic elasticity and polymer-solvent interactions. Specific to polyelectrolytes, additional factors for microgel conformation and swelling include the presence of salt/ionic strength of solution and the pH.

Microgel networks can be divided into two categories based on the nature of the interaction between crosslinked segments: covalent and physical networks. Regardless of the crosslinking strategy, a common goal would be to be able to systematically tune the network mesh size. Mesh size is a key factor in scaffold mechanics and diffusion of encapsulated cargo. The ideal method would produce microgels with controlled composition and narrow particle size distribution. Specific microgel systems prepared by droplet microfluidics are discussed in the following section.

1.4 Droplet Microfluidics

Microfluidic devices enable control over the flow and break up of fluids within micrometer scale channels.[64] Traditional, undirected droplet generation methods to synthesize microparticles such as emulsion polymerization[48] membrane extrusion,[49] or phase separation[50] often yield batches with large particle size distributions. In contrast, precise manipulation over the flow and mixing of two or more immiscible fluids within microfluidic devices can generate uniform droplets or emulsions.[65] Key considerations for particles produced by droplet microfluidics includes droplet template generation, particle precursor material selection, and internal mixing within the droplet.

Droplet generators can be divided into three main geometries: coflow, T-junction, and focused flow. In a coflow set up, the extrusion of a droplet phase from a capillary can produce passive breakup of the droplet phase within a continuous phase (fluid or air).[66] The T-junction geometry, consists of a perpendicular stream of the continuous phase shears off the droplet phase.[67] The third geometry, focused flow geometry, was first report by Anna et al. in 2003, in which water droplets were generated in silicone oil. To do this, a water channel was crossed two outer oil streams across a narrow opening which breaks up the water phase into droplets.[68] This geometry offers more stable flow regimes than the T-junction which can be more susceptible to chaotic flows that result in a loss of control over droplet size.[69] However, droplet formation within the flow focused geometry is highly influenced by the surface wetting properties of the channels. For instance, stable water droplet formation requires hydrophobic microchannels.[70] In the case of a focused flow device with hydrophilic channels, a set up containing a middle water stream focused by two outer oil streams, would still generate oil droplets in a continuous water phase downstream of the orifice; contrary to the expected production of water droplets.[71] In addition to channel wettability, other considerations include channel dimensions and relative flow ratios of the continuous phase to droplet phase in order to tune the droplet size.[72] For uniform droplet composition, internal mixing of the components is necessary. While controlled droplet formation necessitates laminar flow and low shear forces by the continuous phase, internal mixing of the droplet phase requires chaotic advection. To this end, several geometric designs have been employed including ridges[73] and curved channels.[74]

Regarding particle synthesis, methods of solidification (for the monomer or polymer contained within the droplet) include solvent evaporation and crosslinking methods. The production of drug loaded poly(lactide-*co*-glycolide) (PLGA) microspheres by flow focusing microfluidic devices has been reported since 2009, and incorporates polyvinyl alcohol as surfactants into the continuous phase to prevent particle coalescence.[75–77] While this system demonstrates exquisite size control, the use of organic solvent significantly limits the compatibility of this system. Microspheres from natural polymers such as alginate and chitosan provide a biocompatible alternative due to water solubility and potential for mild physical gelation by multivalent ions[10,19] or by homopolymers.[20] However, the disadvantages of natural polymers such as compositional variation among polymers from different harvested batches[21] motivates the assembly of microgels from water soluble synthetic polymers.

Combining droplet microfluidics with initiator-free covalent crosslinking, Rossow et al. reported covalent microgels prepared from hyperbranched polyglycerol acrylate and dithiol polyethylene glycol macro-crosslinkers for cell encapsulation.[78] This use of synthetic microgel precursors produces scaffolds with well-defined covalent internal networks, but non-covalent associations in microgels may offer the advantage of reversible interactions such as dynamic assembly[79,80] or anion exchange.[81] In the current literature, a microfluidic preparation method for non-covalent microgels from synthetic block copolymers has yet to be reported. Addressing this gap, Chapter 5 describes the design and use of a microfluidic flow focusing device to assemble well-defined ABA triblock copolyelectrolytes within water droplets into well-defined non-covalently crosslinked microgels containing functional payloads.

1.5 References

1. Lohse, S. E.; Murphy, C. J. *J. Am. Chem. Soc.* **2012**, *134*, 15607–15620.
2. Stucky, G. D.; Ostomel, T. A.; Shi, Q.; Stoimenov, P. K.; Holden, P. A. Google Patents January 12, 2009.
3. Silvestre, C.; Duraccio, D.; Cimmino, S. *Prog. Polym. Sci.* **2011**, *36*, 1766–1782.
4. De Volder, M. F. L.; Tawfick, S. H.; Baughman, R. H.; Hart, A. J. *Science.* **2013**, *339*, 535–539.
5. Zhang, H.; Jin, M.; Xia, Y. *Angew. Chemie Int. Ed.* **2012**, *51*, 7656–7673.
6. Wegst, U. G. K.; Bai, H.; Saiz, E.; Tomsia, A. P.; Ritchie, R. O. *Nat. Mater.* **2014**, No. October, 1–14.
7. Grinthal, A.; Aizenberg, J. *Chem. Soc. Rev.* **2013**, *42*, 7072–7085.
8. Stefik, M.; Guldin, S.; Vignolini, S.; Wiesner, U.; Steiner, U. *Chem. Soc. Rev.* **2015**. 44, 5076-5091.
9. Schacher, F. H.; Rupar, P. A.; Manners, I. *Angew. Chemie - Int. Ed.* **2012**, *51*, 7898–7921.
10. Alfrey, T.; Gurnee, E. F.; Schrenk, W. J. *Polym. Eng. Sci.* **1969**, *9*.
11. Sheppard, C. J. R. *Pure Appl. Opt. J. Eur. Opt. Soc. Part A* **1995**, *4*, 665.
12. Bonifacio, L. D.; Lotsch, B. V.; Puzzo, D. P.; Scotognella, F.; Ozin, G. A. *Adv. Mater.* **2009**, *21*, 1641–1646.
13. Bonifacio, L. D.; Puzzo, D. P.; Breslav, S.; Willey, B. M.; McGeer, A.; Ozin, G. *Adv. Mater.* **2010**, *22*, 1351–1354.
14. Yu, Z.; Wang, C.-F.; Ling, L.; Chen, L.; Chen, S. *Angew. Chem. Int. Ed. Engl.* **2012**, *51*, 2375–2378.
15. Wu, Z.; Lee, D.; Rubner, M. F.; Cohen, R. E. *Small* **2007**, *3*, 1445–1451.
16. Kang, Y.; Walish, J. J.; Gorishnyy, T.; Thomas, E. L. *Nat. Mater.* **2007**, *6*, 957–960.

17. Kinoshita, S.; Yoshioka, S. *ChemPhysChem* **2005**, *6*, 1443–1459.

18. Tao, A. R.; DeMartini, D. G.; Izumi, M.; Sweeney, A. M.; Holt, A. L.; Morse, D. E. *Biomaterials* **2010**, *31*, 793–801.

19. Ball, P. *Sci. Am.* **2012**, *306*, 74–79.

20. Sundgren, J. E.; Hentzell, H. T. G. *J. Vac. Sci. Technol. A* **1986**, *4*.

21. Feili, D.; Schuettler, M.; Doerge, T.; Kammer, S.; Hoffmann, K. P.; Stieglitz, T. *J. Micromechanics Microengineering* **2006**, *16*, 1555–1561.

22. Balazs, A. C.; Emrick, T.; Russell, T. P. *Science* **2006**, *314*, 1107–1110.

23. Corbierre, M. K.; Cameron, N. S.; Sutton, M.; Mochrie, S. G. J.; Lurio, L. B.; Rühm, A.; Lennox, R. B. *J. Am. Chem. Soc.* **2001**, *123*, 10411–10412.

24. Capadona, J. R.; Van Den Berg, O.; Capadona, L. a; Schroeter, M.; Rowan, S. J.; Tyler, D. J.; Weder, C.; Berg, O. V. A. N. D. E. N. *Nat. Nanotechnol.* **2007**, *2*, 765–769.

25. Selvan, T.; Spatz, J. P.; Klok, H.-A.; Möller, M. *Adv. Mater.* **1998**, *10*, 132–134.

26. Decher, G. **2012**, 1–21.

27. Decher, G. *Science* **1997**, *277*, 1232–1237.

28. Schmitt, J.; Decher, G.; Dressick, W. J.; Brandow, S. L.; Geer, R. E.; Shashidhar, R.; Calvert, J. M. *Adv. Mater.* **1997**, *9*, 61–65.

29. Min, Y.; Hammond, P. T. *Chem. Mater.* **2011**, *23*, 5349–5357.

30. Nogueira, G. M.; Banerjee, D.; Cohen, R. E.; Rubner, M. F. *Langmuir* **2011**, *27*, 7860–7867.

31. Liaqat, F.; Tahir, M. N.; Schechtel, E.; Kappl, M.; Auernhammer, G. K.; Char, K.; Zentel, R.; Butt, H.-J.; Tremel, W. *Macromol. Rapid Commun.* **2015**, n/a – n/a.

32. Kharlampieva, E.; Kozlovskaya, V.; Gunawidjaja, R.; Shevchenko, V. V.; Vaia, R.; Naik, R. R.; Kaplan, D. L.; Tsukruk, V. V. *Adv. Funct. Mater.* **2010**, *20*, 840–846.

33. Calvo, M. E.; Sánchez Sobrado, O.; Lozano, G.; Míguez, H. *J. Mater. Chem.* **2009**, *19*, 3144.

34. Pavlichenko, I.; Exner, A. T.; Guehl, M.; Lugli, P.; Scarpa, G.; Lotsch, B. V. **2012**, 298–305.

35. Quinn, J. F.; Johnston, A. P. R.; Such, G. K.; Zelikin, A. N.; Caruso, F. *Chem. Soc. Rev.* **2007**, *36*, 707–718.

36. Sánchez-Sobrado, O.; Calvo, M. E.; Míguez, H. *J. Mater. Chem.* **2010**, *20*, 8240.

37. Choi, S. Y.; Mamak, M.; von Freymann, G.; Chopra, N.; Ozin, G. A. *Nano Lett.* **2006**, *6*, 2456–2461.

38. Vig, J. R. *J. Vac. Sci. Technol. A* **1985**, *3*, 1027.

39. Hsieh, M. C.; Farris, R. J.; McCarthy, T. J. *Macromolecules* **1997**, *30*, 8453–8458.

40. Waite, J. H.; Andersen, N. H. No. July 2014, 37–41.

41. Waite, J. H.; Tanzer, M. L. *Sci.* **1981**, *212* , 1038–1040.

42. Holten-Andersen, N.; Harrington, M. J.; Birkedal, H.; Lee, B. P.; Messersmith, P. B.; Lee, K. Y. C.; Waite, J. H. *Proc. Natl. Acad. Sci. U. S. A.* **2011**, *108*, 2651–2655.

43. Lee, H.; Dellatore, S. M.; Miller, W. M.; Messersmith, P. B. *Science* **2007**, *318*, 426–430.

44. Anzai, J.; Nishimura, M. *J. Chem. Soc. Perkin Trans. 2* **1997**, No. 10, 1887–1889.

45. Malisova, B.; Tosatti, S.; Textor, M.; Gademann, K.; Zürcher, S. *Langmuir* **2010**, *26*, 4018–4026.
46. Yuen, A. K. L.; Hutton, G. a.; Masters, A. F.; Maschmeyer, T. *Dalt. Trans.* **2012**, *41*, 2545.
47. Lana-Villarreal, T.; Rodes, A.; Pérez, J. M.; Gómez, R. *J. Am. Chem. Soc.* **2005**, *127*, 12601–12611.
48. Bradley, M.; Grieser, F. *J. Colloid Interface Sci.* **2002**, *251*, 78–84.
49. Tangirala, R.; Revanur, R.; Russell, T. P.; Emrick, T. *Langmuir* **2007**, *23*, 965–969.
50. Loxley, A.; Vincent, B. *Colloid Polym. Sci.* **1997**, *275*, 1108–1114.
51. Yabu, H.; Higuchi, T.; Shimomura, M. *Adv. Mater.* **2005**, *17*, 2062–2065.
52. Bates, F. S. *Annu. Rev. Phys. Chem.* **1990**, *41*, 525–557.
53. Matsen, M. W.; Bates, F. S.; M.W. Matsen, F. S. B. *Macromolecules* **1996**, *29*, 7641–7644.
54. Stutman, D. R.; Klein, A.; El-Aasser, M. S.; Vanderhoff, J. W. *Ind. Eng. Chem. Prod. Res. Dev.* **1985**, *24*, 404–412.
55. Jeon, S.-J.; Yi, G.-R.; Yang, S.-M. *Adv. Mater.* **2008**, *20*, 4103–4108.
56. Jang, S. G.; Audus, D. J.; Klinger, D.; Krogstad, D. V; Kim, B. J.; Cameron, A.; Kim, S.-W.; Delaney, K. T.; Hur, S.-M.; Killops, K. L.; Fredrickson, G. H.; Kramer, E. J.; Hawker, C. J. *J. Am. Chem. Soc.* **2013**, *135*, 6649–6657.
57. Deng, R.; Liang, F.; Li, W.; Liu, S.; Liang, R.; Cai, M. **2013**, 1–5.
58. Hudson, Z. M.; Boott, C. E.; Robinson, M. E.; Rupar, P. A.; Winnik, M. A.; Manners, I. *Nat Chem* **2014**, *6*, 893–898.
59. Schmidt, B. V. K. J.; Elbert, J.; Scheid, D.; Hawker, C. J.; Klinger, D.; Gallei, M. *ACS Macro Lett.* **2015**, *4*, 731–735.
60. Li, Y.; Hindi, K.; Watts, K. M.; Taylor, J. B.; Zhang, K.; Li, Z.; Hunstad, D. A.; Cannon, C. L.; Youngs, W. J.; Wooley, K. L. *Chem. Commun.* **2010**, *46*, 121–123.
61. Zhu, J.; Zhang, S.; Zhang, K.; Wang, X.; Mays, J. W.; Wooley, K. L.; Pochan, D. J. *Nat. Commun.* **2013**, *4*, 2297.
62. Park, J.-G.; Kim, S.-H.; Magkiriadou, S.; Choi, T. M.; Kim, Y.-S.; Manoharan, V. N. *Angew. Chem. Int. Ed. Engl.* **2014**, *53*, 2899–2903.
63. Klinger, D.; Landfester, K. *Polym. (United Kingdom)* **2012**, *53*, 5209–5231.
64. Whitesides, G. M. *Nature* **2006**, *442*, 368–373.
65. Seemann, R.; Brinkmann, M.; Pfohl, T.; Herminghaus, S. *Rep. Prog. Phys.* **2012**, *75*, 016601.
66. Anna, S. L.; Mayer, H. C. *Phys. Fluids* **2006**, *18*, 121512.
67. Thorsen, T.; Roberts, R. W.; Arnold, F. H.; Quake, S. R. *Phys. Rev. Lett.* **2001**, *86*, 4163–4166.
68. Anna, S. L.; Bontoux, N.; Stone, H. A. *Appl. Phys. Lett.* **2003**, *82*, 364–366.
69. Christopher, G. F.; Anna, S. L. *J. Phys. D. Appl. Phys.* **2007**, *40*, R319–R336.
70. Seo, M.; Paquet, C.; Nie, Z.; Xu, S.; Kumacheva, E. *Soft Matter* **2007**, *3*, 986.
71. Abate, A. R.; Seiffert, S.; Utada, A. S.; Shum, A.; Shah, R.; Thiele, J.; Duncanson, W. J.; Lee, M. H.; Akartuna, I.; Lee, D.; Rotem, A.; Weitz, D. A. 1–21.
72. Tice, J. D.; Song, H.; Lyon, A. D.; Ismagilov, R. F. *Langmuir* **2003**, *19*, 9127–9133.

73. Sugiura, S.; Nakajima, M.; Tong, J.; Nabetani, H.; Seki, M. *J. Colloid Interface Sci.* **2000**, *227*, 95–103.

74. Song, H.; Tice, J. D.; Ismagilov, R. F. *Angew. Chemie, Int. Ed. English* **2003**, *42*, 768–772.

75. Xu, Q.; Hashimoto, M.; Dang, T. T.; Hoare, T.; Kohane, D. S.; Whitesides, G. M.; Langer, R.; Anderson, D. G. *Small* **2009**, *5*, 1575–1581.

76. Häfeli, U. O.; Saatchi, K.; Elischer, P.; Misri, R.; Bokharaei, M.; Labiris, N. R.; Stoeber, B. *Biomacromolecules* **2010**, *11*, 561–567.

77. Schneider, T.; Chapman, G. H.; Häfeli, U. O. *Colloids Surf. B. Biointerfaces* **2011**, *87*, 361–368.

78. Rossow, T.; Heyman, J. A.; Ehrlicher, A. J.; Langhoff, A.; Weitz, D. A.; Haag, R.; Seiffert, S. *J. Am. Chem. Soc.* **2012**, *134*, 4983–4989.

79. Go, D.; Kodger, T. E.; Sprakel, J.; Kuehne, A. *Soft Matter* **2014**, *10*, 8060–8065.

80. Fitzgerald, P. A.; Amalvy, J. I.; Armes, S. P.; Wanless, E. J. *Langmuir* **2008**, *24*, 10228–10234.

81. Rahman, M. T.; Barikbin, Z.; Badruddoza, A. Z. M.; Doyle, P. S.; Khan, S. a. *Langmuir* **2013**, *29*, 9535–9543.

2 Catechol-based layer-by-layer assembly of composite coatings: a versatile platform to hierarchical nano-materials[*]

2.1 Introduction

In numerous applications, performance is highly dependent on the interface between the material and its surrounding environment. Many devices, ranging from–biocompatible neural implants[1], antireflective optical coatings[2–5] to antifouling sensors,[6–10] rely on thin-film coatings[4] to achieve the desired surface chemistry or functionality. While chemically tunable and flexible surfaces are easily accessible via polymeric films,[11] more robust coatings are usually realized using inorganic components. By combining the advantages of both systems, composite coatings realize flexibility and robustness in one multifunctional material.[12,13] However, the formation of nanocomposites creates new challenges regarding deposition methods suitable for highly disparate building blocks, e.g., ensuring uniform dispersion of inorganic particles in a polymeric matrix.[14–16] Existing nanocomposite coating methods, such as spin coating[6–8] and spray deposition,[17,18] provide precise control over film architecture, but the scope of such methods is limited by the compatibility of the components with the chosen deposition method, the substrate and/or the substrate geometry.

---

[*] Reproduced with permission: Wang, C. X.; Braendle, A.; Menyo, M. S.; Pester, C. W.; Perl, E. E.; Arias, I.; Hawker, C. J.; Klinger, D. *Soft Matter*. **2015**, 11, 6173-79. Copyright 2015, Royal Society of Chemistry.

To overcome these limitations and coat multicomponent films on complex substrate geometries, a powerful strategy known as layer-by-layer (LbL) assembly[19] is commonly used. This technique involves the sequential immersion of a sample in a nanoparticle dispersion and a binder solution for film growth. However, since this process is typically driven by electrostatics,[6–8,20] it requires the use of charged hydrophilic substrates and cannot be used with neutral or hydrophobic surfaces without the use of surface treatments such as UV ozone irradiation[21] or plasma cleaning.[22] For this reason, there is an active effort to expand the LbL toolbox to additional assembly methods. An ideal technique should encompass the following criteria: a) use of aqueous media for an affordable, environmentally friendly process; b) formation of stable films; c) construction of films with tunable composition; and d) substrate independent assembly.

Nature presents us with a number of systems in which all these criteria align. One striking example is the marine mussel, which can strongly anchor to many surfaces in aqueous surroundings by using catechol-containing proteins as binders.[23] Inspired by this unique underwater adhesive strategy, we propose using biomimetic synthetic catechol derivatives[24,25] to develop a new aqueous dip coating platform independent of electrostatics.
An emerging area of focus has been the recent development of film assembly strategies based on catechol groups as binders. In these systems, polymer coatings are accessible via hydrogen bond-driven, sequential assembly between poly(vinylpyrrolidone) and catechol containing polymers.[26] While these materials can be prepared from aqueous solutions they do not extend to composite films. In contrast, the formation of composite materials has been reported via infiltration of catechol-based polymers into inorganic nanoparticle mesocrystals but relies on the utilization of organic solvents.[27] The work details the preparation of robust

nanocomposite coatings on arbitrary substrates by dip coating from aqueous solutions and demonstrates a new modular approach towards the facile construction of hierarchical nanostructured composites from easily accessible components. (Figure 2.1).

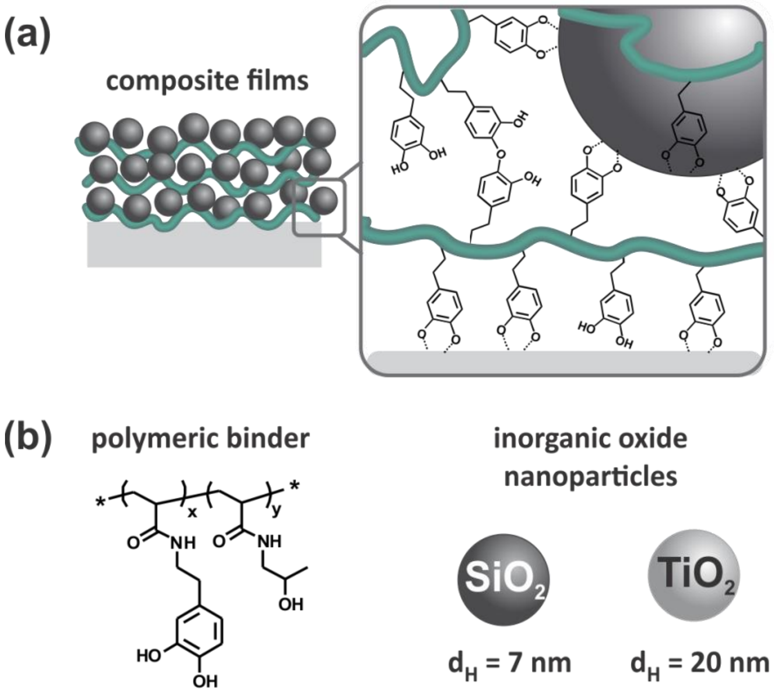

Figure 2.1. Layer-by-layer assembly of nanocomposite films from polymeric catechol binders and inorganic oxide nanoparticles (NPs) (a) Schematic representation of composite films based on different catechol interactions: anchoring to the substrate and oxide NPs as well as intermolecular covalent crosslinking. **(b)** Coating components used in this study: polyacrylamide-based catechol binder and oxide NPs.

2.2 Results and Discussion

2.2.1 Controlled deposition of silica-composite and titania-composite films on model Si substrates

The polymeric binder was designed to exhibit two functionalities: hydroxylpropylacrylamide units allow for water solubility, and catechol moieties not only serve to anchor the nanocomposite onto the substrate but also to incorporate silicon dioxide (SiO_2) and titanium dioxide (TiO_2) nanoparticles into coatings (Figure 2.1a). Moreover, it is assumed that free catechol groups that are not coordinated to the silica or titania surface can undergo a variety of self-crosslinking reactions to enhance film stability.[24] Binder synthesis via post-polymerization functionalization[28,29] enables optimization of the catechol incorporation[30] with a random copolymer containing 15 mol % catechol units achieve excellent binding in addition to water solubility. Using this copolymer binder, a layer-by-layer process was developed to form composite films with the assembly of SiO_2–polymer and TiO_2–polymer films on a model substrate (thermally annealed silicon (Si) wafers with a 100 nm SiO_2 surface) investigated. The sequential immersion of the substrate into the polymer and nanoparticle solution is defined as a deposition “cycle” for simplicity. In this process, a Si wafer substrate is first soaked in an aqueous solution of the catechol-polymer binder and rinsed to remove unbound polymer (Figure 2.2).

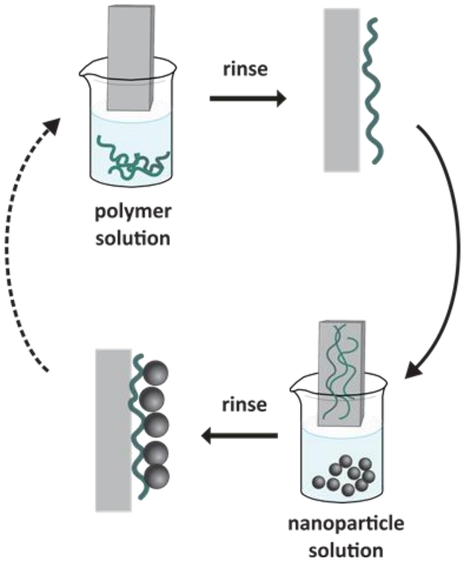

Figure 2.2 Schematic representation of one dip coating cycle. Sequential adsorption of polymer and nanoparticles onto substrate is accompanied by respective rinsing steps.

Free catechol units from this base layer can then bind oxide nanoparticles through simple dipping in a dispersion of the nanoparticles in the second step. Following another rinsing procedure, the cycle can be repeated until the desired thickness is achieved. The increase of film thickness with the number of dipping cycles was investigated visually and by reflectometry[4] with the results shown in Figure 1.3. In the case of the SiO_2 nanoparticle composite films, the pH of the deposition and rinsing solutions was adjusted to pH 1–2 in order to facilitate hydrogen bonding between the catechol and the silica nanoparticles.[31] With progression of dipping cycles, highly uniform SiO_2-polymer films display a red shift

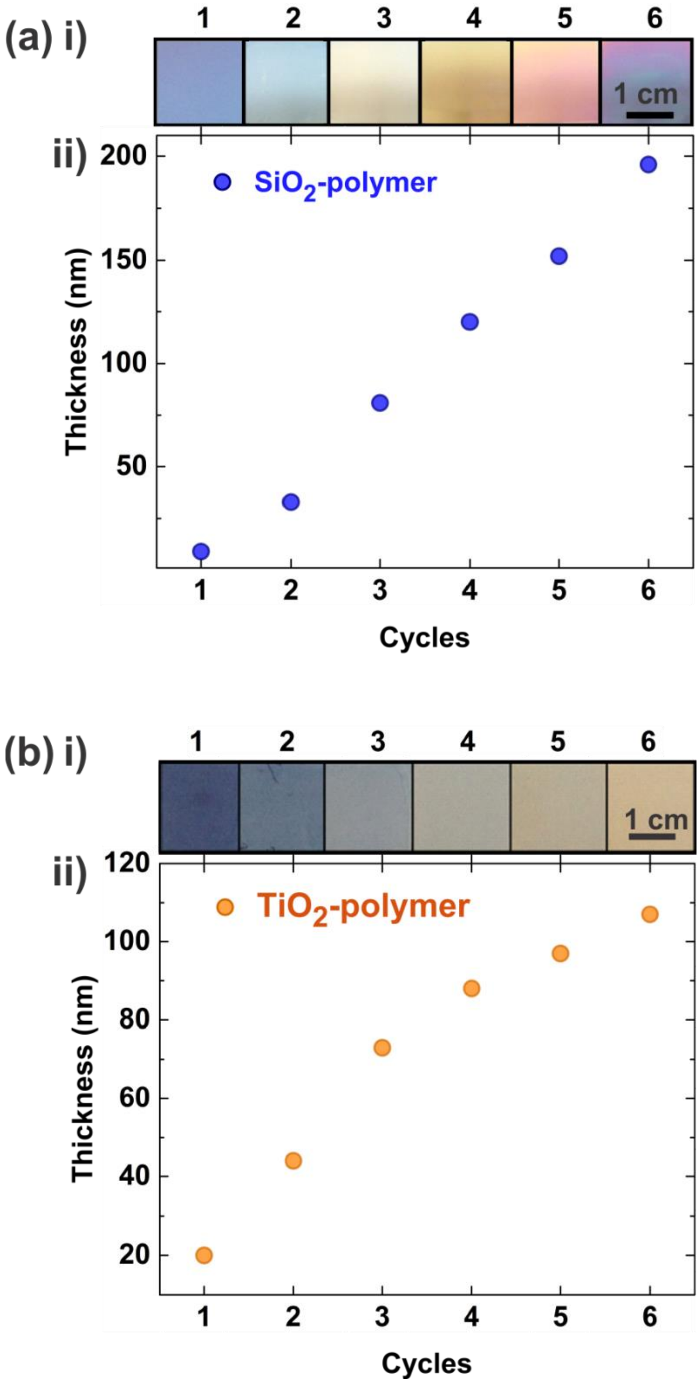

Figure 2.3. Progression of film thickness with number of dipping cycles. (a) SiO_2-polymer composites; **(b)** TiO_2-polymer composites. **i)** Optical images of coated Si wafers after the corresponding number of dipping cycles. **ii)** Thickness estimated by reflectometry in dependence of number of dipping cycles.

in reflected color due to thin film interference.[4] This corresponds to a linear increase in film thickness with a composite growth of around 30–50 nm per cycle (Figure 2.3a). This facile method could also be extended to the fabrication of TiO_2-polymer composites requiring only one modification: the pH of the solutions is increased to pH 4.5 in order to promote formation of catechol-TiO_2 charge transfer complexes.[31,32] From this procedure, uniform composite films were formed with a consistent deposition per cycle of around 15–20 nm (Figure 2.3). For both systems, it becomes obvious that the composite deposition per cycle exceeds the size of each individual building blocks. Taking into account the polydispersity of the nanoparticles' sizes and the dynamic nature of the coordinative bonds, it is apparent that the composite build-up exceeds the addition of a single nanoparticle monolayer which is consistent with multi-valent interactions between multiple nanoparticles per polymer chain.

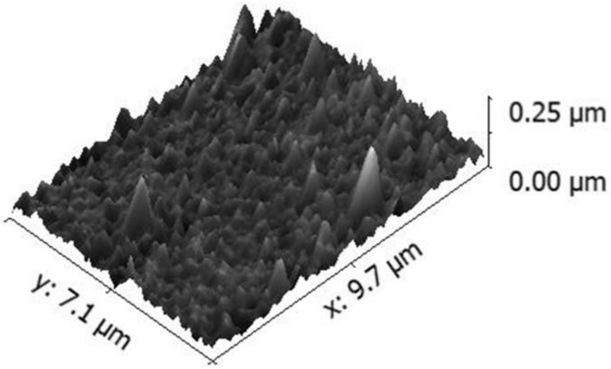

Figure 2.4. **AFM of composite film bilayer surface**. Minor surface roughness due to particle aggregation, but no macroscopic clusters present. The coating of a top layer of TiO_2 -composite film (4 cycles, 70 nm thickness) deposited onto a SiO_2 -composite film (4 cycles, 110 nm thickness) on top of a wafer substrate (Si with 100 nm SiO_2 surface layer).

Notably, as shown by AFM investigations, this build up mechanism is not accompanied by the formation of any macroscopic nanoparticle clusters (Fig 1.4). Homogeneous distribution of the nanoparticles throughout the polymeric matrix is further evidenced by SEM investigations on the composites' cross-section and surface (see Figure 1.5). To demonstrate that this coating platform was not substrate specific, SiO_2 -composite films were also deposited on a planar hydrophobic surface. Polystyrene was spin-coated onto a

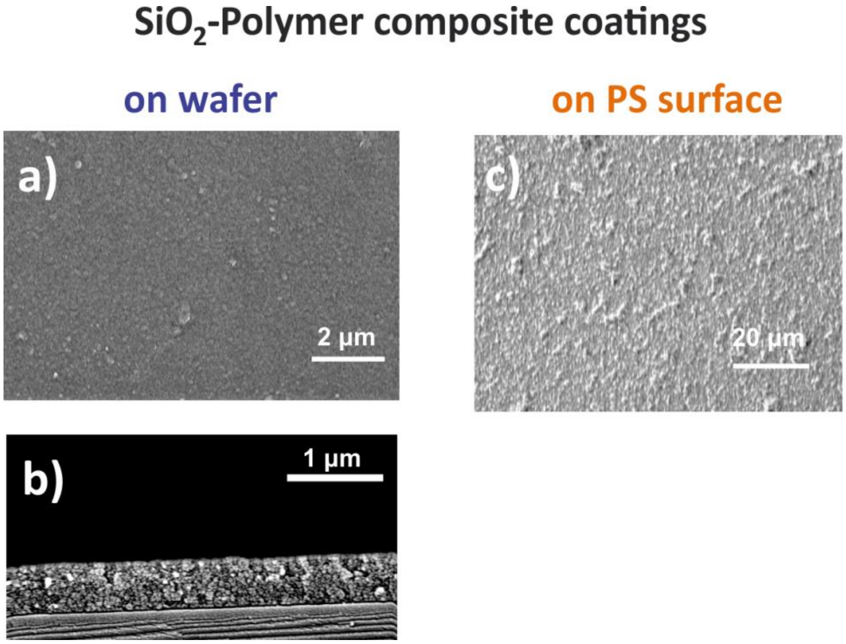

Figure 2.5. SEM of SiO_2-composite films on different substrates. SiO_2 -composite films were deposited onto a wafer and SEM investigations were performed on a) the surface of SiO_2 -composite film (4 cycles, 110 nm thickness) and b) the cross section of a SiO_2 -composite film (20 cycles, 500 nm thickness) which shows a close-packed film with nanoparticles distributed homogeneously throughout. c) SiO_2 -composite film on a planar hydrophobic surface, (spin-coated polystyrene).The coating appears continuous with some small aggregates. All Si wafer substrates used contained a thermally annealed 100 nm SiO_2 surface layer.

wafer (80 nm), and this surface was coated with the SiO_2 -composite film (16 cycles, 480 nm thickness). The coating appears continuous with some small aggregates (Figure 1.5c). Therefore, this controlled deposition method allows for the preparation of films with excellent homogeneity from the micro- to the centimetre length scale.

2.2.2 Coating inner tube surfaces with titania-composite film

Having demonstrated the controlled deposition of silica- and titania-based composites on flat model surfaces, it is of high interest to determine whether this coating method could impart functionalities to substrates that are not readily accessible by other coating techniques. In this context, the formation of nanoparticle-polymer composite coatings on the inner surface of tubes or channels represents an interesting approach to impart omniphobicity[33] or antifouling properties.[34]

Unfortunately, coating of such hollow structures is often hindered by the accessibility of the surface - an aqueous dip coating platform would provide a benign alternative to existing methods such as harsh sol-gel chemistry.[35] However, traditional LbL methods still require surface pre-treatments to generate charges, thereby limiting their applicability. Hence, circumventing these limitations by coating internal surfaces and other challenging substrates via the catechol-based dip coating method would represent a dramatic improvement over existing methods.

To test the potential of the catechol LbL technique, the same precursor solutions and deposition process as with the Si wafer was used to immobilize a TiO_2-polymer composite film (6 cycles) on the inside of a commercially available untreated polyvinyl chloride (PVC) tube. To investigate the deposition, a cut segment of the tube was examined by SEM (Figure 2.6).

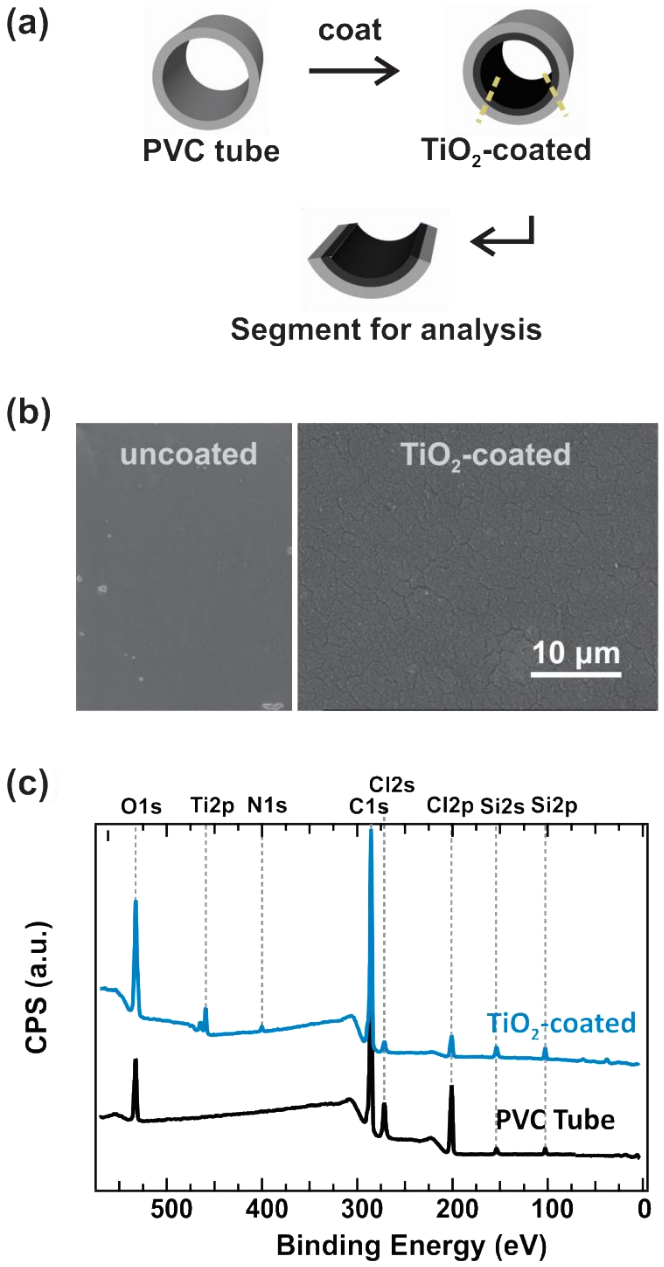

Figure 2.6. Coating of the inner surface of a PVC tube with TiO_2-polymer composite. **(a)** Scheme of tube coating process. **(b)** SEM of coated inner surface of tube in comparison to a non-coated area. **(c)** X-ray photoelectron spectroscopy (XPS) shows that TiO_2 nanoparticles can be immobilized onto the inner surface of a polyvinyl chloride tube.

In contrast to an untreated part of the tube, the composite material is clearly visible in the areas subjected to the dipping procedure. Further investigations per X-ray photoelectron spectroscopy (XPS) indicate surface immobilization of TiO_2 nanoparticles, as evidenced by the titanium 2p peaks. In combination with the carbon 1s, nitrogen 1s, and oxygen 1s peaks of the polymeric binder, these signals reflect the composition of the TiO_2-polyacrylamide coating. Chlorine and silicon peaks can be assigned to the PVC substrate and lubricants in the tubing, respectively . This composite film deposited onto the PVC tube appears slightly different to the composite film deposited onto a planar wafer (Figure 2.7). We attribute these differences to the deformation of the coated tube during sample mounting.

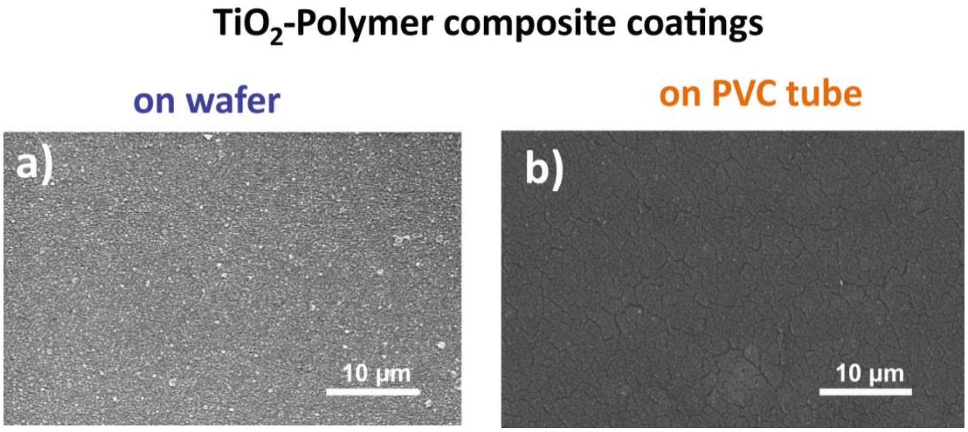

Figure 2.7. **SEM of TiO_2-composite films on different substrates.** Comparison of the surface of TiO_2 -composite film (5 cycles) deposited onto a) a wafer substrate versus b) a PVC tube (6 cycles) by scanning electron microscopy. While the films on the planar wafer appear smooth and continuous, cracks in the tube coating may be due to sample deformation while dissecting and mounting the sample after the coating process.

2.2.3 Degradation studies of composite films subject to different pH conditions and ionic strength

The potential use of such thin film coatings in advanced applications crucially depends on the resistance of the assembled composites against undesired environmental degradation, including a decrease in film thickness or partial/complete detachment off the substrate. The strength of catechol binding and potential secondary covalent crosslinking reactions suggest that these catechol-based assemblies may withstand a broader range of acidic and basic conditions than comparably weak polyelectrolyte LbL assemblies.[36]

To test the resistance of the composite films, coatings on Si wafers were immersed into buffered aqueous solutions of varied pH for 5 days. Of main interest are conditions that could weaken the catechol-oxide interaction. Thus, the influence of neutral and basic buffers is shown in Figure 2.8 since the coordinative bond strength is reduced considerably and catechol moieties are prone to oxidation at these pH values. At predetermined time intervals, the coated films were dried and their thickness determined using reflectometry. No significant change in thickness were observed for the films immersed in pH 7.4 buffered aqueous solutions of high ionic strength (1 M NaCl) after five days. In the case of pH 10 immersion, TiO_2 composite films remain stable while a minor reduction (~20%) in film thickness was observed for SiO_2-composite films. SiO_2-composite films are resistant to solutions buffered to pH 2, and in contrast, TiO_2 – composite films undergo marginal reduction in film thickness which may be due to disruption of the metal charge transfer complex at the surface layers under acidic conditions. Additionally, the stability of the films against organic solvents was also investigated by immersing the samples in tetrahydrofuran (THF), a good solvent for the polymeric binder. Samples were also immersed in toluene, a non-polar organic solvent (Figure 2.9). Both composite films were stable in THF as tested for five days. TiO_2-composite films remain stable with a constant thickness for up to 5 days immersed in toluene, while SiO_2-composite films under the same conditions swell slightly, less than 10% overall.

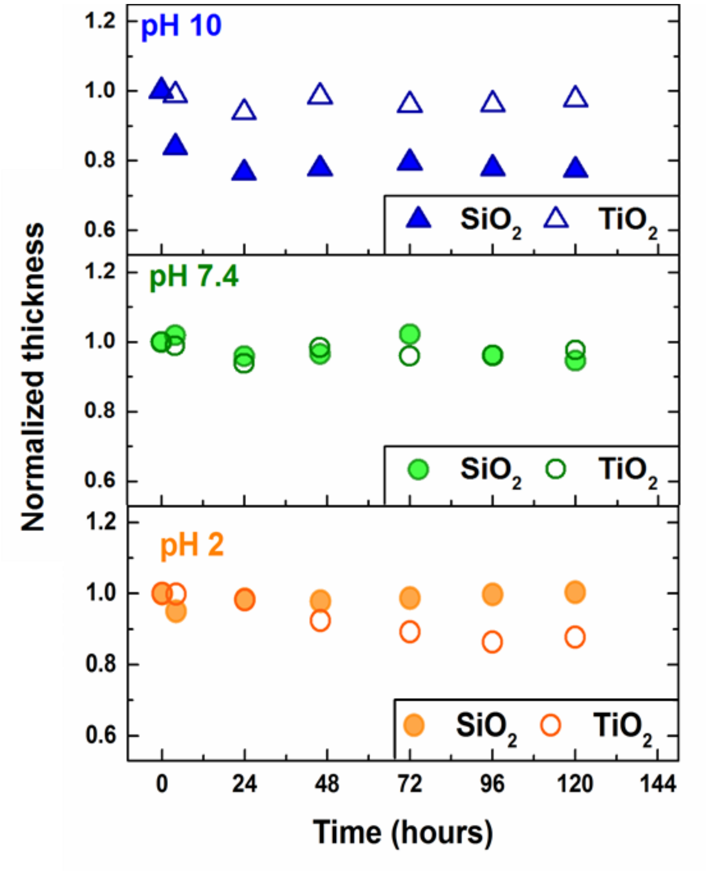

Figure 2.8. Degradation study of films under different pH conditions (high ionic strength). SiO_2 and TiO_2 composite films remain stable under neutral conditions of high ionic strength. SiO_2 composite films are more resistant to acidic conditions while TiO_2 composite films are more tolerant of basic conditions.

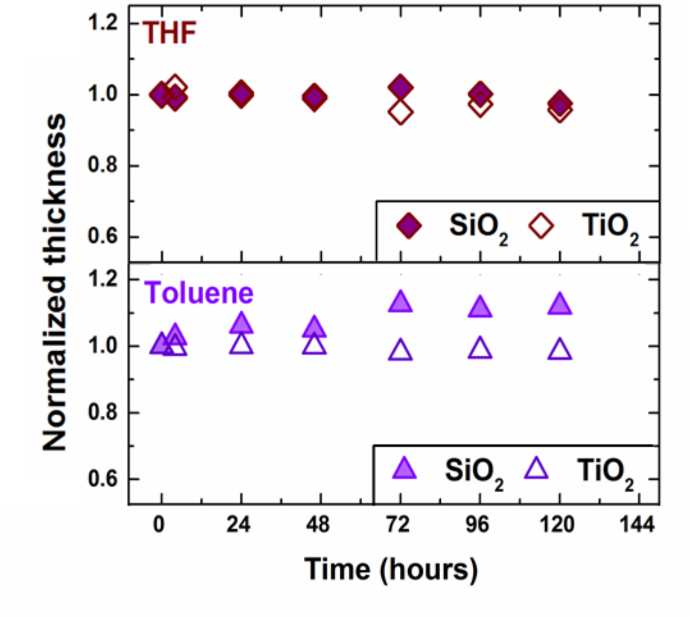

Figure 2.9. Solvent resistance of SiO_2 and TiO_2 composite films. Both are are able to withstand THF, a polar organic solvent, for over 5 days. TiO_2-composite films remain stable with a constant thickness for up to 5 days immersed in toluene, while SiO_2-composite films under the same conditions swell slightly.

While the overall outstanding stability is assumed to result from a combination of the strong catechol oxide-NP interactions and potential inter-catechol crosslinks under oxidizing conditions, the observed decay in film thickness to a constant level in the silica composites might be assigned to disrupted hydrogen bonds on the film surface at elevated pH. Overall, the coatings showed exceptional stability with no visible change in film morphology against all the conditions investigated.

2.2.4 Preparation of Bragg stack coatings on glass substrates from catechol-based composite multilayers

In combination with the modularity and high level of control, the catechol-based dip coating process is promising for the preparation of more complex coatings such as hierarchically structured films. In such materials, a specific function is achieved by controlling the spatial confinement of different building blocks. In the one dimensional case of multilayer films, controlling the refractive index and thickness of individual layers enables the preparation of periodic structures such as Bragg stacks. Bragg stacks are photonic materials that consist of alternating layers of low and high refractive index materials. This structure results in the selective reflection of light over a narrow range of wavelengths therefore rendering these materials brightly colored.[4]

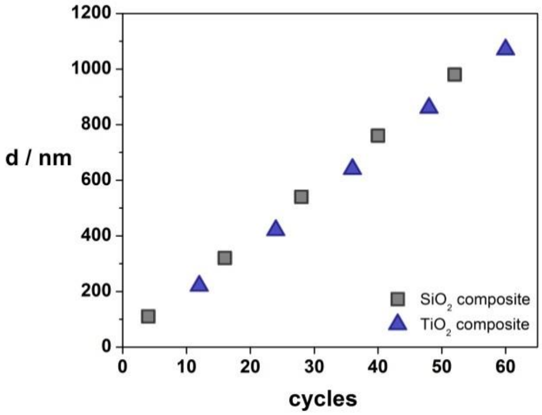

Figure 2.10. Progression of layer thickness with dipping cycles for the build-up of multi-layered Bragg stacks. Shown are the thicknesses of the composite multilayers where the legend denotes the respective top layer.

To demonstrate the applicability of the catechol LbL platform for the preparation of such photonic materials, Bragg stack coatings were prepared on a transparent glass substrate (Figure 2.11). Alternating layers of SiO_2 and TiO_2 composites serve as low ($n_{SiO2\text{-}composite}$=1.47) and high refractive index ($n_{titania\text{-}comp}$=1.63) domains, respectively. The reflectance of ten alternating layers of SiO_2 and TiO_2 composites was measured on a

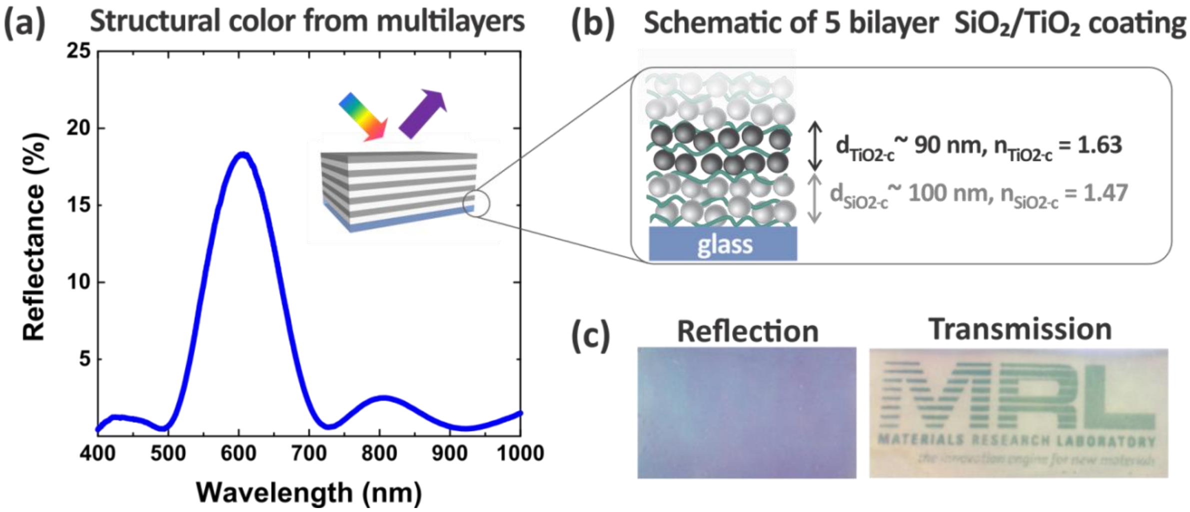

Figure 2.11. Bragg stack coatings on glass substrates: Structural color from multilayer composites. Ten alternating layers of low refractive index SiO2 composite and high refractive index TiO2 composite (5 bilayers) were deposited onto a glass substrate. (a) Experimental reflectance spectrum exhibits a Bragg peak at 600 nm. (b) Schematic representation of SiO2-composite films and TiO2-composite films, indicating the thickness d and refractive index n of individual layers. (c) Structural color is observed in reflection. In transmission, films are transparent.

spectroscopic reflectometer (Figure 2.11). The experimental reflectance curve is in good agreement with a simulated Bragg stack reflectance spectra calculated for these materials (Figure 2.12)**.** While the reduced peak intensity is presumably attributed to the rough interfaces and/or interpenetration between the SiO_2 and TiO_2 layers, the successful preparation of a composite coating exhibiting structural color demonstrates the great potential of this dip coating strategy for the preparation of highly functional hierarchically structured nanomaterials.

To increase the refractive index contrast between the SiO_2 composite layers and TiO_2 composite layers, future studies could pursue alternative assembly components. Since it is challenging to raise the refractive index of the TiO_2 composite layer (n~1.65), future work could consider using a lower refractive index layer than the SiO_2 composite to alternate with the high refractive TiO_2 composite. One potential substitute could be silica mesoporous films based on pluronic (triblock copolymer) templates with reported low refractive indices as low as 1.3.[37] The assembly of catechol functionalized triblock copolymers that are synthesized by our lab[38] may also complement this proposed construction of mesoporous silica alternating with TiO_2 composite for Bragg stacks.

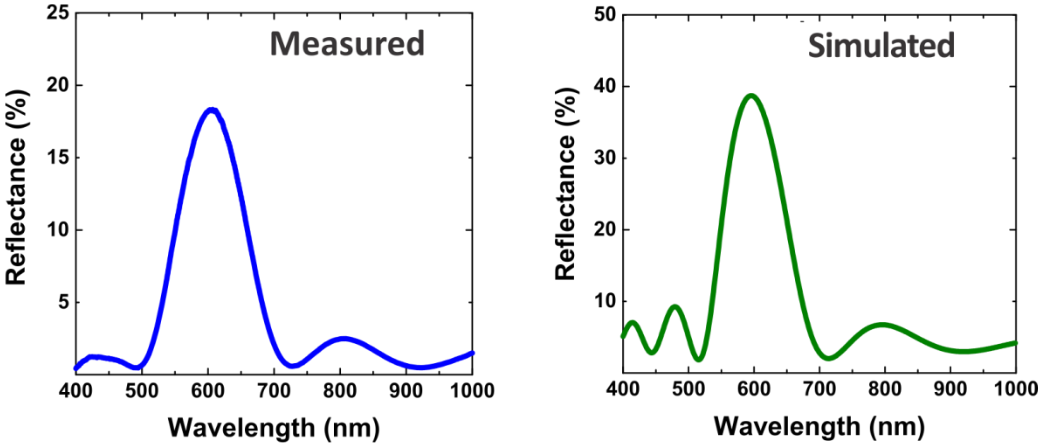

Figure 2.13. Comparison of reflectance spectra for experimental and simulated reflectance of five bilayers of SiO_2-composite/ TiO_2-composite coatings on glass substrate. The shape of the measured reflectance curve shows good agreement with the reflectance spectra. The reduction in peak intensity may be due to scattering at rough interfaces or interpenetration between the different composite layers. The measured refractive indices of individual layers at 600 nm are $n_{silica\text{-}comp}=1.47$ and $n_{titania\text{-}comp}=1.63$, by ellipsometry. The simulated peak corresponds to thicknesses of the SiO_2- and TiO_2-composite layers of 100 nm and 90 nm, respectively.

2.3 Summary and Outlook

Robust nanocomposite films were fabricated by a new aqueous catechol-based dip coating platform. Using a catechol-functionalized polyacrylamide binder in combination with inorganic nanoparticles enables the facile fabrication of robust composite coatings via a layer-by-layer process. The power of catechol as a binding motif allows composite multilayer structures to be prepared with strong adhesion of the respective coatings to substrates of arbitrary geometry and chemical composition. Since this process does not rely on electrostatic interactions, it represents a versatile addition to the preparation toolbox for functional coatings.

Additionally, the homogeneous film morphology in combination with the ability to precisely control the composite thickness and the nature of the building blocks facilitates the preparation of multilayered films. Such one-dimensionally periodic structures, containing alternating lamellae with different refractive indices (from silica and titania composites) enable the successful formation of tunable Bragg stacks with enhanced stability to solvent, pH and ionic strength. The simplicity and versatility of this new coating platform is of high interest with regards to further developments by incorporating additional functionalities such as stimuli-responsive moieties in composite films.

2.4 Experimental Section

2.4.1 Materials:

Chemicals were purchased from Sigma-Aldrich and used as received unless otherwise stated. N,N-Dimethylformamide (DMF) was collected directly from a solvent purification system (PureSolv, Innovative Technology). Silicon dioxide nanoparticles (SiO2) Ludox SM-30 (30 wt% SiO2 suspension in water, mean particle size of 7 nm) and titanium dioxide nanoparticles (TiO2) (33–35 wt% suspension in water, mean particle size of 20 nm) were purchased from Sigma-Aldrich. Hydrochloric acid (12N, fuming 37%) and sodium hydroxide (pellets) were purchased from Fischer Scientific. Thermally annealed silicon wafers with 100 nm of silicon oxide were purchased from Silicon Quest International. Poly(vinvyl chloride) tubing (5/16" ID x 7/16" OD) was purchased (Tygon R3603).

2.4.2 Synthesis of poly(dopamine acrylamide)-*co*-poly(*N*-2-hydroxypropyl)acrylamide):

The polymeric binder, poly(dopamine acrylamide)-co-poly(N-2-hydroxypropyl)acrylamide) was synthesized via post-polymerization functionalization of poly(pentafluorophenyl acrylate) (PFPA) based on a procedure adapted from the literature[28,29] (Scheme 1).

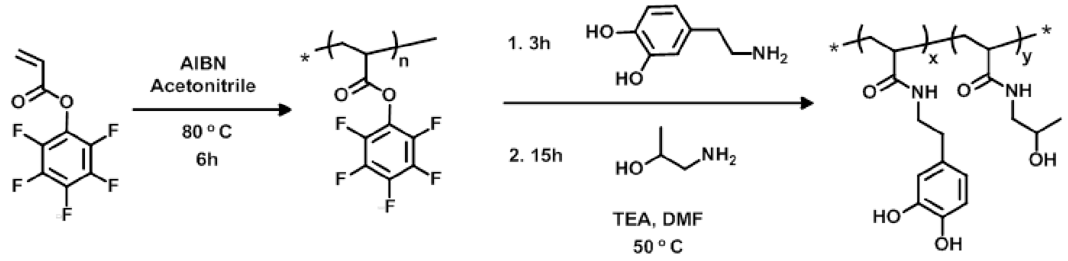

Scheme 1. Synthesis of the catechol-based polymeric binder. Free radical polymerization of pentafluorophenyl acrylate is followed by substitution of the activated ester groups with catechol moieties for adhesion and hydroxypropyl acrylamide groups for water solubility.

Pentafluorophenyl acrylate, PFPA (2.4 g, 0.010 mol, 1.0 eq) and recrystallized azobisisobutyronitrile (AIBN) (15.7 mg, 0.096 mmol, 0.01 eq) were added to a 50 mL Schlenk flask. Dry acetonitrile (12 mL) was added and the mixture was subjected to three freeze-pump-thaw cycles. The flask was sealed under argon and the mixture was stirred for 7 hrs at 80 °C. Then, 5 mL THF was added to the solution and the polymer was precipitated into 200 mL of cold methanol, followed by filtration and drying to give the product, poly(pentafluorophenyl acrylate), as white powder (2.08 gmass yield: 87.5%). M_n, GPC = 24.5 kDa, *Đ*: 2.05.

Following a previously reported post-polymerization functionalization procedure,[29] poly(pentafluorophenyl acrylate) (1.86 g, 7.79 mmol repeat units, 1 eq) and dopamine hydrochloride (0.23 g, 1.20 mmol, 0.15 eq) were dissolved in 25 mL dry DMF. Triethylamine (0.19 mL, 1.32 mmol, 0.17 eq) was added to the solution, and the mixture was stirred at 50 °C for 4 h under an argon atmosphere. Next, amino-2-propanol (0.97 mL, 11.67 mmol, 1.50 eq) and triethylamine (1.8 mL, 13.91 mmol, 1.70 eq) were added in excess to displace the remaining activated ester groups. The reaction was allowed to stir overnight under argon at 50 °C. The solution was concentrated and then purified via dialysis (MWCO: 3 kDa) using MiliQ water sparged with argon. Freeze drying gave the desired product as a white solid. The percent incorporation of catechol was determined via ^{1}H-NMR by calculating the integral ratio of the aromatic peaks to the multiplet at 3.5–3.7 ppm corresponding to the (H-(C-CH_3)-OH) protons in the aminopropanol group.

^{1}H-NMR of poly(dopamine acrylamide)-*co*-poly(N-2-hydroxypropyl)acrylamide) (500 MHz, DMSO):

δ_H: 0.95 (s, 3H, aminopropanol), 1.18–3.16 (polyacrylamide backbone), 3.66 (s, 1H, aminopropanol), 6.30–6.49 (s, 1H, Ar H catechol), 6.51–6.72 (m, 2H, Ar-H catechol), 7.06-7.98(br s, 2H, N-H amide), 8.50-8.83 (d, 2H, O-H catechol) ppm.

2.4.3 Preparation of nanocomposite coatings by dip coating:

Substrate preparation:

Silicon wafers (with 100 nm thermal oxide surface layer) and glass slides were cleaned by immersion into a freshly prepared piranha solution [consisting of 3:1 vol/vol ratio of H_2SO_4 (98%) to H_2O_2 (30%)] for 1 hr at 90 °C. This was followed by rinsing under sonication with MiliQ water, then methanol and finally dried with air.

Dip coating:

Sequential adsorption of polymer and nanoparticles was conducted on silicon wafers (with 100 nm SiO_2 surface layer) or glass slides using the following general procedure: The pH for the dip coating process was adjusted (addition of 1 M HCl or 1 M NaOH) to values for optimal binding between the respective oxide nanoparticles and catechols.[31] For SiO_2-composite coatings on Si wafers (with 100 nm thermal oxide surface layer) and glass slides, all solutions used in the deposition were adjusted to pH 1.5. The substrate was first immersed in an aqueous polymer solution (0.14 wt-%) for 10 minutes, then rinsed three times in degassed acidic water for 1 minute each. Next the polymer coated substrate was dipped in a 0.06 wt-% SiO_2 nanoparticle dispersion for 10 minutes and rinsed three times before repeating the cycle. Films were dried under a stream of air and characterized by reflectometry to estimate refractive index and thickness.

A similar procedure was used to prepare TiO_2-composite coatings. The dip coating of TiO_2 containing layers was conducted in the dark to circumvent potential photocatalytic influences of the titania nanoparticles. The first polymer deposition was carried out at pH 1.5 to adhere to the Si substrate, rinsed twice with water adjusted to pH 1.5, then once in water at pH 4.5 before immersing the polymer-coated substrate into TiO_2 nanoparticle solution at pH 4.5. All subsequent cycles for TiO_2 composite deposition used a polymer binder solution at pH 4.5.

Ten alternating layers (five bilayers) of SiO_2/TiO_2 composite were deposited onto the wafer and glass substrates with targeted layer thicknesses of 100–110 nm for SiO_2 and 90–100 nm for TiO_2 to create structurally colored coatings.

Stability tests:

Films supported on silicon substrates were immersed into THF, toluene or pH buffered solutions for 5 days at room temperature. For each time interval, films were dried and their dry thickness was estimated by reflectometry.

2.4.4 Physical characterization of composite films

Thickness and refractive index were characterized using a Filmetrics F20 spectroscopic reflectometer equipped with the standard SS-3 stage. The base line was obtained against a native oxide silicon reference wafer and spectral data was acquired over the wavelength range of 380 – 1050 nm. Each measurement was done in triplicate and the average thickness reported. Coated PVC tube samples were investigated by X-ray photoelectron spectroscopy (XPS) using a Kratos Axis Ultra XPS system with a monochromated aluminium X-ray source for elemental analysis. The films on the inner surface of the tube were visualized by field-emission scanning electron microscopy, using an FEI XL40 Sirion microscope operating with an accelerating voltage of 3 kV. Composite film surfaces were also investigated by Atomic force microscopy (AFM) on Dimension 3100 Nanoscope IV from Digital Instruments Inc. The Bragg stack coating prepared on the transparent glass substrate was photographed against a black or white background.

2.4.5 Optical model for Bragg stack coating on glass substrate:

The refractive index of the SiO_2-composite coating, n_{SiO2-c}, and the TiO_2-composite coatings, n_{TiO2-c}, were measured by ellipsometry and fit to a Cauchy model. The transfer matrix method was used to calculate the reflectance spectrum of an ideal Bragg stack of 5 SiO_2/TiO_2 composite bilayers with a peak at 600 nm.

2.5 References

1. Kim, D.-H.; Martin, D. C. *Biomaterials* **2006**, *27*, 3031–3037.
2. Wang, Z.; Zhang, J.; Xie, J.; Wang, Z.; Yin, Y.; Li, J.; Li, Y.; Liang, S.; Zhang, L.; Cui, L.; Zhang, H.; Yang, B. *J. Mater. Chem.* **2012**, *22*, 7887.
3. Puzzo, D. P.; Bonifacio, L. D.; Oreopoulos, J.; Yip, C. M.; Manners, I.; Ozin, G. A. *J. Mater. Chem.* **2009**, *19*, 3500.
4. Bonifacio, L. D.; Lotsch, B. V.; Puzzo, D. P.; Scotognella, F.; Ozin, G. A. *Adv. Mater.* **2009**, *21*, 1641–1646.
5. Hiller, J.; Mendelsohn, J. D.; Rubner, M. F. *Nat. Mater.* **2002**, *1*, 59–63.
6. Choi, S. Y.; Mamak, M.; von Freymann, G.; Chopra, N.; Ozin, G. A. *Nano Lett.* **2006**, *6*, 2456–2461.
7. Pavlichenko, I.; Exner, A. T.; Guehl, M.; Lugli, P.; Scarpa, G.; Lotsch, B. V. **2012**, 298–305.

8. Sánchez-Sobrado, O.; Calvo, M. E.; Míguez, H. *J. Mater. Chem.* **2010**, *20*, 8240.
9. Wu, Z.; Lee, D.; Rubner, M. F.; Cohen, R. E. *Small* **2007**, *3*, 1445–1451.
10. Ge, J.; Yin, Y. *Angew. Chem. Int. Ed. Engl.* **2011**, *50*, 1492–1522.
11. Melzak, K. A.; Mateescu, A.; Toca-Herrera, J. L.; Jonas, U. *Langmuir* **2012**, *28*, 12871–12878.
12. Neikirk, C. C.; Chung, J. W.; Priestley, R. D. *RSC Adv.* **2013**, *3*, 16686–16696.
13. Kharlampieva, E.; Kozlovskaya, V.; Gunawidjaja, R.; Shevchenko, V. V.; Vaia, R.; Naik, R. R.; Kaplan, D. L.; Tsukruk, V. V. *Adv. Funct. Mater.* **2010**, *20*, 840–846.
14. Tahir, M. N.; Zink, N.; Eberhardt, M.; Therese, H. A.; Kolb, U.; Theato, P.; Tremel, W. *Angew. Chemie Int. Ed.* **2006**, *45*, 4809–4815.
15. Chung, H.; Ohno, K.; Fukuda, T.; Composto, R. J. *Nano Lett.* **2005**, *5*, 1878–1882.
16. Balazs, A. C.; Emrick, T.; Russell, T. P. *Science* **2006**, *314*, 1107–1110.
17. Izquierdo, A.; Ono, S. S.; Voegel, J.-C.; Schaaf, P.; Decher, G. *Langmuir* **2005**, *21*, 7558–7567.
18. Nogueira, G. M.; Banerjee, D.; Cohen, R. E.; Rubner, M. F. *Langmuir* **2011**, *27*, 7860–7867.
19. Decher, G. In *Multilayer Thin Films*; Wiley-VCH Verlag GmbH & Co. KGaA: Weinheim, Germany, 2012; pp 1–21.
20. Decher, G. *Science (80).* **1997**, *277*, 1232–1237.
21. Vig, J. R. *J. Vac. Sci. Technol. A* **1985**, *3*, 1027.
22. Hsieh, M. C.; Farris, R. J.; McCarthy, T. J. *Macromolecules* **1997**, *30*, 8453–8458.
23. Holten-Andersen, N.; Harrington, M. J.; Birkedal, H.; Lee, B. P.; Messersmith, P. B.; Lee, K. Y. C.; Waite, J. H. *Proc. Natl. Acad. Sci. U. S. A.* **2011**, *108*, 2651–2655.
24. Min, Y.; Hammond, P. T. *Chem. Mater.* **2011**, *23*, 5349–5357.
25. Lee, H.; Dellatore, S. M.; Miller, W. M.; Messersmith, P. B. *Science* **2007**, *318*, 426–430.
26. Sun, J.; Su, C.; Zhang, X.; Yin, W.; Xu, J.; Yang, S. *Langmuir* **2015**.
27. Liaqat, F.; Tahir, M. N.; Schechtel, E.; Kappl, M.; Auernhammer, G. K.; Char, K.; Zentel, R.; Butt, H.-J.; Tremel, W. *Macromol. Rapid Commun.* **2015**, n/a – n/a.
28. Eberhardt, M.; Mruk, R.; Zentel, R.; Théato, P. *Eur. Polym. J.* **2005**, *41*, 1569–1575.
29. Xu, L. Q.; Jiang, H.; Neoh, K.-G.; Kang, E.-T.; Fu, G. D. *Polym. Chem.* **2012**, *3*, 920.
30. Wei, Q.; Becherer, T.; Noeske, P.-L. M.; Grunwald, I.; Haag, R. *Adv. Mater.* **2014**, *26*, 2688–2693, 2615.
31. Malisova, B.; Tosatti, S.; Textor, M.; Gademann, K.; Zürcher, S. *Langmuir* **2010**, *26*, 4018–4026.
32. Lana-villarreal, T.; Rodes, A.; Pe, J. M.; Go, R. **2005**, No. 19, 12601–12611.
33. Leslie, D. C.; Waterhouse, A.; Berthet, J. B.; Valentin, T. M.; Watters, A. L.; Jain, A.; Kim, P.; Hatton, B. D.; Nedder, A.; Donovan, K.; Super, E. H.; Howell, C.; Johnson, C. P.; Vu, T. L.; Bolgen, D. E.; Rifai, S.; Hansen, A. R.; Aizenberg, M.; Super, M.; Aizenberg, J.; Ingber, D. E. *Nat Biotech* **2014**, *32*, 1134–1140.
34. Ohko, Y.; Utsumi, Y.; Niwa, C.; Tatsuma, T.; Kobayakawa, K.; Satoh, Y.; Kubota, Y.; Fujishima, A. *J. Biomed. Mater. Res.* **2001**, *58*, 97–101.

35. Abate, A. R.; Lee, D.; Do, T.; Holtze, C.; Weitz, D. A. *Lab Chip* **2008**, *8*, 516–518.
36. Lee, H.; Sample, C.; Cohen, R. E.; Rubner, M. F. *ACS Macro Lett.* **2013**, *2*, 924–927.
37. Falcaro, P.; Grosso, D.; Amenitsch, H.; Innocenzi, P. *J. Phys. Chem. B* **2004**, *108*, 10942–10948.
38. Mattson, K. M.; Latimer, A. A.; McGrath, A. J.; Lynd, N. A.; Lundberg, P.; Hudson, Z. M.; Hawker, C. J. A Facile Synthesis of Catechol-Functionalized Poly(ethylene Oxide) Block and Random Copolymers. *J. Polym. Sci. Part A Polym. Chem.* **2015**, *53*, 2685–2692.

3 pH Responsive Cross-linked Block Copolymer Particles[†]

3.1 Introduction

The generation of nanostructured materials is a critical for applications requiring controlled optical, electrical, and physical behavior. While the size and shape dependent novel properties of inorganic nanoparticles[1] have been well-studied since the 1950s,[2] recent development of polymer-based nanoparticles may enable access to more dynamic or complex architectures not accessible to inorganic counterparts such self-assembling patchy particles[3] and multicompartment nanoparticles.[4]

Dynamic and well-defined nanostructured particles would be valuable for biological and photonic applications, among many others. Shape anisotropic particles have demonstrated unique pharmacokinetics as drug carriers in addition to their value for fundamental colloidal assembly studies.[5] An ideal nanomaterials synthetic platform would require the ability to direct particle shape, inner morphology and response to stimuli. However, it remains challenging to address all these three aspects within a single system. Current examples only partially fulfill these requirements. For instance, anisotropic particles have been prepared mechanically stretching spheres[5] or micromolding of liquid particle

---

[†] Reproduced in part with permission: Klinger, D.; Wang, C. X.; Connal, L. A.; Audus, D. J.; Jang, S. G.; Kraemer, S.; Killops, K. L.; Fredrickson, G. H.; Kramer, E. J.; Hawker, C. J. *Angew. Chem., Int. Ed.* **2014**, *53*, 7018-22. Copyright 2014, Wiley. License Number: 3857370378496

precursors.[6] But neither of these methods provides control over the inner morphology of the particle.

To achieve particles with periodic internal structures, we pursue the assembly of block copolymers within droplets.[7–10] The microphase separation of block copolymers is influenced by the polymer molecular weight, composition, architecture, interaction parameter between segments and block volume fraction. Self-assembled morphologies of AB diblock copolymers can range from alternating lamellae to cylindrical to spherical domains in order of increasingly asymmetric block volume fractions. The use of a single surfactant (or no surfactant) to assemble symmetric block copolymer results in onion-like particles with radial morphology; due to preferential wetting of one block by the surfactant layer surrounding the dispersed particle.

Interfacial engineering is necessary to control the phase separation of block copolymers particles. The associated self-assembly of block copolymers in thin films is instructive here. For thin films, the introduction of a neutral layer, typically a random copolymer, between the block copolymer and substrate and/or air can induce a perpendicular orientation of lamellae and cylinders.[12] In the case of particles, a neutral layer can be derived from a mixture of two surfactants to orient the block copolymer domains relative to the surrounding medium.

This dual surfactant strategy was first reported by Jeon et al. and resulted in ellipsoidal particles with axially stacked lamellae of poly(styrene)-*b*-poly(butadiene).[9] A similar ellipsoidal structure was assembled from symmetric poly(styrene-b-2vinylpyridine), (PS-*b*-P2VP) by Jang. et al. through the use of poly(styrene) coated Au nanoparticles and cetyltrimethyl ammonium bromide (CTAB).[11] However, stimuli-responsive behavior was not demonstrated with these block copolymer assemblies. This work aims to address the formation of multifunctional block copolymer based nanoparticles that combine shape anisotropy, internal morphology, and stimuli-responsiveness.

Herein, we report the development of a facile and powerful strategy for the preparation of functional, dynamic particles that serves as a broad platform for nanoscale materials. The use of functional surfactant mixtures to control the phase separation of the symmetric PS-*b*-P2VP block copolymers within dispersed nanoparticles may allow for selective switching between the three distinct internal morphologies shown in Figure 3.1, with the final result being the controlled synthesis of spherical or elongated particles. This approach further allows for secondary chemistry, such as cross-linking of the P2VP domains, to be carried out. These multifunctional particles not only combine an overall shape anisotropy with a well-defined internal morphology but also display a reversible pH-dependent swelling of the P2VP layers.

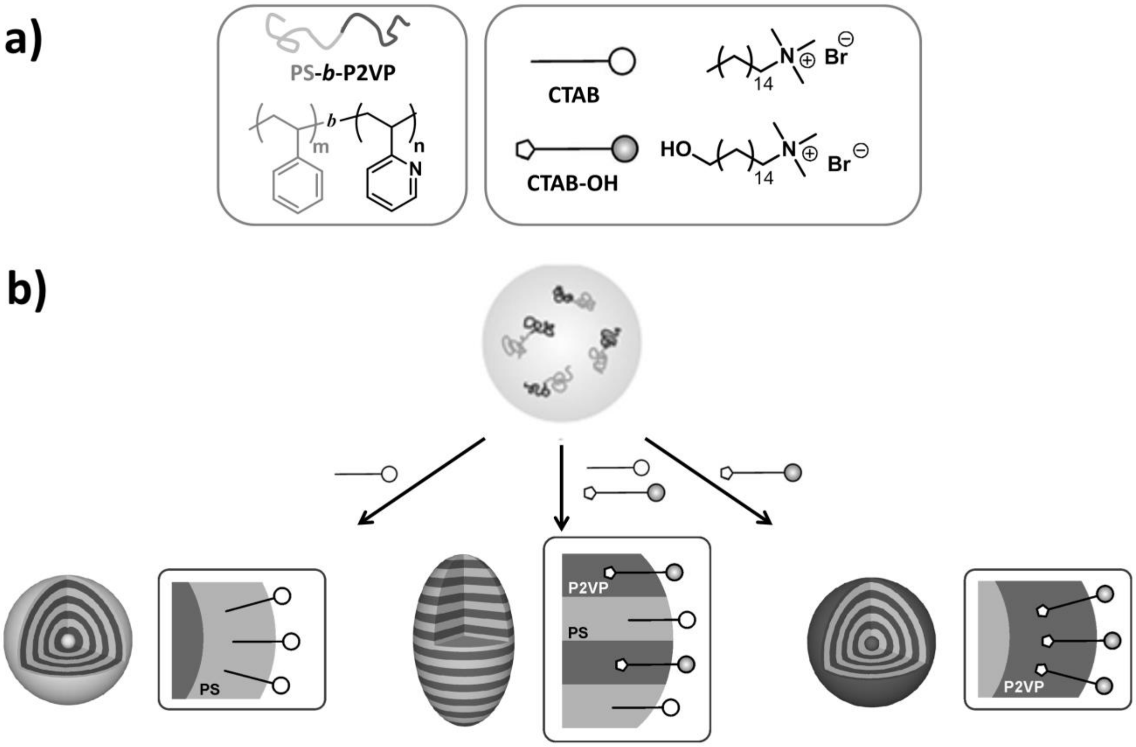

Figure 3.1. Scheme of components used for particle assembly and expected morphologies using mixed surfactant directed assembly. a) Poly(styrene-*b*-2-vinyl pyridine) (PS-*b*-P2VP) diblock copolymer is assembled within droplets using two surfactants, cetyltrimethylammonium bromide (CTAB) and 16-hydroxy-N,N,N-trimethylhexadecan-1-ammonium bromide (CTAB-OH). **b)** Graphic depicting the expected particle morphology containing radial or axially oriented PS-*b*-P2VP lamellar based on the surfactant content.

Finally, the axially stacked internal lamellae morphology translates to an anisotropic swelling profile, thus resulting in a pH-triggered dynamic shape change as a result of a preferential stretching/shrinking of the elongated particles along the long axis.

3.2 Results and discussion

3.2.1 Directing BCP phase separation through mixed surfactant assembly

Our approach to controlling the interaction between block copolymers (BCPs) and the surrounding medium employs functional surfactants in combination with solvent evaporation driven assembly.[9,11,12] In this design, each surfactant would be preferential for one specific domain (Figure 3.1). Consequently, intermediate ratios of the two surfactants would lead to nonpreferential interactions, in effect a neutral interface. To investigate the effect of surfactant ratio on the internal particle morphology, the block copolymer, PS-*b*-P2VP (molecular weight:102k–97k, *Đ:*1.05, Polymer Source) ,was dissolved in chloroform, mixed with aqueous solution containing surfactant and emulsified in a sonication bath (Figure 3.2).[11] After evaporation of the chloroform over 2 days at 30 °C, the particles are stained and characterized by transmission electron microscopy (TEM). The P2VP domains appear dark due to selective iodine staining.

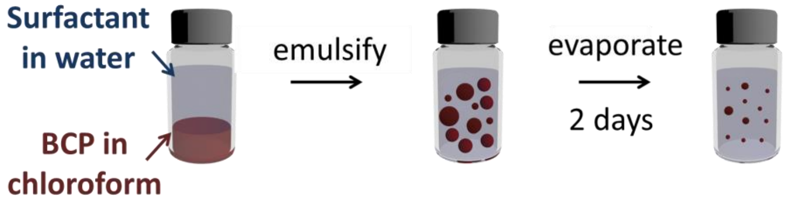

Figure 3.2. Schematic representation of solvent evaporation driven assembly procedure. Ultrasonication is used to emulsify block copolymer (BCP) chloroform droplets in aqueous surfactant solution, followed by evaporation of the chloroform to solidify particles. Based on literature procedure.[11]

In initial experiments with 100% cetyltrimethylammonium bromide (CTAB) as the surfactant, the expected radial morphology was obtained with polystyrene as the outermost layer as a consequence of hydrophobic interactions. The ability of the 2VP groups to serve as hydrogen-bond acceptors was exploited when designing a surfactant that would exhibit a preferential interaction with the P2VP phase.[10] A hydroxy group was, therefore, incorporated at the ω-position of CTAB to give HO-CTAB (Figure 3.1).[13] Significantly, the use of HO-CTAB resulted in the anticipated reverse behavior, and nanoparticles with P2VP as the outermost layer of an "inverse onion" morphology were obtained (Figure 3.3). This ability to switch the layer sequence by switching surfactants suggests that a neutral layer will be obtained by adjusting the composition of the surfactant mixture. To test this hypothesis, a series of PS-b-P2VP particles was prepared using mixtures with various compositions of the two surfactants, whereby $f_{\text{CTAB-OH}}$ is the mass fraction of HO-CTAB in relation to the total surfactant concentration. The TEM images in Figure 3.3 demonstrate that tuning the mass fraction of surfactants is a facile technique to control both the self-assembly process and the particle shape. Radial structures with a PS layer clearly at the surface are obtained at high CTAB concentrations (≤0.50).

Significantly, as the mass fraction of HO-CTABis increased above a 1:1 ratio ($f_{\text{CTAB-OH}} \approx 0.50$), a distinct morphology and shape change is observed to give spherical onions as well as nonspherical particles with a mixture of radially and axially stacked lamellae morphologies (Figure 3.3). A distinct transition is then observed at $f_{\text{CTAB-OH}}$ between 0.70 and 0.80, where only the desired stacked lamellae morphology and ellipsoidal particle shape are observed. This confirms the validity of this mixed surfactant approach and the existence of a specific range of HO-CTAB/CTAB ratios for which the interfacial energies between the surfactants layer and the

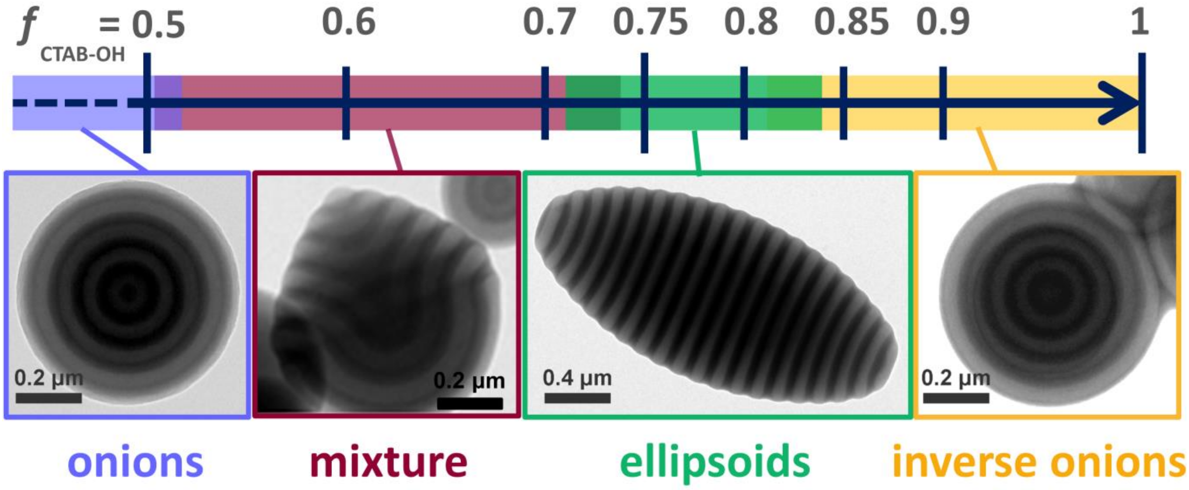

Figure 3.3. Influence of surfactant ratio on particle morphology. PS-b-P2VP (MW = 102k–97k Da) diblock copolymer particles are prepared in the presence of a binary mixture of surfactants, CTAB and CTAB-OH. Mass fraction of HO-CTAB, is denoted by $f_{\text{CTAB-OH}}$. Representative transmission electron microscopy (TEM) images of assembled PS-b-P2VP for each distinct morphological region: onions, mixtures containing combination of axial and radial oriented lamellar within "intermediate" structures, ellipsoids, and inverse onions. P2VP domains are stained with iodine for imaging contrast, appearing dark grey while PS appears light grey.

domains of the BCP are balanced. For the mid-point of the neutral range, $f_{\text{CTAB-OH}}$=0.75, the interfacial balance results in all the particles assuming an ellipsoidal shape, with axially stacked lamellae that persistent throughout the entire particle as shown by reconstructive tomography (Figure 3.4b). The formation of ellipsoids from excess CTAB-OH surfactant relative to CTAB (as opposed to an equimolar ratio of two surfactants) was likely due to the higher water solubility and lower surface activity of the CTAB-OH surfactant compared to the CTAB surfactant.[13] Nonetheless, the ability to reproducibly and exclusively obtain radially or axially stacked lamellae in BCP particles at a specific surfactant compositions demonstrates interfacial control. This strategy is a simple and scalable method for nanostructured polymer ellipsoids.

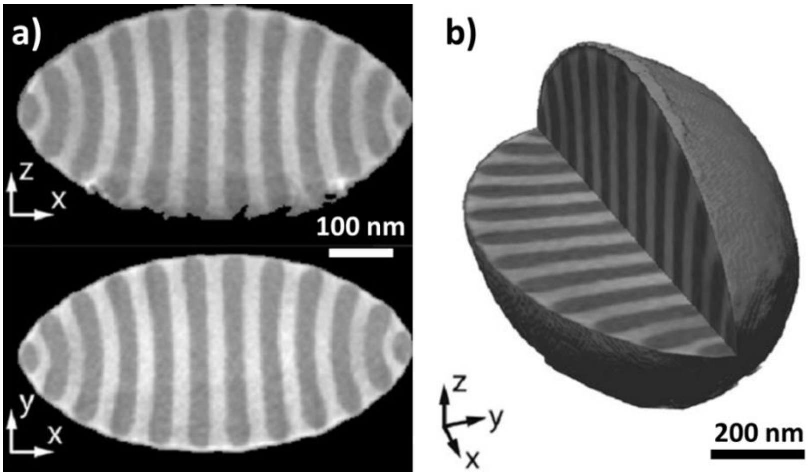

Figure 3.4. Dark field electron micrographs of ellipsoidal particle and reconstruction. a) 2D slices extracted from the full 3D reconstructed image, and b) reconstructed 3D image from TEM tomography. PS domains are depicted as dark grey and the P2VP domains are white. Reconstruction by Dr. Stephan Kraemer.

3.2.2 Effect of molecular weight on particle aspect ratio:

Importantly, the aspect ratio of these shape-anisotropic particles is not a fixed parameter, since the elongation is determined by the counterbalance of three different contributions to the free energy: a stretching penalty term for PS-b-P2VP, the interfacial energy between PS and P2VP, and the interfacial energy between PS-b- P2VP and the surrounding medium. Theoretical calculations indicate that it is possible to shift this balance and thus tune the particle aspect ratio.[11] To understand the effect of the BCP molecular weight, three different lamellae forming PS-b-P2VP diblock copolymers with molecular weights of 102k--97k, 40.5k--41k, and 20k--20kDa were examined. By plotting both the theoretical and experimental aspect ratio (A) versus the long axis (L) of ellipsoidal particles (formed from a HO-CTAB/CTAB ratio of 3:1, that is, $f_{\text{CTAB-OH}}$=0.75; (Figure 3.4) it is evident that elongation not only increases with block copolymer molecular weight but also with particle size. Regarding the latter, the theoretical model predicts that larger droplets/particles are easier to stretch since the surface energy of the droplets decrease

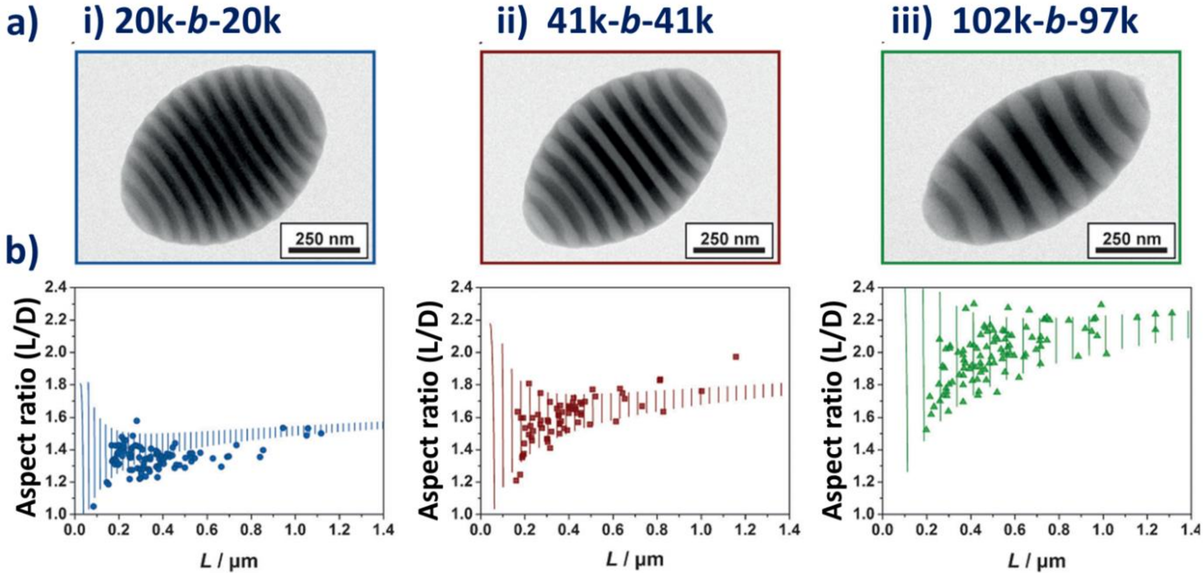

Figure 3.5. Influence of BCP molecular weight on the shape anisotropy of ellipsoidal PS-b-P2VP nanoparticles with axially stacked lamellae obtained for neutral wetting conditions at a 3:1 ratio of HO-CTAB/CTAB ($f_{CTAB\text{-}OH}$=0.75). a) TEM images of similar sized (*L*≈550nm) BCP nanoparticles obtained from PS-b-P2VP diblock copolymers with molecular weights of **i)** 20k–20k, **ii)** 40.5k–41k, and **iii)**102k–97kDa **b)** plots of experimental (•) and theoretically predicted (—)aspect ratios (*L*/*D*) as a function of the long axis (*L*) for representative populations of the three respective diblock copolymer molecular weights. Particles dimensions measured using ImageJ. [†]Theoretical model by Dr. Debra Audus.

relative to the bulk elastic and interfacial free-energy contributions on increasing the particle size. This strong influence of the droplet volume on elongation is demonstrated by an increase in the aspect ratio with particle size (Figure 3.4b) Regarding the influence of the

BCP molecular weight, the theoretical model predicts that it is easier to stretch particles consisting of BCPs with higher molecular weights since the energetic penalty for chain stretching is higher for shorter polymers. This assumption is strongly supported by the results, where decreasing the overall MW of the symmetrical PS-b-P2VP block copolymers decreases the aspect ratio of the colloids. As shown in Figure 3.5a, TEM images of similarly sized particles (ca. 550nm in length) demonstrate that different aspect ratios are obtained for similar *L* values, and a direct correlation between the number of layers per particle and molecular weight is obtained.

3.2.3 Effect of pH on conformation of cross-linked particles:

Having demonstrated the ability to tune the shape and internal morphology, the introduction of stimuli-responsiveness was investigated by taking advantage of the nucleophilicity and basic character of the 2VP units present in the PS-b-P2VP block copolymer. To render the ellipsoidal particles pH-responsive while maintaining their integrity, the P2VP chains were cross-linked by the addition of 1,4-dibromobutane (DBB), thereby transforming the P2VP domains into hydrogel materials[14] (Scheme 3.1). The use of methanol as a co-solvent waskey to ensure penetration of the DBB cross-linker. Significantly, cross-linking did not change the internal morphology or shape of the particles at neutral pH (Figure 3.6a) However, lowering the pH value results in the remaining 2VP units being protonated, thus causing the P2VP hydrogel layers to undergo significant swelling. As these hydrogel layers are connected by glassy PS lamellae, the swelling results in a dramatic elongation of the ellipsoids along the long axis *L*. Particles with 8 lamellae swell from around 550nm at pH 7 to approximately 1400nm at pH 3, with TEM analysis showing a unique shape change from ellipsoidal to an "accordion-like",

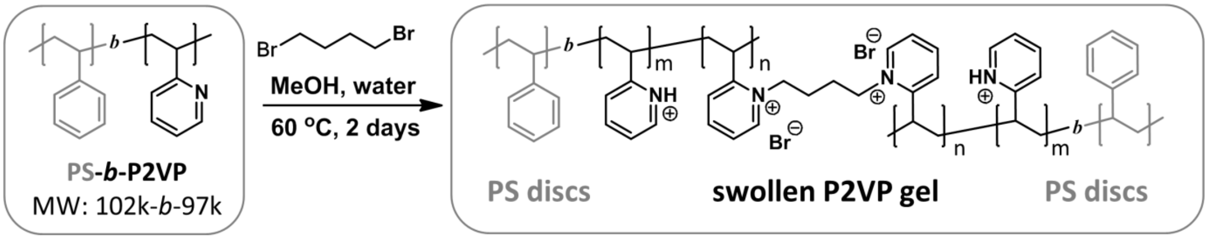

Scheme 3.1. Cross-linking scheme. The cross-linking agent dibromobutane (DBB) quarternizes the pyridyl moieties of the P2VP to pyridinium moieties[15] and form a pH responsive network.

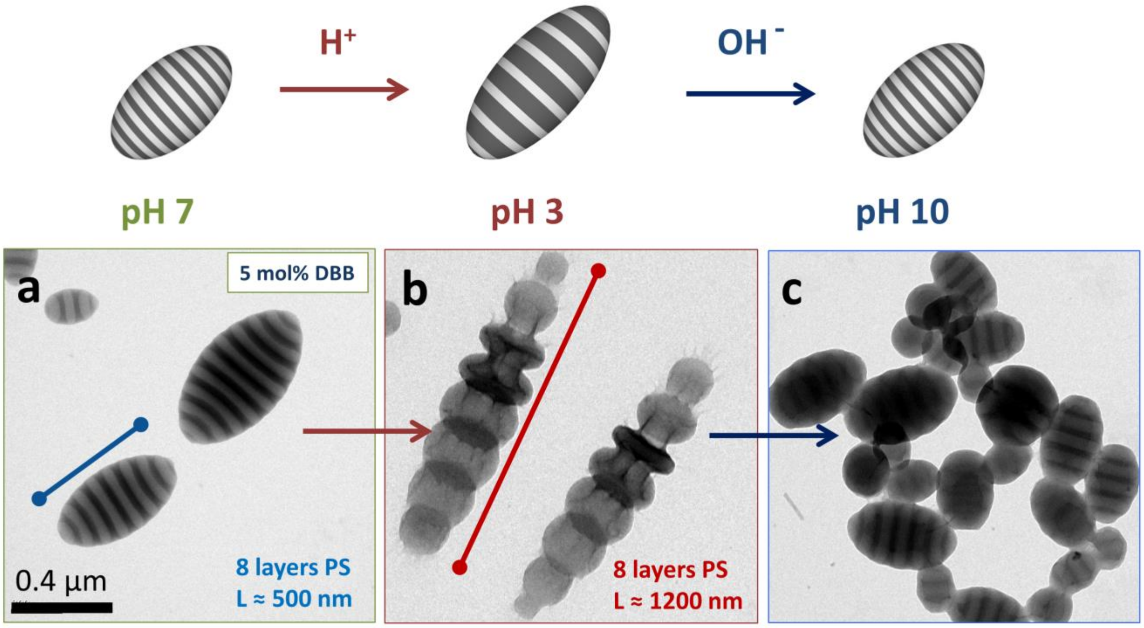

Figure 3.6. Schematic illustration of cross-linked, pH responsive BCP particles and their representative TEM micrographs. a) After addition of cross-linker dibromobutane (DBB) in MeOH (5 mol% with respect to 2VP groups), particle assembly remains intact. b) Under acidic conditions P2VP domains are protonated and become more hydrophilic, which result in their swelling. c) Upon addition of base, pyridine moieties are deprotonated and P2VP domains deswell and return to their original domain size

segmented structure (Figure 3.6b). Since the short axis (*D*) of the particles remains unaltered, this pH-induced shape change corresponds to a more than 250^% increase in the aspect ratio.

Most notably, these dramatic changes are reversible: increasing the pH value from 3 to 10 results in the initial stacked lamellae structure and ellipsoidal shape of the elongated particles being fully restored (Figure 3.6c). In direct contrast, non-cross-linked materials do not undergo reversible switching or dramatic shape changes. Complete disintegration of the ellipsoid particles into glassy PS nanodiscs with P2VP coronas occurs under acidic conditions (Figure 3.7). All attempts to reverse this process by increasing the pH value failed, with clusters of nanodiscs remaining. In addition, attempts to exploit the responsive properties of the spherical, radial lamella structures, either before or after cross-linking, did not lead to any changes in shape or morphology. The reversible shape transformation for the ellipsoidal, stacked lamella particles, therefore, represents a unique platform directing shape, morphology and selective cross-linking.

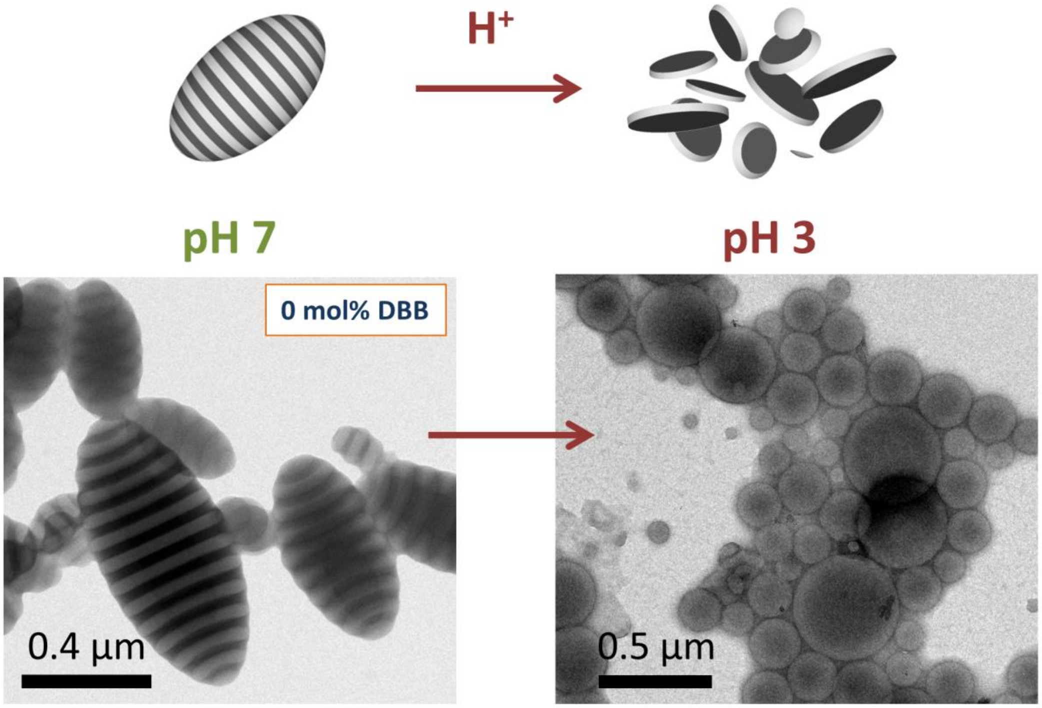

Figure 3.7. Uncross-linked particles dissociate into PS discs with P2VP corona. At pH 3, below the pKa of 2-vinyl pyridine, P2VP become water soluble and surrounds the glassy PS domains.

3.2.4 Effect of degree of P2VP cross-linking on particle conformation:

BCP particle dispersions were subject to different amounts of cross-linker (1, 2, 12.5 and 25 mol% relative to the 2VP units), and the particle conformation was investigated by TEM (Figure 3.8). Under acidic conditions, a greater degree of swelling in the P2VP layers was observed for particles subject to lower addition of cross-linker. Representative micrographs demonstrate that this swelling can be easily reversed by the addition of base to particle dispersions.

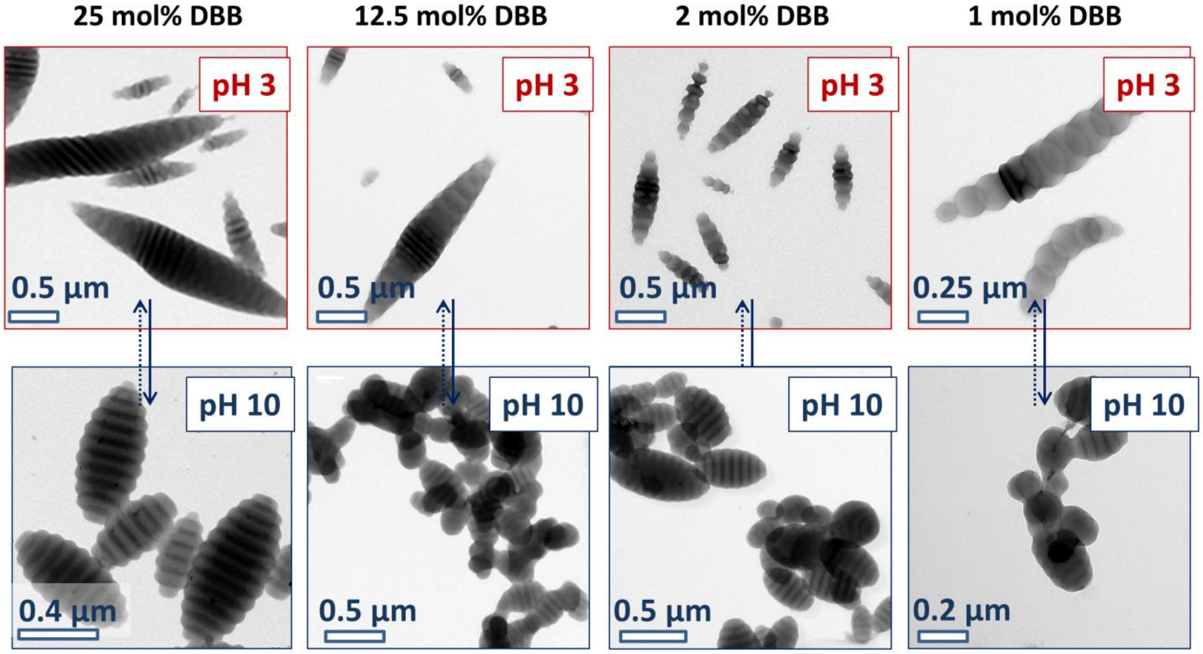

Figure 3.8. Particle morphology for different equivalence of dibromobutane (DBB) cross-linker. TEM images depict the particles containing P2VP domains swollen in pH 3 acidic conditions followed by addition of base to collapse the particles back to their original conformation. The lower equivalence of cross-linker added (mol % relative to units of 2VP) leads to greater degree of swelling of the P2VP domains.

The ability to vary the thickness and hydration of the P2VP network opens up the possibility to tune the optical contrast between glassy PS layers alternating with swollen P2VP domains.[14,16] As prepared, the dispersion of uncross-linked block copolymer particles appears milky by eye, where they are completely glassy and scatter light (Figure 3.8a). In contrast, after these particles are subjected to the crosslinking procedure with dibromobutane (100 mol% relative to the 2VP units), and swollen at pH 3, an iridescent solution is observed (Figure 3.8b). The hydrated cross-linked and quarternized P2VP network, alternating with the glassy PS layers of higher refractive index could potentially lead to selective light

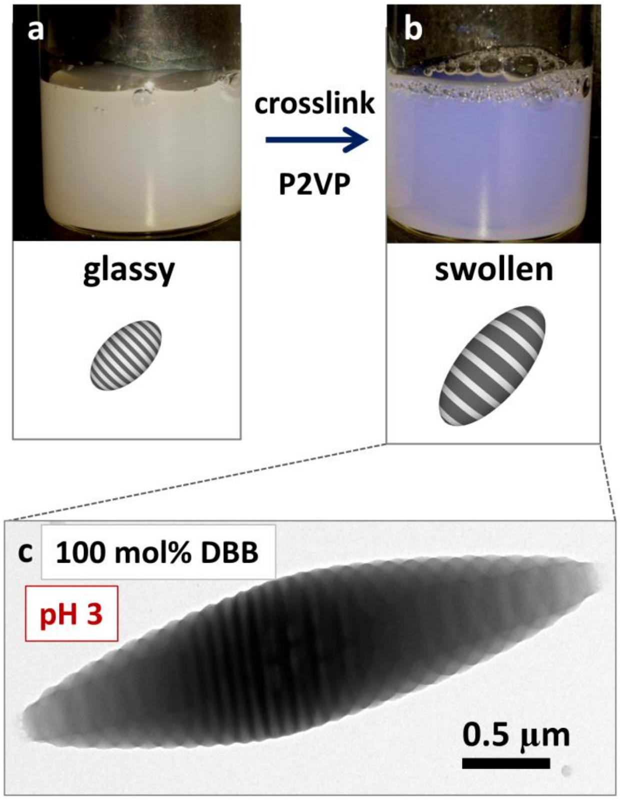

Figure 3.9. Comparison of uncross-linked versus cross-linked ellipsoidal particles dispersed in aqueous solution. **a)** Photograph of the dispersion of uncross-linked BCP particles which appears milky at pH 7 due to light scattering by the micrometer scale glassy assemblies. **b)** Iridescent appearance of highly swollen cross-linked BCP particle (100 mol % dibromobutane cross-linker relative to 2VP units) dispersion at pH 3. **c)** TEM micrograph of swollen P2VP domains within BCP particle, P2VP domains stained with iodine.

reflection or structural coloration.[17,18]

Dispersions of particles crosslinked with intermediate levels of dibromobutane do not exhibit significant iridescence. Since the BCP particles are not aligned and free to float in solution (even for the 100 % cross-linked system), we hypothesize that the ellipsoidal particles may align into a pseudo-nematic phase similar to those observed in liquid crystals.[19] Assembly of larger PS-P2VP particles containing a greater number of BCP lamellae may improve the quality of pigments and increase the particle reflectivity by constructive thin-film interference.[17]

3.3 Summary

We have demonstrated a facile method to control particle shape and morphology through the use of tailored, mixed surfactant systems to tune surface interactions. For PS-b-P2VP particles, three disparate morphologies—spherical particles consisting of radial layers with either PS or P2VP as the outer layer and ellipsoidal particles containing axially stacked lamellae—could be reproducibly and exclusively obtained. In addition, control over the aspect ratio could be realized by adjusting the molecular weight of the block copolymer. In an interesting demonstration of the interplay between chemistry, surface interactions, and nanoscale morphology, cross-linking of the P2VP domains allows the pH-responsiveness of the 2VP moieties to be exploited, thereby leading to shape- and structure-responsive particles. Preliminary results also suggest that it may be possible to tune the refractive index contrast between glassy PS layers alternating with swollen P2VP domains.

3.4 Experimental

3.4.1 Materials

Cetyltrimethylammoniumbromide (CTAB, Sigma Aldrich, ≥ 99%), trimethylamine (4.2 M in ethanol, Sigma Aldrich), Poly(styrene-block-2-vinyl pyridine) (PS-b-P2VP) (M_n= 102k–97k, 40.5k–41k, and 20k–20k, Polymer Source Inc., CAS 24980-54-9), and 16-bromo-1-hexadecanol, (Astatech Inc, 95%) were used as received. Chloroform and methanol were purchased from Fisher Scientific. Ultrahigh purity deionized water (18.2MΩ·cm) was obtained from buffer grade Mili-Q Advantage A10 water purification system by MilliPore.

3.4.2 Particle synthesis

PS-b-P2VP based particles were prepared by a combination of solvent evaporation from emulsion droplets and interfacial surfactant directed assembly. The droplet phase consisted of 1 wt% polymer solution prepared by dissolving PS-b-P2VP in chloroform. The continuous phase was composed of 0.1 wt% surfactant in MiliQ deionized water, where the surfactant was either CTAB or a combination of CTAB and CTAB-OH. CTAB-OH (16-hydroxy-N,N,N-trimethylhexadecan-1-ammonium bromide) was synthesized according to a literature procedure[13]

Sonication method: 1 mL of droplet phase and 10 mL of surfactant solution are combined in a 20 mL vial and capped. The mixture is vortexed for 30s, emulsified in an ultrasound bath for 2 min, and the chloroform evaporated by stirring open vials containing the emulsions for 2 days at 30 °C.

3.4.3 Particle characterization

Transmission electron microscopy was performed on a Tecnai FEI T20 using a single tilt holder and images recorded on a CCD camera. Samples were washed with MiliQ water and centrifuged 3 times to remove surfactant. The purified solutions were then drop cast onto carbon coated copper grids (CF300-Cu, Electron Microscopy Sciences) and stained with iodine vapor for 3 minutes before imaging. Iodine forms a charge transfer complex with the nitrogen atom in the 2-vinyl pyridine,[20] selectively staining the P2VP domains for contrast against the PS domains. For the tomography, a tilt series of bright field images was recorded in the angle range from -70° to +70° with angle increments following the Saxton scheme. An in-house software package developed in Matlab was used to normalize the relative intensities, align the images with help of fiducial markers and calculate the three- dimensional scattering density map based on the filtered back projection (FBP) approach. Visualization of 2D slices also done in Matlab.

3.4.4 Cross-linking procedure for P2VP domains and pH response

A solution of of 1,4-dibromobutane in methanol (0.1 mg/mL) was added to 5mL of the purified particle dispersion (0.05 wt% solid content) and stirred at 60 °C for 2 days. The table below summarizes the different amounts of cross-linker tested.

The morphology of these cross-linked particles as a function of pH, was investigated by addition of 1M hydrochloric acid to adjust the pH of these solutions to pH 3. The mixtures were sonicated and vortexed before sample preparation for TEM investigation. In tandem, the uncross-linked particles were subject to the same treatment. To collapse the P2VP domains and reverse this shape change, 1M sodium hydroxide was added until the solution reached pH 10.

3.5 References

1. Lohse, S. E.; Murphy, C. J. *J. Am. Chem. Soc.* **2012**, *134*, 15607–15620.

2. Turkevich, J.; Stevenson, P. C.; Hillier, J. *Discuss. Faraday Soc.* **1951**, *11*, 55–75.

3. Schacher, F. H.; Rupar, P. A.; Manners, I. *Angew. Chemie - Int. Ed.* **2012**, *51*, 7898–7921.

4. Zhu, J.; Zhang, S.; Zhang, K.; Wang, X.; Mays, J. W.; Wooley, K. L.; Pochan, D. J. *Nat. Commun.* **2013**, *4*, 2297.

5. Champion, J. A.; Katare, Y. K.; Mitragotri, S. *J. Control. Release* **2007**, *121*, 3–9.

6. Rolland, J. P.; Maynor, B. W.; Euliss, L. E.; Exner, A. E.; Denison, G. M.; DeSimone, J. M. *J. Am. Chem. Soc.* **2005**, *127*, 10096–10100.

7. Yabu, H.; Higuchi, T.; Shimomura, M. *Adv. Mater.* **2005**, *17*, 2062–2065.

8. Hales, K.; Pochan, D. J. *Curr. Opin. Colloid Interface Sci.* **2006**, *11*, 330–336.

9. Jeon, S.-J.; Yi, G.-R.; Yang, S.-M. *Adv. Mater.* **2008**, *20*, 4103–4108.

10. Deng, R.; Liu, S.; Li, J.; Liao, Y.; Tao, J.; Zhu, J. *Adv. Mater.* **2012**, *24*, 1889–1893.

11. Jang, S. G.; Audus, D. J.; Klinger, D.; Krogstad, D. V; Kim, B. J.; Cameron, A.; Kim, S.-W.; Delaney, K. T.; Hur, S.-M.; Killops, K. L.; Fredrickson, G. H.; Kramer, E. J.; Hawker, C. J. *J. Am. Chem. Soc.* **2013**, *135*, 6649–6657.

12. Deng, R.; Liang, F.; Li, W.; Liu, S.; Liang, R.; Cai, M. *Small* **2013**, 1–5.

13. Davey, T. W.; Ducker, W. A.; Hayman, A. R. *Langmuir* **2000**, *16*, 2430–2435.

14. Kang, Y.; Walish, J. J.; Gorishnyy, T.; Thomas, E. L. *Nat. Mater.* **2007**, *6*, 957–960.

15. Kuang, M.; Duan, H.; Wang, J.; Jiang, M. *J. Phys. Chem. B* **2004**, *108*, 16023–16029.

16. Lim, H. S.; Lee, J.; Walish, J. J.; Thomas, E. L. **2012**, No. 10, 8933–8939.

17. Alfrey, T.; Gurnee, E. F.; Schrenk, W. J. *Polym. Eng. Sci.* **1969**, *9*.

18. Kang, Y.; Walish, J. J.; Gorishnyy, T.; Thomas, E. L. *Nat. Mater.* **2007**, *6*, 957–960.

19. Crawford, G. P.; Zumer, S. CRC Press, 1996.

20. Aronson, S.; Wilensky, S. B. *J. Polym. Sci. Part A Polym. Chem.* **1988**, *26*, 1259–1262.

4 Mesofluidic Generation Of Block Copolymer Particles: Towards Colloidal Bragg Reflectors

4.1 Introduction

From the shape shifting mimic octopus to the iridescent longfin squid, cephalopods provide guiding principles for the design of dynamic photonic materials. Within the skin of the longfin squid, light-reflecting cells termed iridophores,[1] (alternatively iridocytes) are composed of dense reflective protein platelets[3] that alternate with clear extracellular matrix (Figure 4.1a). These dynamic intracellular Bragg stacks exhibit highly desirable traits for camouflage, displays and sensors such as the ability to rapidly tune the wavelength of the reflected light over a wide spectrum and with broadband reflectivity.

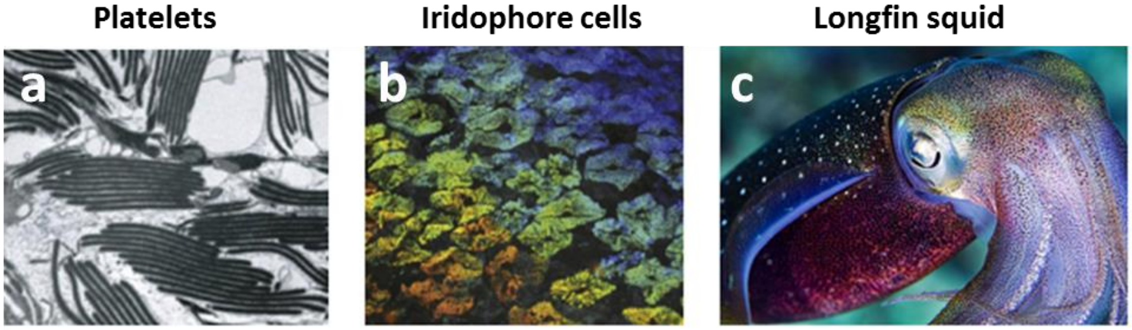

Figure 4.1 Structural hierarchy of specialized light reflecting cells (iridophores) within squid skin. Reproduced with permission.[2] **a)** Reflectin protein platelets within extracellular matrix.[3] Copyright 2012 AAAS. **b)** Iridophore cells with varied swelling (and color response) to an acetylchlorine chemical gradient.[1] Copyright 2010 Elsevier **c)** Iridescent longfin inshore squid, *Loligo pealeii*.[2] Copyright 2012 Scientific American.

Inspired by this system, researchers have developed responsive synthetic Bragg stack/multilayered films as environmental photonic sensors,[4] stealth coatings[5] and displays.[6] There is a growing interest in colloidal based systems or photonic particles for similar applications. Colloidal particles provide a dispersible system and could potentially have a quicker response time to stimuli as compared to thin films. Confining polymeric Bragg stacks into colloidal particles would give access to a new class of dynamic photonic materials that enable rapid color change in aqueous dispersion. The selective reflection of color has been demonstrated from static assemblies of core-shell particles packed within a complex microcapsule but these systems require distinct assemblies to access the full color spectrum.[7] Control over domain size and refractive index contrast within a dynamic system is necessary to tune the color.

Chapter 3 demonstrated a facile method to prepare colloidal Bragg reflectors in the form of block copolymer (BCP) ellipsoidal nanoparticles with an axially stacked lamellae morphology.[8] While this surfactants-directed assembly strategy led us to the desired particle internal structure, the photonic properties of such particles require further improvement with several challenges needing to be addressed: Firstly, improving the intensity of reflected color is desirable. Since in a one dimensional photonic crystal the reflectivity strongly depends on the number of bilayers/BCP lamellae, the overall size of the particles needs to be increased dramatically. Second, controlling the orientation of such BCP colloids would ultimately allow for switching the color on and off by using external fields. To realize such behavior, a narrow size distribution of these anisotropic colloidal building blocks is needed; since different sized ellipsoids would prevent ideal packing or hinder alignment.

To address these points, this work examines new methods for the generation of large (>2 µm) particles with narrow size distributions. We chose to focus on investigating simplified microfluidic droplet generation to control the dimension and size distribution of the droplets which yield photonic particles after solvent evaporation. We investigate two set ups for droplet generation, where the particle precursor chloroform solution/droplet phase is extruded from a needle and sheared off by the continuous flow of aqueous solution. In the first method, a coaxial tube/co-flow geometry and in the

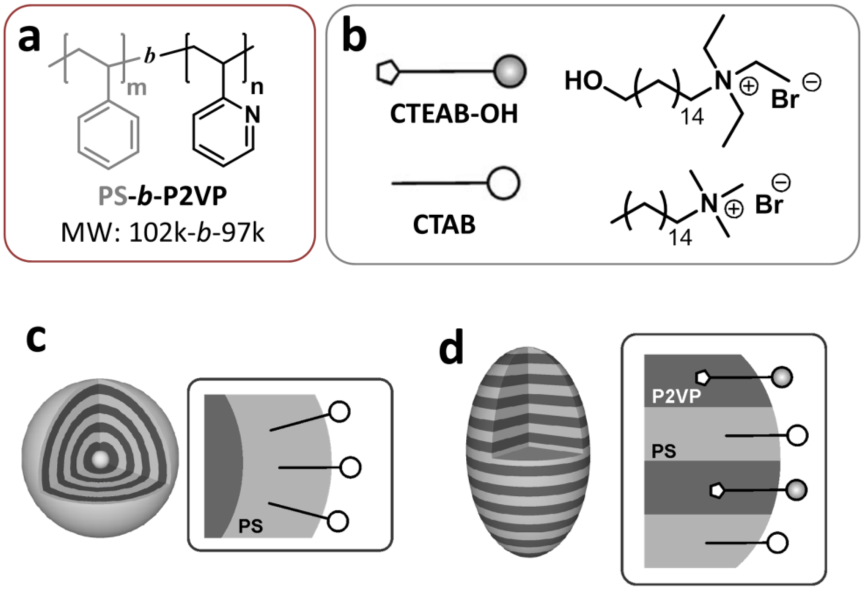

Figure 4.2. Components used for surfactant directed assembly of BCP particles and associated particle schematic. a) Poly(styrene-*b*-2-vinyl pyridine) (PS-*b*-P2VP) diblock copolymer is assembled within droplets at room temperature using two surfactants, **b)** cetyltriethylammonium bromide (CTAB) and 16-hydroxy-N,N,N-triethylhexadecan-1-ammonium bromide (CTEAB-OH). The expected particle morphology based on the selection of surfactant.: **c)** “onions” or **d)** ellipsoids with axially oriented PS-*b*-P2VP lamellar. CTEAB-OH synthesized by Daniel Klinger and Bernhard Schmidt.

second method, droplets are directly extruded into solution stirring within a round bottom flask. These methods allow access to a wide window of droplet sizes by varying parameters such as the inner diameter of the dispensing tube and flow rates of the droplet phase. Size control over these BCP assemblies is important for future work on particle alignment.

4.2 Results and Discussion

New methods to generate droplet templates for PS-b-P2VP particles were explored using a similar surfactant directed assembly strategy to Chapter 3 (Figure 4.2) but using a different emulsification strategy from ultrasonication.

4.2.1 Comparison of droplet morphology by simplified co-flow vs extrusion method

During the first stage of experiments and screening of mesofluidic emulsification methods, BCP particles were assembled in an aqueous solution with a single surfactant, 0.1 wt% CTAB. The morphology and size distribution of BCP particles produced by two droplet generator geometries were evaluated.

In the first method, inspired by co-axial flow droplet generators,[9,10] a chloroform solution containing the BCP is extruded from a needle and sheared off by a stream of continuous aqueous phase within a tube. These droplets were collected in a vial and stirred for 2 days to evaporate the chloroform. The particle morphology was investigated using scanning electron microscopy (SEM). While relatively narrow size distribution was achieved (Figure 4.3b), however, the high flow rate ratios necessary to generate droplets using this set-up yielded particles with uncontrolled morphology and rough surface

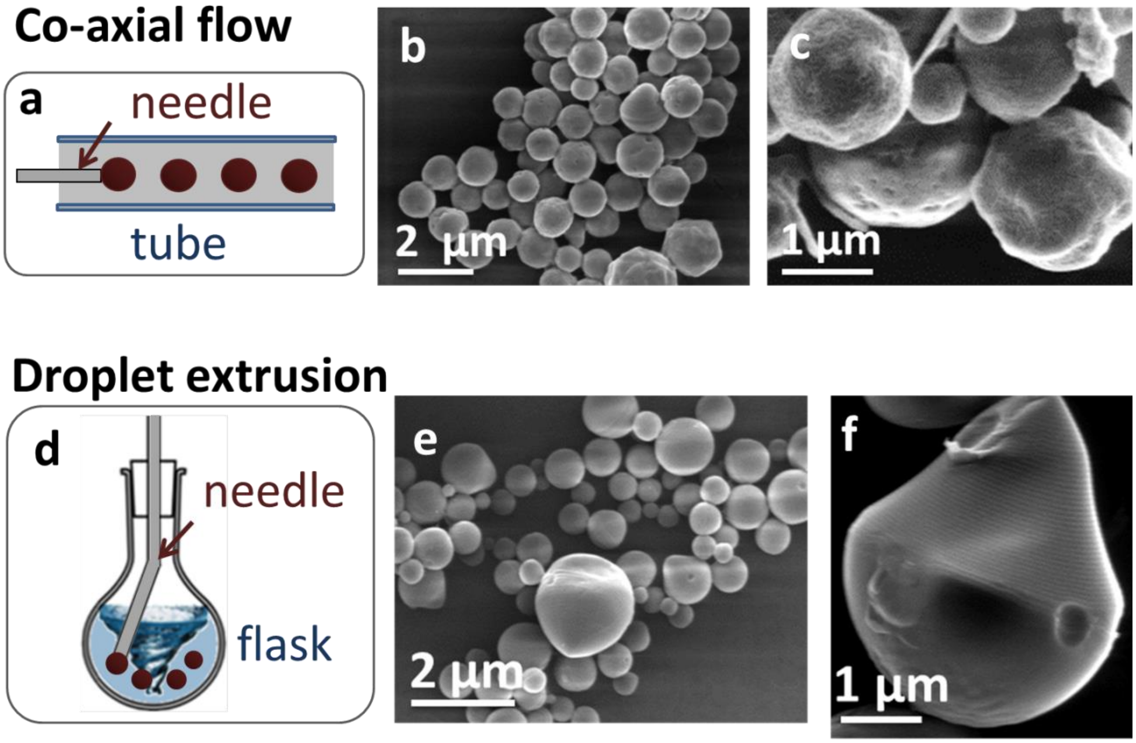

Figure 4.3. Two approaches to control droplet size. a) Schematic of coaxial droplet generation set up. **b)** SEM of PS-P2VP particles generated by the co-axial flow method in 0.1 wt% CTAB after solvent evaporation. **c)** Amorphous PS-P2VP particles **d)** Schematic of droplet extrusion set up into round bottom flask. **e)** SEM presenting overview of particles generated by droplet extrusion into a 0.1 wt% CTAB solution after solvent evaporation **f)** Large BCP particles exhibit the lamellar morphology.

texture (Figure 4.3c). Attempts to thermally or solvent anneal these colloidal particles post synthesis were unsuccessful. We hypothesize that the chloroform leaches out of the BCP droplets too quickly for self-assembly of lamella forming PS-P2VP to proceed. These results led us to pursue an alternative method which would enable slower solvent evaporation and maintain a 1:10 volume ratio of droplet to continuous phase to prevent kinetically trapped BCP phases.

In the second approach, the droplet phase is extruded from a tube using a syringe pump and sheared off by a continuous phase stirring within a round bottom vessel. The BCP droplets are stirred for 2 days to evaporate the chloroform, and the solidified particles exhibit the lamellar morphology by SEM (Figure 4.3f). While the obtained particles appear to have a broader size distribution (Figure 4.3e) than the former co-flow approach, the average droplet size can still be controlled in this set up through parameters such as tube diameter, flow rate of droplet phase, and stirring speed. Similar extrusion set ups have been use to prepare alginate beads by polymer extrusion into a crosslinking solution but without stirring.[11]

4.2.2 Effect of extrusion rate and dispensing tube diameter on particle size

The average droplet size was expected to increase with the inner diameter of the tube dispensing the droplet phase. To test this, the droplet phase was dispensed from tubes with the following inner diameter: 0.25 mm, 0.5 mm and 0.76 mm, at a constant flow rate of 10 μL/min using a syringe pump. After evaporation of the chloroform phase, the particles were analyzed by electron microscopy (Figure 4.3). Comparison of the histograms indicates that a wider dispensing tube increases the average particle size (Figure 4.4). However, when the dispensing flow rate was increased to 50 μL/min, this reduced the influence of the tube diameter on the outcome of average particle size. The asymmetric acorn shape of some particles, observed independent of flow rate, tube

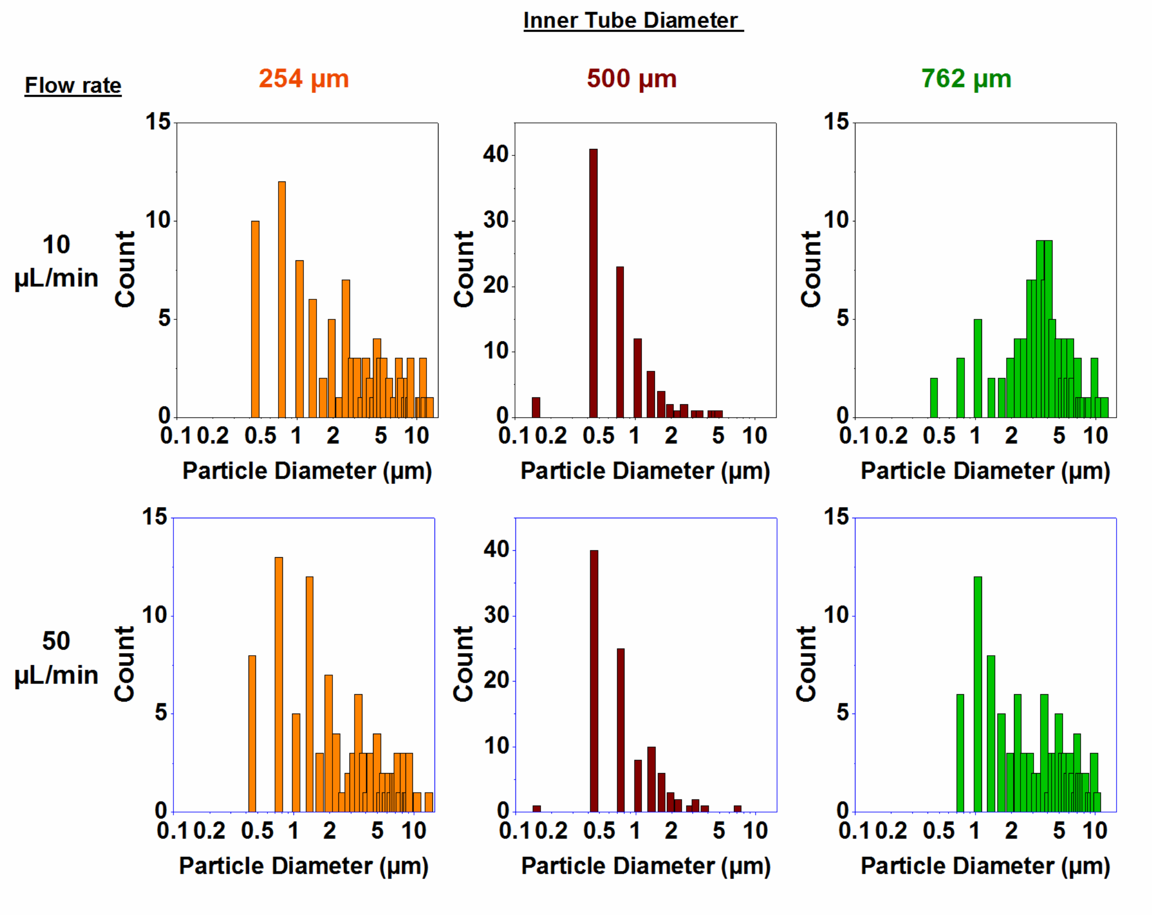

Figure 4.4. Particle size distributions for varied dispensing tube dimensions and different extrusion rates. Three different tube sizes were tested keeping the final volume ratio of droplet phase to continuous phase constant for two droplet extrusion rates at 10 μL/min and 50 μL/min. Larger particles were observed for wider tubing diameter. Each histogram was generated from measurements of 200 particles.

diameter and dispensing orientation, has also been observed for polymeric particles produced by other extrusion set ups.[11] Having demonstrated the ability of this mesofluidic

droplet generation method to tune droplet size using several different parameters, this method was applied to generate large ellipsoidal BCP particles (>2 μm). Such asymmetric particles would be of interest for colloidal Bragg reflectors.

In order to assemble large BCP ellipsoids at room temperature, a new surfactant with a triethylamine polar headgroup (CTEAB-OH) (Figure 4.1, conditions in Experimental) was synthesized to associate with the P2VP domain. This surfactant exhibited better solubility in water than our previously reported mixed surfactant system[8] that required a temperature of 30 ^{o}C to suppress crystallization of CTAB-OH in water. Following the previously described extrusion set up, droplets of BCP solution were dispensed from a 500 μm tube into a round bottom flask containing 20 mL of 0.1 wt% surfactant concentration with a 4:6 weight ratio of CTAB:CTEAB-OH. After solvent evaporation, ellipsoids with long axis measurements as large as 16 μm were observed (Figure 4.4). More importantly, the lamellar morphology is clearly observed on the particle surface as shown by high magnification SEM (Figure 4.5). For comparison, BCP particles prepared by ultrasonication emulsion of PS-P2VP in equivalent surfactant mixtures are also shown in Figure 4.4. Small particles are also observed in the batch from droplet extrusion (Figure 4.4), likely due to the break of of satellite droplets during stir-

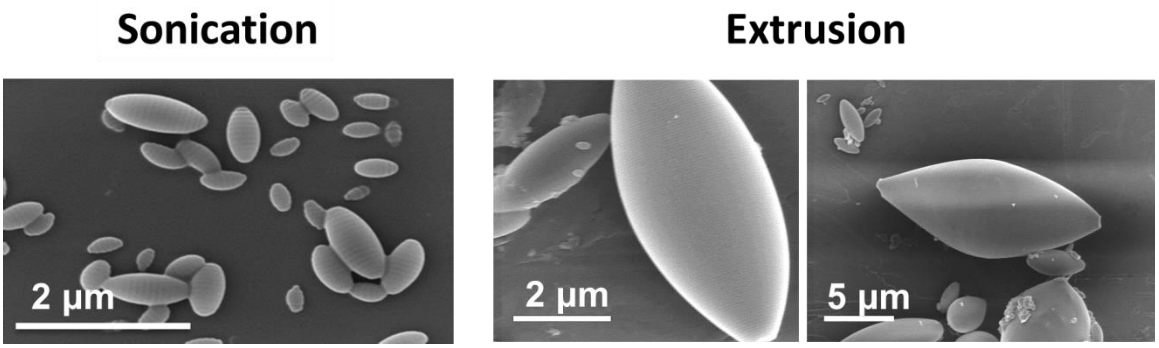

Figure 4.5. SEM of particles from sonication versus extrusion method. Both methods emulfisied PS-P2VP chloroform droplets in 4:6 w/w CTAB:CTEAB, 0.1 wt% surfactant concentration.

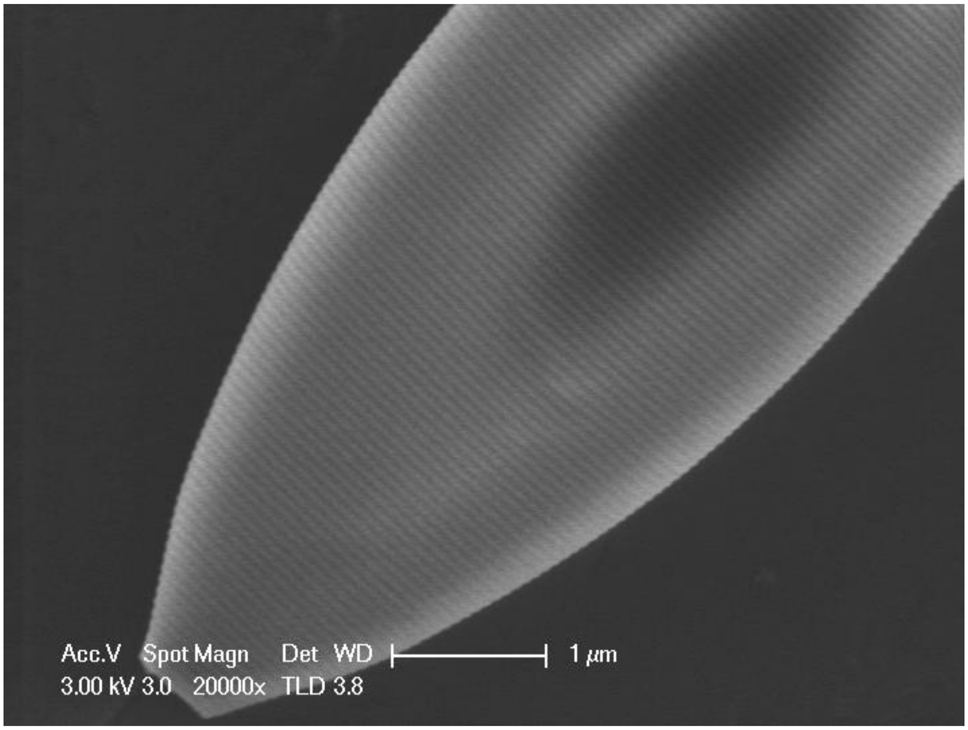

Figure 4.6. Alternating PS-P2VP domains visible by SEM. Axial orientation of lamellae maintained for the large ellipsoids produced by droplet extrusion method. PS domains are dark while the P2VP domains appear light grey due to an iodine stain.

-ring for solvent evaporation. Purification methods post-assembly of the BCP particles may address this concern.

4.3 Summary

A new method to generate micron scale ellipsoidal nanoparticles using surfactant directed assembly of poly(styrene)-b-poly(2-vinyl pyridine) was presented. The amorphous particles from first coaxial flow set-up, reveals two critical factors for BCP self-assembly in our system, 1) ratio of droplet to continuous phase 2) slow solvent evaporation. In the second approach involving droplet extrusion into a stirring continuous phase, we demonstrated access to a larger window of particle sizes compared to sonicated emulsions. This work is an important stepping stone toward the development of stimuli responsive photonic colloids.

Our collaborators in the Soh Lab are currently exploring strategies to purify large ellipsoidal BCP particles from polydisperse samples based on dielectrophoretic sorting of particles combined with high speed microscopy. Automated image analysis within an integrated microfluidic device enables their system to discriminate particles by size and shape.

4.4 Experimental

4.4.1 Materials

Cetyltrimethylammoniumbromide (CTAB, Sigma Aldrich, ≥ 99%), triethylamine (NEt_3, Acros, 99%), Poly(styrene-block-2-vinyl pyridine) (PS-b-P2VP) (MW: 102k-97k, Polymer Source Inc.), and 16-bromo-1-hexadecanol, (Astatech Inc, 95%) were used as received. Chloroform and methanol were purchased from Fisher Scientific. Tygon tubing (outer diameter/OD: 1.78 mm, inner diameter/ID: 1 mm) was purchased from Cole-Parmer. FEP tubing with the following specifications were purchased from Idex Health and Science (OD: 1.59 mm with ID: 0.254, 0.508, or 0.762 mm). Ultrahigh purity deionized water (18.2MΩ·cm) was obtained from buffer grade Mili-Q Advantage A10 water purification system by MilliPore. Digital syringe pumps were manufactured by New Era.

4.4.2 Particle synthesis

The droplet phase consisted of 0.1 wt% polymer solution prepared by dissolving poly(styrene)-b-poly(2-vinyl pyridine) (MW: 102k-97k) in chloroform. The continuous phase was composed of 0.1 wt% surfactant in MiliQ deionized water, where the surfactant was either CTAB or a combination of CTAB and CTEAB-OH. CTEAB-OH (16-hydroxy-N,N,N-triethylhexadecan-1-ammonium bromide) was synthesized according to a literature procedure.

Sonication method: 1 mL of droplet phase and 10 mL of surfactant solution are combined in a 20 mL vial and capped. The mixture is vortexed for 30s, emulsified in an ultrasound bath for 2 min, and the chloroform evaporated by stirring open vials containing the emulsions for 2 days.

Co-axial flow method: In the co-axial flow set up, a needle to dispense the droplet phase was inserted into a tube, containing the continuous phase. The flow rates used to generate droplets were $Q_{continuous}/Q_{droplet}$ at 10/0.05 mL min $^{-1}$ The emulsion was collected into 20 mL vials and the chloroform evaporated by stirring open vials containing the emulsions for 2 days.

Droplet extrusion into round bottom method: 2 mL of droplet phase is extruded from a tube using a syringe pump ($Q_{droplet}$ = 10 or 50 μL min^{-1}) and sheared off by a stirring aqueous continuous phase (20 mL, 0.1 wt% surfactant) within a round bottom vessel containing a magnetic stir bar. The chloroform was evaporated by stirring open vessels containing the emulsions for 2 days.

4.4.3 Particle characterization

The particles were visualized by field-emission scanning electron microscopy, using an FEI XL30 Sirion microscope operating with an accelerating voltage of 3 kV. Samples were prepared by drop casting dilute particle solutions on silicon wafers and sputter coated with gold/palladium. For each histogram, the diameters of two hundred particles were measured via ImageJ.

4.5 References

1. Tao, A. R.; DeMartini, D. G.; Izumi, M.; Sweeney, A. M.; Holt, A. L.; Morse, D. E. *Biomaterials* **2010**, *31*, 793–801.
2. Ball, P. *Sci. Am.* **2012**, *306*, 74–79.
3. Crookes, W. J.; Ding, L.; Huang, Q. L.; Kimbell, J.; R. Horwitz, J.; McFall-Ngai, M. J. *Science.* **2004**, *303*, 235–238.
4. Yu, C.; Li, Y.; Zhang, X.; Huang, X.; Malyarchuk, V.; Wang, S.; Shi, Y.; Gao, L.; Su, Y.; Zhang, Y.; Xu, H.; Hanlon, R. T.; Huang, Y.; Rogers, J. A. *Proc. Natl. Acad. Sci.* **2014**, *111*, 12998–13003.
5. Phan, L.; Walkup, W. G.; Ordinario, D. D.; Karshalev, E.; Jocson, J.-M.; Burke, A. M.; Gorodetsky, A. A. *Adv. Mater.* **2013**, *25*, 5621–5625.
6. Walish, J. J.; Kang, Y.; Mickiewicz, R. A.; Thomas, E. L. *Adv. Mater.* **2009**, *21*, 3078–3081.
7. Park, J.-G.; Kim, S.-H.; Magkiriadou, S.; Choi, T. M.; Kim, Y.-S.; Manoharan, V. N. *Angew. Chem. Int. Ed. Engl.* **2014**, *53*, 2899–2903.
8. Klinger, D.; Wang, C. X.; Connal, L. A.; Audus, D. J.; Jang, S. G.; Kraemer, S.; Killops, K. L.; Fredrickson, G. H.; Kramer, E. J.; Hawker, C. J. *Angew. Chem. Int. Ed. Engl.* **2014**, *53*, 7018–7022.
9. Quevedo, E.; Steinbacher, J.; Mcquade, D. T. *J. Am. Chem. Soc.* **2005**, 10498–10499.
10. Abate, A. R.; Seiffert, S.; Utada, A. S.; Shum, A.; Shah, R.; Thiele, J.; Duncanson, W. J.; Lee, M. H.; Akartuna, I.; Lee, D.; Rotem, A.; Weitz, D. A. 1–21.
11. Hu, Y.; Wang, Q.; Wang, J.; Zhu, J.; Wang, H.; Yang, Y. *Biomicrofluidics* **2012**, *6*, 26502–265029.

5 Microgel Particles with Functional Payloads: Coacervation of PEG-Based Triblocks via Microfluidics[‡]

5.1 Introduction

Biomedical applications such as therapeutic delivery vehicles[1,2] and scaffolds for regenerative medicine[3] increasingly require well-defined and tunable polymeric carriers. Microgels are highly attractive candidates for these roles due to their unique combination of a hydrophilic internal network that can mimic properties of tissue,[4] with the structural features of colloidal particles.[5–9]

The development of microgels to serve as biocompatible scaffolds[3,10] or carriers[5] requires control both over a) microgel size and particle size distribution as well as b) microgel network composition and functionality. However, traditional methods to synthesize microgels such as emulsion polymerization[11] and phase separation[12] do not meet the former criteria and often yield batches with broad carrier size distribution that may lead to undesired variability in the cargo release profile. To address this issue, droplet microfluidics has emerged as a powerful tool for precise formation of microgel particles with well-defined sizes and narrow size distribution.[13] The droplet formation can be combined with a variety of covalent or physical network formation mechanisms to tailor the chemical composition of

---

[‡] Reproduced with permission from ACS Applied Materials and Interfaces, submitted for publication. **Wang, C. X.;** Utech,S.; Gopez, J. D.; Mabesoone, M. F. J.; Hawker, C. J.; Klinger, D. “Non-Covalent Microgel Particles Containing Functional Payloads: Coacervation of PEG-Based Triblocks via Microfluidics.” Unpublished work copyright 2016 American Chemical Society.

microgels.[14] For instance, degradable microgels exhibit triggered cargo release in response to diverse environmental stimuli[5] based on network composition.

With regard to the microgel composition, achieving the desired chemical functionality of the networks poses a significant challenge. To enable the encapsulation of biologically relevant but fragile payloads, traditional covalent network formation methods that are well-established in emulsion-based approaches are often too harsh.[15] To avoid harmful reactions such as radical polymerizations or glutaraldehyde crosslinking,[16,17] the development of new mild and efficient methods for hydrogel formation is of significant utility.

Physical gelation provides a mild route to encapsulate fragile or living cargo since no toxic initiators or crosslinkers are required.[18] Biocompatible microgels for regenerative medicine and cell cultures are often composed of natural polymers such as alginate, chitosan or hyaluronic acid, physically associated by multivalent ions[10,19] or by homopolymers.[20] While this approach is biocompatible, the combination of compositional variation among the harvested batches[21] with the random distribution of ionic crosslinks for these systems[22] presents an obstacle to systematically tuning the network mesh size. Mesh size is a key factor in scaffold mechanics and diffusion of encapsulated cargo. A physical crosslinking platform to produce microgels with controlled composition from precise building blocks would bridge this gap. Synthetic polymers in particular would allow a degree of control that is not easily achievable using natural building blocks.

In focusing on a mild and efficient crosslinking strategy, an ideal microgel encapsulation platform would combine the narrow particle size distribution, accessible

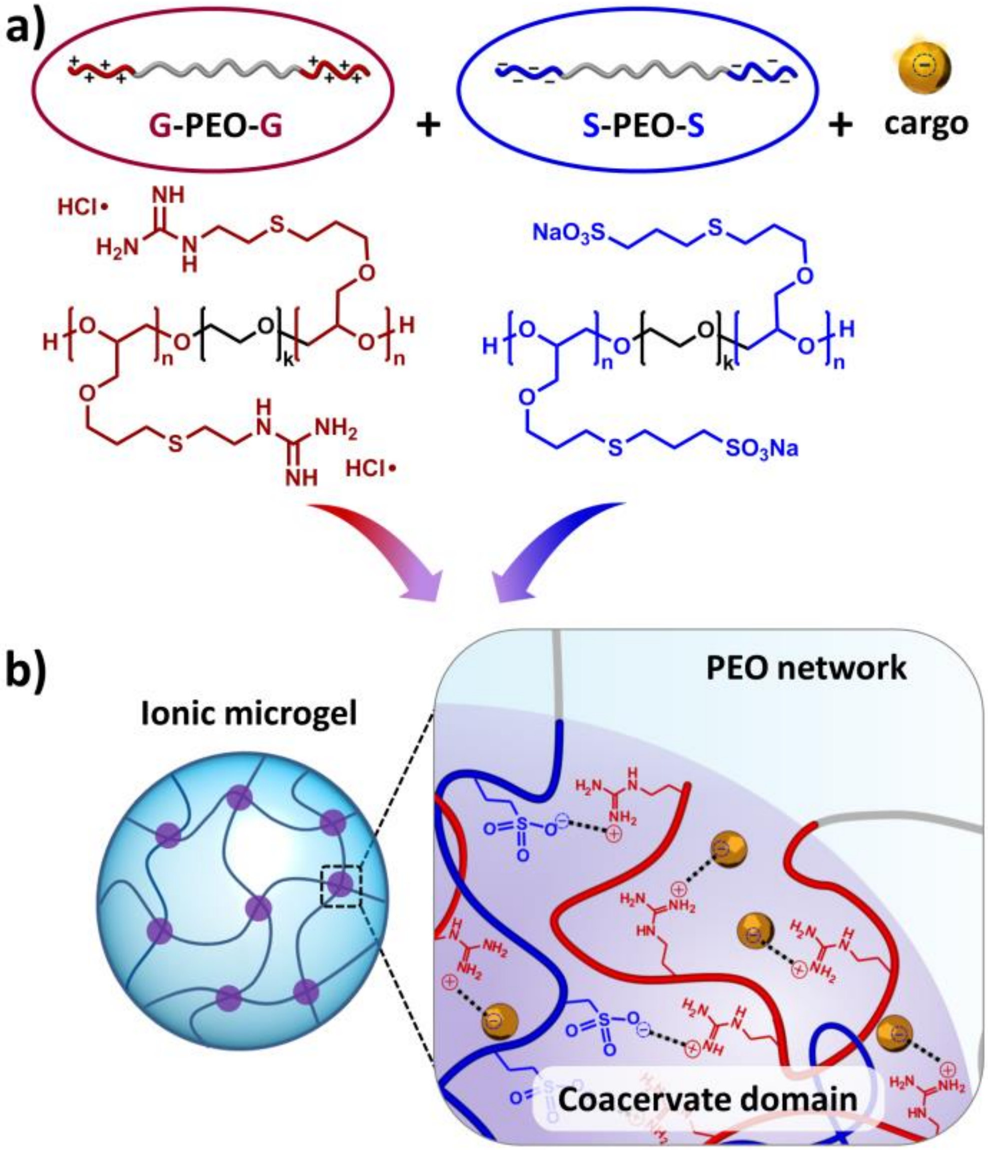

Figure 5.1. Schematic of coacervate based microgels from ABA triblock copolymers. a) Schematic of the components of the microgels: PEO-based triblock copolymers with guanidinium (cationic, G-PEO-G) or sulfonate (anionic, A-PEO-A) functionalized end-blocks and cargo (anionic dye, e.g. fluorescein carboxylate). b) Graphic depicts the electrostatic interaction between the oppositely charged end blocks and anionic cargo.

through microfluidics, with the structural control inherent in block copolymers.

Nature provides instructive examples of aqueous materials assembly for tunable hydrogels. Marine organisms, for example produce strong crosslinked materials by mixing oppositely charged polyelectrolytes, known as complex coacervate formation.[23–26] Recent work demonstrates that transferring this coacervate concept to synthetic materials allows for modular assembly of hydrogel networks.[27] One example of this strategy involves cationic guanidinium (G) end-blocks of G-PEO-G polymers forming coacervate domains upon interaction with the anionic sulfonate (S) end-blocks of S-PEO-S polymers. These coacervate domains serve as physical crosslinks bridged by the hydrophilic PEO mid-blocks.[27]. Moreover, the use of synthetic polymers provides a degree of control that is hard to realize using natural building blocks. The resulting networks exhibit well-defined internal structures that are tunable *via* the block copolymer architecture. Translating this efficient non-covalent crosslinking strategy from the bulk to colloidal particles through microfluidics represents a promising approach towards well-defined microgels. Additionally, the coacervate domains may serve as reservoirs for the encapsulation of charged water-soluble payloads. As shown in Figure 1, this encapsulation strategy is based on electrostatic interactions between dye and charged polymer end-blocks. This strategy allows for loading and release of the payload by varying the ionic strength of the surrounding media and the number and nature of the ionic groups present in both the polymer blocks and small molecules.

5.2 Results and Discussion

5.2.1 Ionic microgels by microfluidic flow focusing

Following the successful preparation of bulk hydrogels from cationic and anionic triblock copolymers, a number of key steps were required for the development of the corresponding microgel particles. Of particular interest was the development of an efficient microfluidic setup for preparation of stable particles with tunable diameters and narrow size distribution as well as the ability to transfer these particles into aqueous media while retaining their structural integrity.

In the first step, a reactive triblock precursor polymer with poly (allyl glycidyl ether) (PAGE) end-blocks was prepared by living anionic polymerization from a commercially available PEO starting block.[27] This affords the desired PAGE-*b*-PEO-*b*-PAGE triblock copolymer with MW of 4k-10k-4k and PDI = 1.1. Thiol-ene click chemistry could then be used to functionalize the triblock AGE units with ionic guanidium (G) or sulfonate (S) groups to yield G-PEO-G and S-PEO-S microgel precursors, respectively (see SI for synthetic details).

In the next step, these ionic building blocks need to be mixed in dispersed water droplets to form microgels particles. As shown in Figure 2, this was achieved by using a custom-made flow-focusing PDMS microfluidic device.[10] A crucial feature of this design is the use of two separate reservoirs for the different triblock copolymer solutions. This is similar to marine mussels which have separate chambers for storage of the anionic and cationic peptides prior to co-extrusion and formation of adhesive plaques.[23,28] Preceding droplet formation, solutions of the triblock copolymer are flowed into a central channel where a water stream in the middle prevents premature gelation and potential clogging of the aqueous channel. At the junction, monodisperse droplets are formed within a continuous oil phase (Novec 7500) containing 1 wt % of biocompatible surfactants[29] and within each droplet, the charged block copolyelectrolytes are then able to mix[30] and undergo coacervation to form an ionically crosslinked network and the desired microgel particles. Additionally, inlet filters and fluid resistors were incorporated within the device to prevent entry of debris and dampen flow fluctuations respectively.

Reproducible microgel formation required optimization of the polymer feed concentration and associated flow rates. Insufficient concentration of polymer (below gelation point) prevents formation of spherical particles or leads to unstable gels. In contrast, excess polymer concentration gives rise to premature gelation and clogging of the device. Therefore, the polymer feed was varied to determine the concentration range for obtaining uniform and spherical microgels with a homogeneous internal network. To illustrate, experiments were carried out with 5 wt %, 10 wt % and 20 wt % polymer solutions. In all experiments charge balance was ensured through equimolar ratios of guanidium and sulfonate groups.

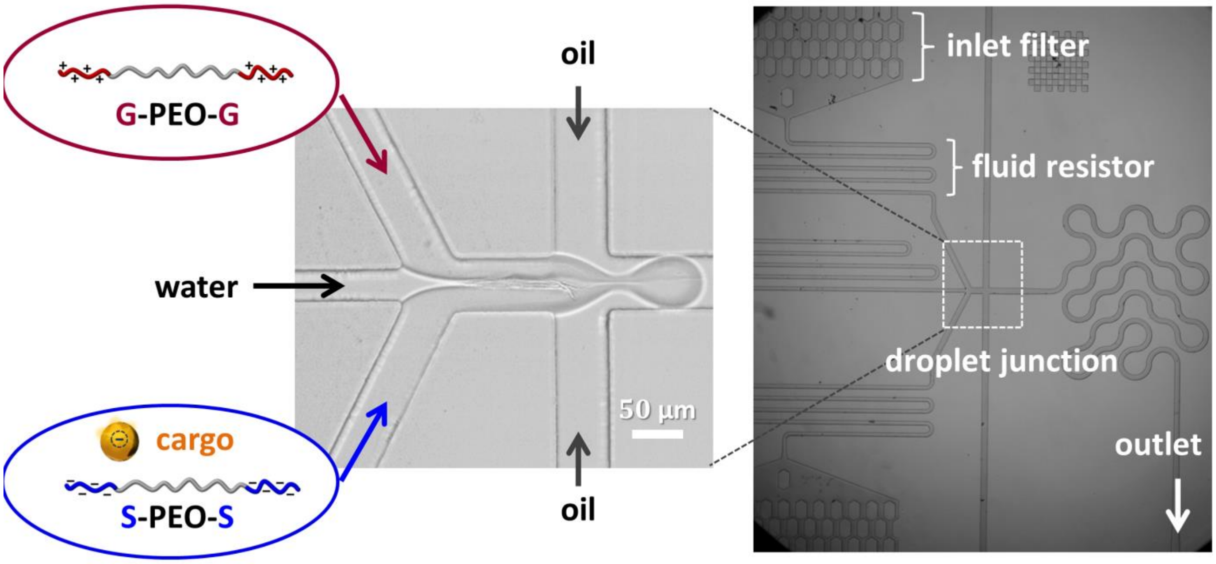

Figure 5.2. Optical image of droplet production by microfluidic flow focusing. Solutions of PEO-based triblock copolymers with cationic (guanidinium, G) or anionic (sulfonate, S) end blocks are separated by a water stream until the droplet junction, in which the continuous oil phase flow focuses the aqueous phase into droplets. A curved outlet was designed to facilitate mixing within the droplet for gelation. Inlet filters and fluid resistors upstream of the droplet junction prevent entry of debris and dampen flow fluctuations respectively.

5.2.2 Concentration study of polymer feed

The morphology of the droplets formed was analyzed by optical microscopy (Figure 3). From these results it becomes obvious that 5 wt % polymer feed leads to non-uniform

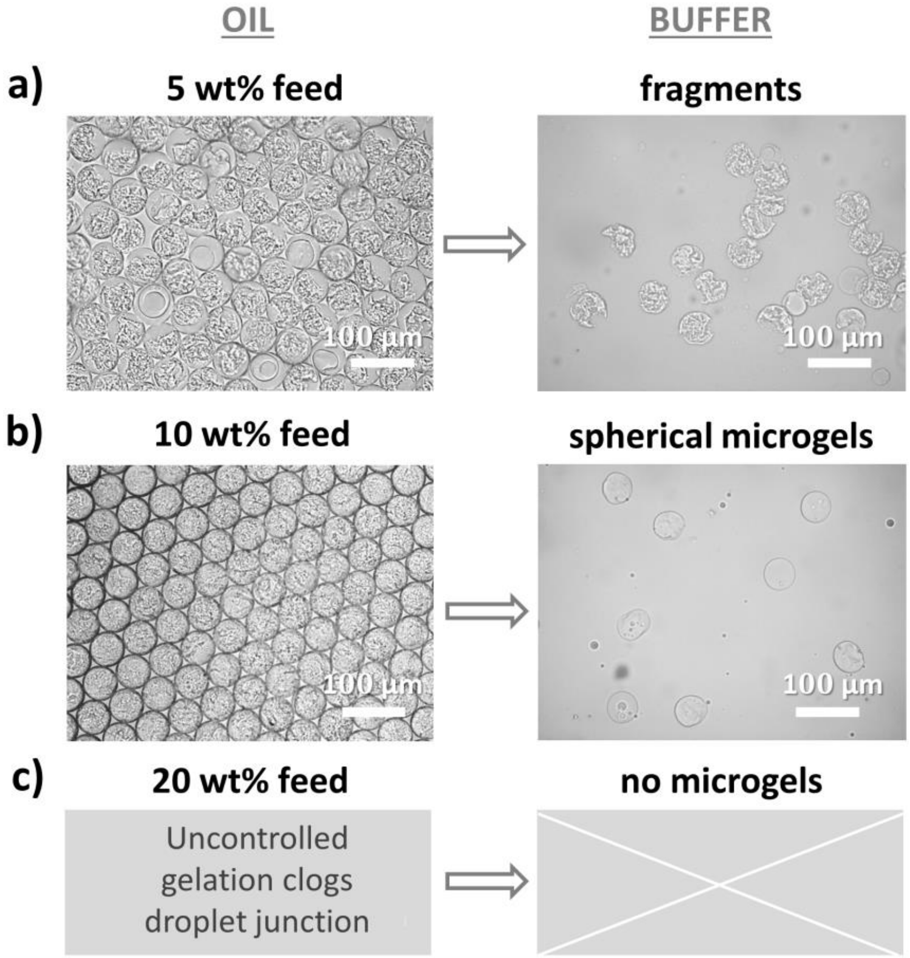

Figure 5.3. Determination of optimal polymer feed concentration for microgel production. Optical micrographs of microgels from 5 wt %, 10 wt % and 20 wt % polymer feed: a) Non-uniform gel distribution was observed within droplets from 5 wt % polymer feed. After transfering to phosphate buffered saline (PBS), non-spherical gel fragments resulted. b) Microgels from 10 wt % polymer feed yielded droplets with a homogeneous gel distribution. These were stable upon transfer to buffer. c) Macroscopic gelation in the droplet junction occurred at 20 wt % polymer feed prevented controlled droplet formation. Scale bars are 100 µm.

distribution of gels within the droplets. It is assumed that in this case the polymer concentration was too low to form homogeneous hydrogels in the confined volumes. As a result of dilution with the middle water stream, the effective concentration of polymers in the droplets is ~4 wt % (based on the flow rate ratio of the water to polymer streams). These conditions likely result in phase separation between hydrogel fragments and excess water in each droplet. In contrast, microgels from the 10 wt % polymer feed yielded a homogeneous gel distribution throughout the droplets (effective polymer content is ~8 wt %). Macroscopic gelation in the droplet junction occurred at polymer feed concentrations of 20 wt % and above. Additional experiments showed stable formation in the 7-15 wt% range with 10 wt % leading to reproducible and controlled droplet formation. For this range of concentrations, optimized syringe flow rates are 60/30/600 μL hr $^{-1}$ for Q_{phase}: $Q_{polymer}/Q_{water}/Q_{continuous}$.

The utility of these hydrogel particles for applications such as biomedical scaffolds or delivery vehicles is crucially dependent on their structural stability in aqueous media. Therefore, the microgels were transferred from the continuous oil phase to phosphate buffered saline (PBS). Following a literature procedure, a fluorinated alcohol surfactant (heptadecafluoro-1-decanol) was added to stabilize the microgels in aqueous solution before transfer to PBS (10mM, pH=7.4).[10] Significantly, when the 10 wt % polymer droplets were transferred, it was observed that the time between microgel formation and transfer plays a major role in determining the resulting structural stability in water. When particles were transferred immediately after their preparation, limited (5-10%) fragmentation of the particles was observed (Figure 3). In direct contrast, when the microgels were kept in the oil phase for 12 hours or greater, full retention of particle diameter and shape was observed with no morphological changes being observed on transference or with prolonged storage (Figure S2). This suggests that for the 10 wt % gels, full formation of the ionic crosslinks and network structure requires an extended annealing time to complete the assembly of the dynamic coacervate domains. This requirement for full formation of coacervate domains and ionic crosslinks also occurs for the non-uniform 5 wt % microgels. Complete fragmentation of the particles are observed upon immediate transfer with ca. 50% remaining intact after aging for 12 hours. These observations highlight the dynamic nature of the coacervate-driven networks and the importance of a homogeneous hydrogel morphology for structural stability.

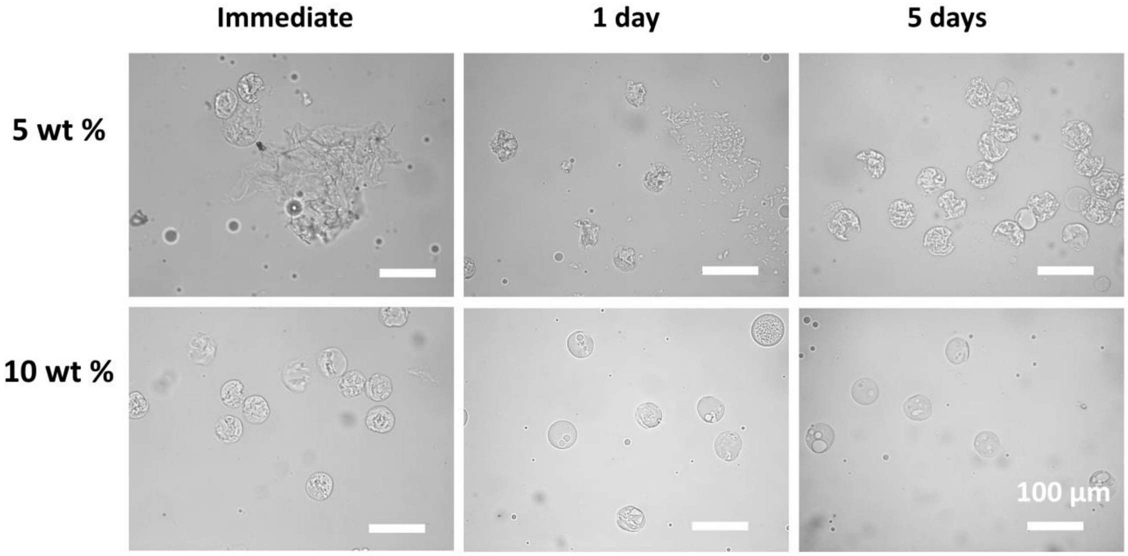

Figure 5.4. Time dependent transfer of microgels to buffer solution. Optical micrographs of microgels transferred immediately from the oil phase to buffered solution, or kept in the oil phase 1 day or 5 days before transfer. Scale bars are 100 µm.

5.2.3 Incorporating fluorescein carboxylate as a model payload into the microgels

Having demonstrated the ability to prepare robust microgel particles, our attention was drawn to the potential of the coacervate domains to serve as reservoirs for functional small molecules. Taking advantage of the dynamic nature of the coacervate domains, it is proposed that the encapsulation of charged payloads can occur through electrostatic interactions between the ionic small molecules and the charged end-blocks of the polymers. In testing this proposed strategy, fluorescein carboxylate was initially selected as an anionic model compound that would interact with the cationic guanidinium groups present in the coacervate domains (see Figure 1). Loading was simply achieved *during* microgel formation by adding the anionic cargo to the feed solution of the negatively charged S-PEO-S polymer. The structural stability of the hydrogel networks was preserved by maintaining the charge balance between anionic and cationic groups. For example, microgels could be loaded with 10 mol % of fluorescein by feeding a 10 wt % aqueous solution of the guanidinium triblock (242 mM guanidinium groups, 1 eq.) with a mixed aqueous solution of 9.5 wt % sulfonate triblock (218 mM sulfonate groups, 0.9 eq.) and 0.9 wt % fluorescein (24 mM carboxylate groups, 0.1 eq.) in the microfluidic device described above. This results in robust loaded microgel particles with stability that is comparable to the corresponding non-loaded particles. To determine the encapsulation efficiency and release characteristics of the fluorescein labelled materials, the microgels were subjected to repeated rinsing steps to remove unbound dye. Then the total amount of encapsulated dye was determined by degradation of the particles upon dissolution in aqueous pH 12 solution. This results in disruption of the coacervate domains by breaking the ionic/electrostatic crosslinks, releasing the bound fluorescein which could then be quantified by UV-Vis spectroscopy. From these studies the encapsulation efficiency was calculated to be ~50%.

Incorporating charged small molecule cargos into the coacervate domains through electrostatic interactions represents a unique loading strategy for microgel particles and opens up a range of opportunities for controlling the release profile. Salt has been previously observed to screen charge interactions between cargo and carrier.[15] To test the effect of ionic strength on the cargo release profile, microgels (66 μm diameter) were incubated at 37 °C, (to simulate body temperature) in two types of media: deionized water and PBS (pH 7.4, 10 mM). The percent cumulative release of fluorescein dye was calculated at specific time points by normalizing the amount of dye released into the supernatant with the amount of dye bound within the microgel at t=0. Different release profiles were observed depending on the ionic strength of the solvent (

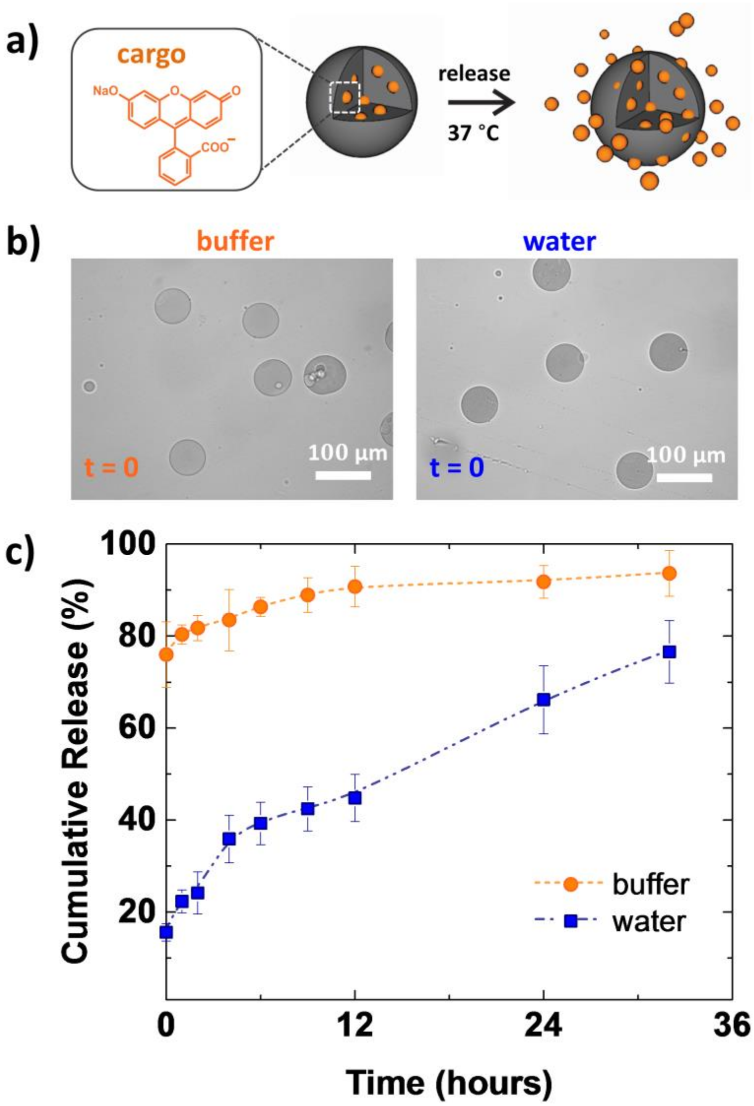

Figure 5.5).

Release of fluorescein from the microgels was gradual in water, 80% of the dye was released over 48 h. In comparison, release was significantly accelerated in PBS, which had released over 80% of the dye within 2 h. This behavior is consistent with the observed weakening of coacervate interactions with buffer solutions that screens the electrostatic interactions between anionic chains and cationic chains. As a result, the binding between the cargo and the coacervate domains also decreases, thus leading to accelerated release.[31] Since these findings indicate that weakening the interaction between the payload and carrier can accelerate the release profile, a stronger interaction between the carrier and cargo, such as a larger pKa difference between the charged groups, may decelerate release of the cargo.

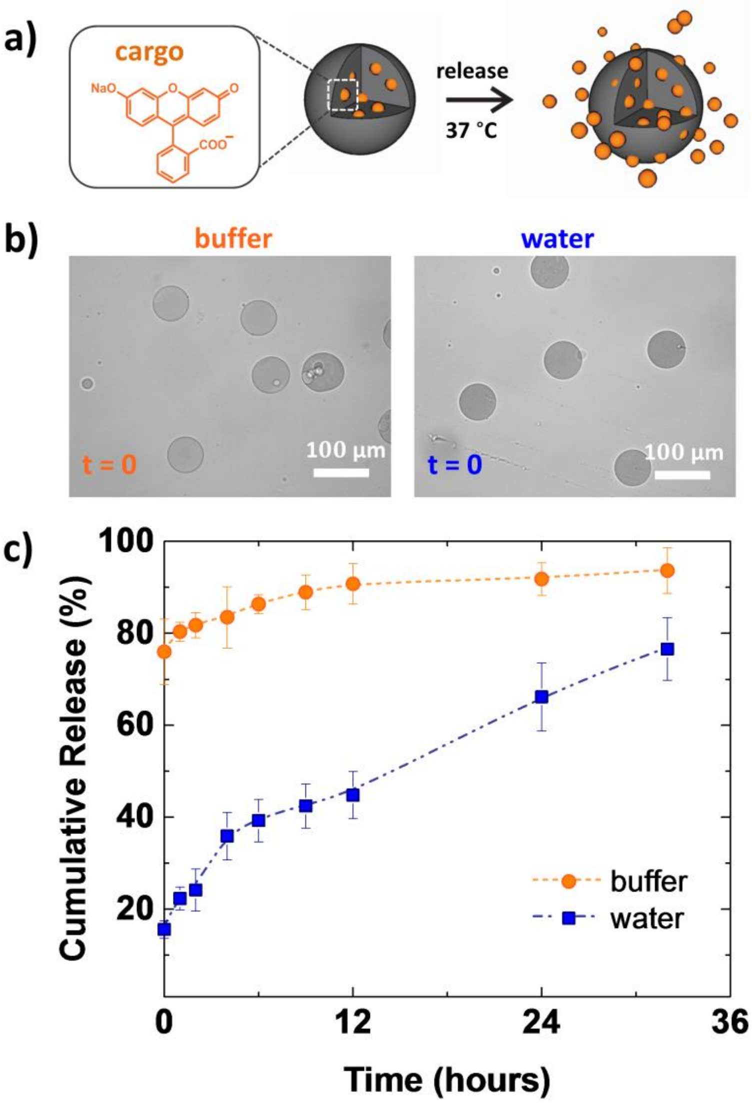

Figure 5.5. Release of fluorescein payload from microgels in media of different ionic strength. a) Schematic of dye loaded microgel and cargo release. b) Optical images of microgels in PBS buffer (pH 7.4, 10 mM) and water. c) The release profiles of fluorescein loaded microgels in PBS and deionized water were compared. Scale bars are 100 μm. The percent release was calculated from UV-vis absorbance measurements, tracking the absorbance at 460 nm. Error bars represent the standard error based on n=4 samples.

5.2.4 Effect of payload affinity for carrier on microgel release profile

Having demonstrated that the electrostatic interactions between the fluorescein payload and the coacervate domains affected the payload release rate, we hypothesized that number and nature of the ionic groups in the small molecule payload would also influence the microgel release profile.

To test this assumption, microgels were prepared using the same device and triblock copolymers as described above but with a similar ~4.5 mol % of two different small molecule dyes: the sulfonate-functionalized derivative 4-(2-Hydroxy-1-naphthylazo) benzenesulfonate (orange II) and 8-hydroxypyrene-1,3,6 trisulfonate (pyranine). Compared to fluorescein carboxylate, orange II has a similar molecular size, however the presence of a sulfonate group instead of a carboxylate group results in a much lower pKa for orange II. This is expected to increase the strength of the electrostatic interaction with the guanidinium domains, thereby delaying the release.[32] In a related fashion, pyranine contains three sulfonate functional groups compared to the single sulfonate/carboxylate group for fluorescein and orange II which would be expected to further increase the affinity of the small molecule dye for the microgel network.

Comparative release experiments were then conducted with microgels of similar dimensions (40 μm) and containing similar concentrations of the small molecule dye (Figure 4a). All release experiments were conducted at 37 °C in PBS (pH 7.4, 10 mM) over 3 days and the percent cumulative release was calculated at specific time points by normalizing the mass of released dye in the supernatant to the mass of incorporated dye at t=0. Significantly, different release profiles were observed for each dye with the release rate being directly related to the structure of the small molecule. For orange II, the rate of release from the microgels was observed to be significantly slower than the release of fluorescein carboxylate: 75% release of the cargo occurred over 3 days. This is in direct contrast to fluorescein-based microgels which released 78% of the dye within the first hour (Figure 4b). As expected, the increase in the number of sulfonate groups for pyranine cargo leads to slower release kinetics. In this case, a significant decrease is observed when compared to orange II with only 60% of the dye being released over 3 days. These findings are of particular interest as they clearly illustrate the tunability of the release profiles for small molecules and the close correlation between molecular structure, overall ionic character, and cumulative release.

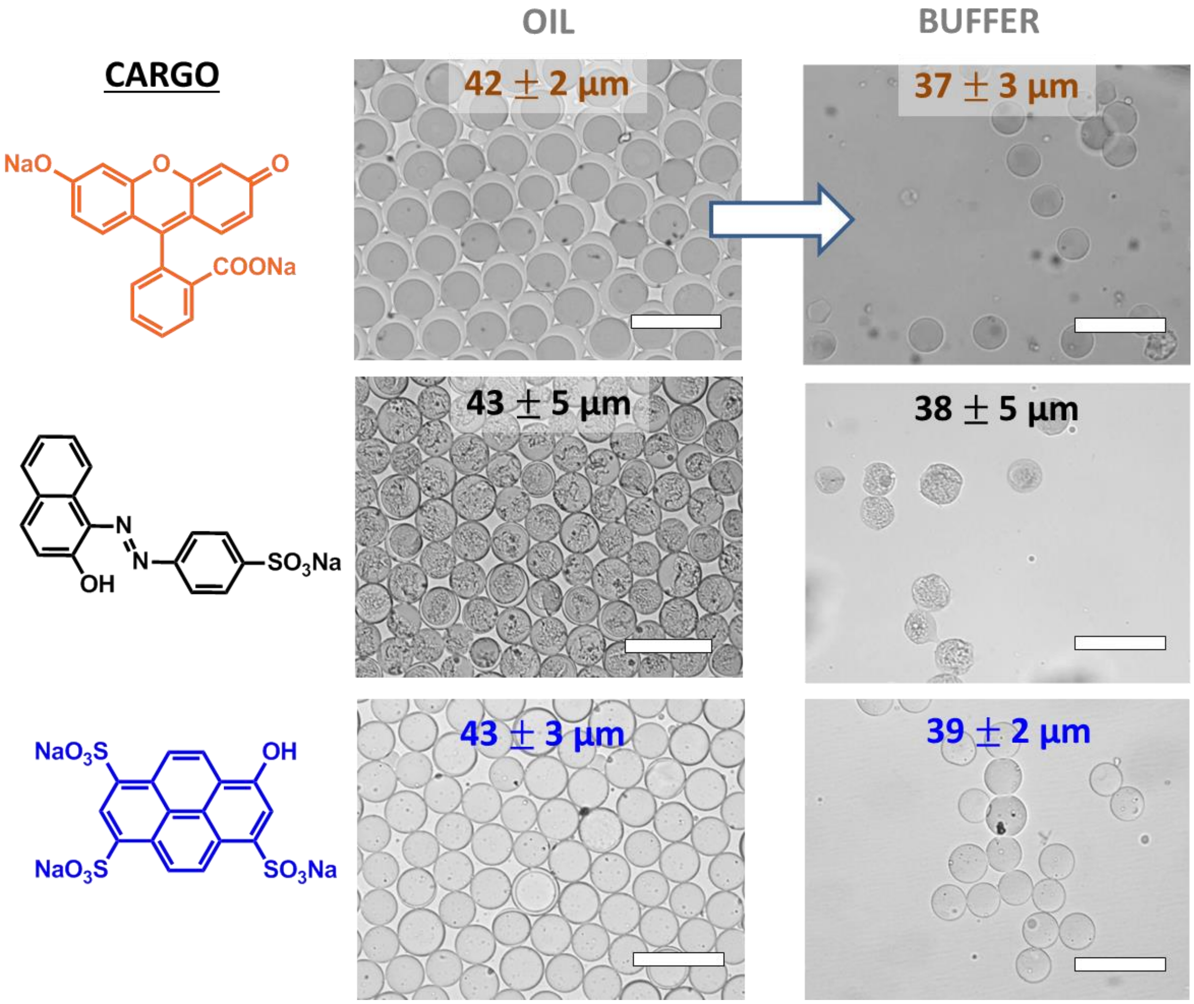

Figure 5.6. Optical micrographs and average diameter of microgels prepared from 10 mol% of anionic dye feed and after transfer to buffer solution. Microgels contain one of the following dyes: fluorescein carboxylate, 4-(2-Hydroxy-1-naphthylazo) benzenesulfonate (orange II), and 8-hydroxypyrene-1,3,6 trisulfonate (pyranine). Reported particle diameters are the average from 200 particle measurements. Scale bars are 100 µm.

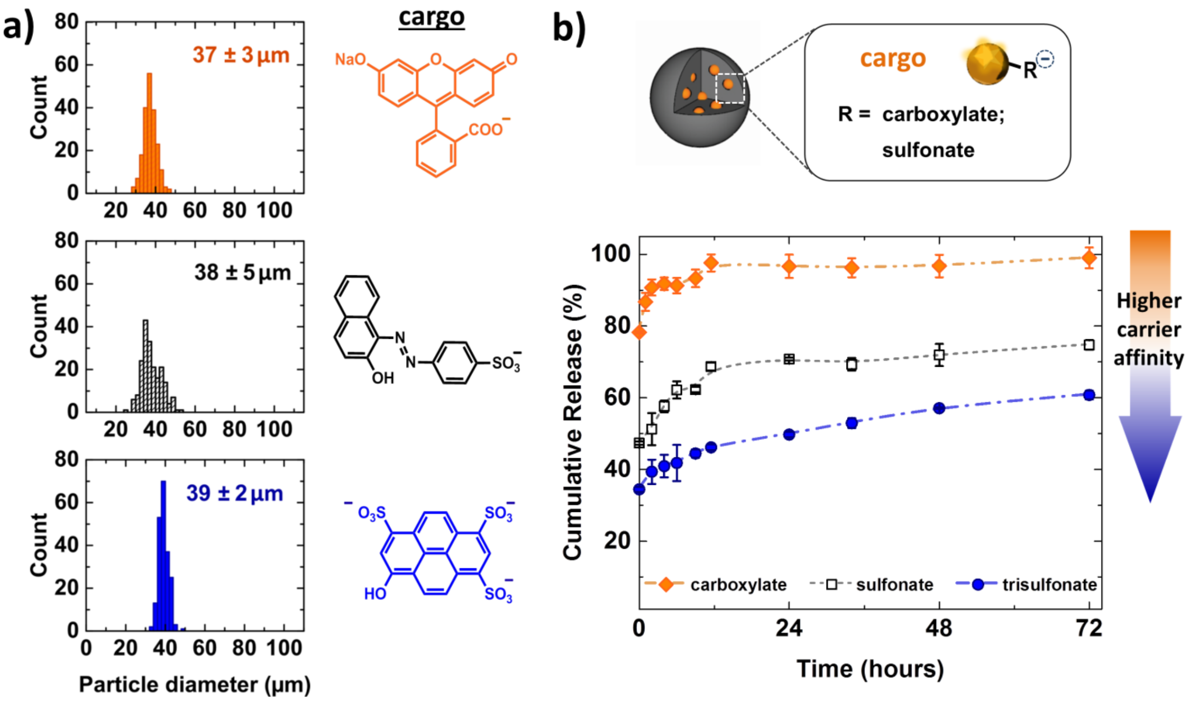

Figure 5.7. Release study for microgels containing payloads with different affinity for the carrier. a) Size distribution of microgels prepared with anionic dyes with different functional groups: fluorescein carboxylate, 4-(2-Hydroxy-1-naphthylazo) benzenesulfonate (orange II), and 8-hydroxypyrene-1,3,6 trisulfonate (pyranine). Histograms of particle size were generated from 200 particle measurements of microgel diameter in buffer. Scale bars are 100 µm. b) Cumulative release of payloads from different microgels over time. Release was calculated from normalized UV-Vis absorbance measurements, tracking the absorbance at 460 nm, 485 nm, and 465 nm for fluorescein, orange II, and pyranine respectively. Error bars represent standard error based on n=3 samples

These results demonstrate a clear dependence of the release profile on the electrostatic interaction between different cargos and one specific microgel carrier. While this enables the qualitative prediction of release rates for different payloads, it is similarly important to control the release rate of one specific compound by adjusting the carrier properties accordingly. This ability would significantly increase the versatility of these materials and thereby enhance their utility for biomedical applications.

5.2.5 Effect of carrier size on microgel release profile

A facile way to control the release rate is to vary the surface area of the microgel particles. Since the cargo release is governed by diffusion out of the microgel, a larger surface area to volume ratio was expected to lead to a faster release. [33,34] This hypothesis was tested by studying the release from different sized microgels containing 4.5 mol% of bound pyranine dye, incubated at 37 °C in buffer (

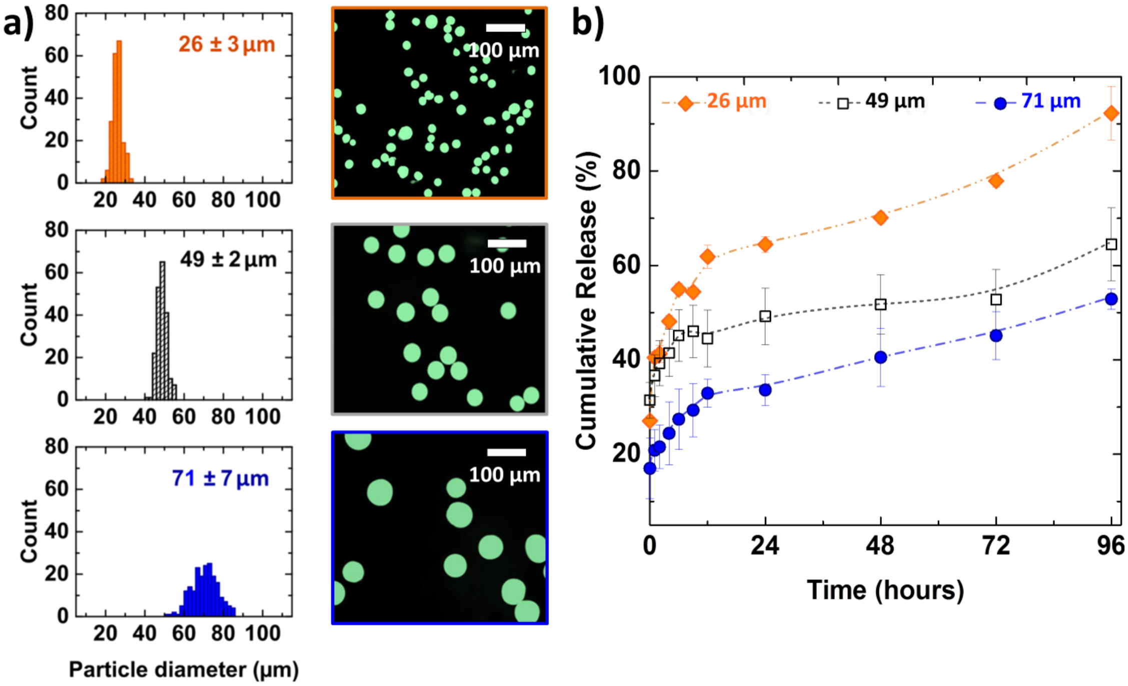

Figure 5.8). Microgels of different sizes (approx. 25, 50 and 70 µm) were obtained from microfluidic devices with the corresponding channel widths. Fluorescent images of the microgels in buffer demonstrate that the dye is well-distributed within the particles (Figure 4.8). The samples were incubated at 37 °C in PBS (pH 7.4, 10 mM) and aliquots were

removed at specific time points over four days. This release experiment protocol was similar to those previously described, except that the dye concentration was determined by fluorescence emission due to greater sensitivity than UV-vis absorbance.[35]

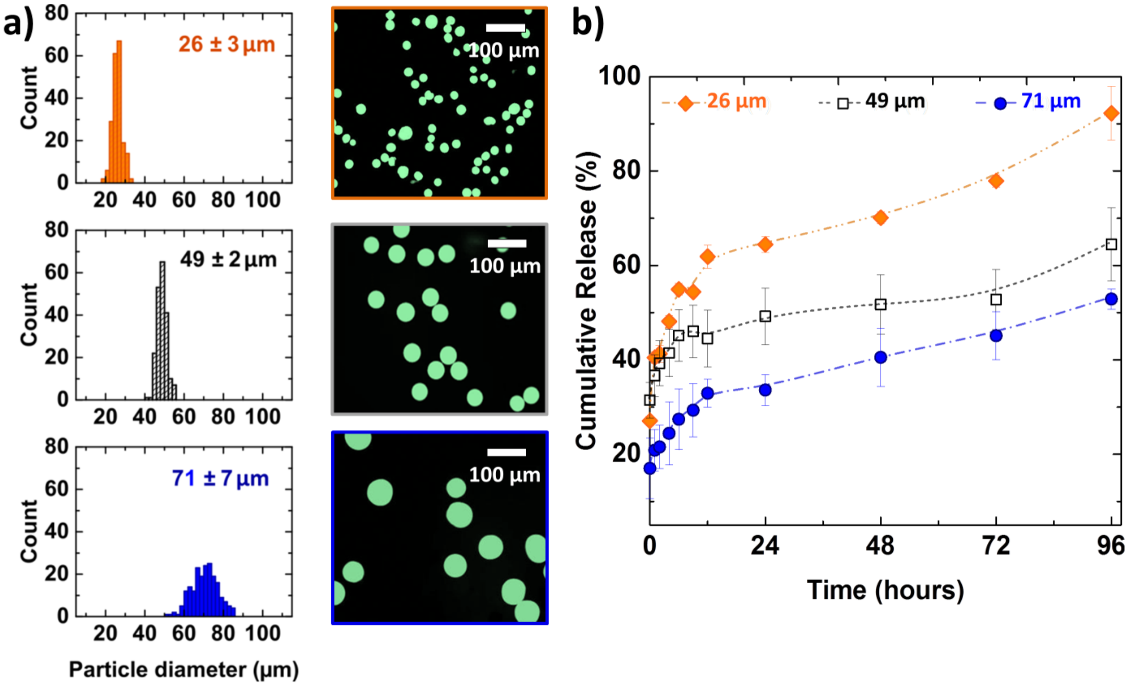

Figure 5.8. Release study for microgels containing (trisulfonate hydroxy pyrene) as a function of carrier size. a) Microgels of varying diameter are obtained from microfluidic devices with different channel widths. Each histogram of particle size was generated from 200 particle measurements. b) Fluorescent images of microgels and cumulative release of payload from microgels over time. The release was calculated based on the fluorescence emission values at 505 nm and excitation at 454 nm and the average values reported based on n=2 samples. Scale bars are 100 µm.

The cumulative release (amount of pyranine released from microgel normalized by initial amount of pyranine bound within the microgel at t=0) was calculated based on the fluorescence emission values at 505 nm and excitation at 454 nm. The fastest release was observed from the microgels with the smallest diameter (~25 μm) with 88% release of pyranine over 4 days, followed by the 50 μm microgels which reached 63% release of pyranine over 4 days. Finally, the slowest release of pyranine was observed at 53% release over 4 days from the 70 μm microgels. This trend indicates that the rate of release increases with higher surface area to volume ratio, and demonstrates the importance of size control for carriers with intended applications in controlled release.

5.3 Summary and Outlook

An efficient platform for microgel preparation was developed by combining the narrow particle size distribution that is accessible from microfluidics with a non-covalent crosslinking approach based on ionic coacervation. Bio-inspired mixing of two aqueous solutions of X-PEO-X triblock copolymers containing oppositely charged X end-blocks in a custom flow-focusing device allows robust particles with controlled size and stability to be obtained. The dynamic nature of the coacervate crosslinking domains enables the incorporation of functional small molecule payloads with a variety of anionic dyes being incorporated into the coacervates *via* electrostatic interaction. Distinct release profiles were dictated by the structure and ionic nature of the small molecules as well as by the microgel size. This new approach to microgel particles, based on mixing ionic triblock copolymers with ionic small molecules, represents a versatile and tunable strategy towards bio-inspired multicomponent scaffolds and delivery vehicles. Future directions involve the extension of microgel payloads from charged small molecules to also include bulky cargos entrapped within the PEO mesh to take advantage of this heterogeneous particle.

5.4 Experimental

5.4.1 Materials

Chemicals were purchased from Sigma-Aldrich and used as received unless otherwise stated. Millipore water (18.2MΩ·cm) was obtained from a buffer grade Milli-Q water purification system. Hydrochloric acid (12N, fuming 37%), sodium hydroxide (pellets), and phosphate buffer tablets were purchased from Fisher Scientific. X-PEO-X triblock copolymers with sulfonate (S-PEO-S) and guanidinium (G-PEO-G) functionalized end-blocks were prepared following a literature procedure (Scheme 4.1).[27] 1H,1H,2H,2H-Heptadecafluoro-1-decanol was obtained from Tokyo Chemical Industry (TCI). Novec 7500 Engineered Fluid was purchased from 3M, St. Paul, MN. Syringe pumps were manufactured by New Era, Farmingdale, NY. Polyethylene tubing with an outer diameter of 1.09 mm and an inner diameter of 0.38 mm was obtained from Scientific Commodities, Lake Havasa City, AZ.

5.4.2 Synthesis of polymers for microgel precursors

Synthesis of triblock copolymer microgel precursors: $P(AGE)_{35}$-b-$P(EO)_{227}$-b-$P(AGE)_{35}$ triblock copolymer was prepared by anionic ring-opening polymerization of allyl glycidyl ether (AGE) from a 10kDa PEO diol macroinitiator as previously reported.[13] M_n, GPC = 18 kDa, $Đ$: 1.1 (based on polystyrene calibrations).

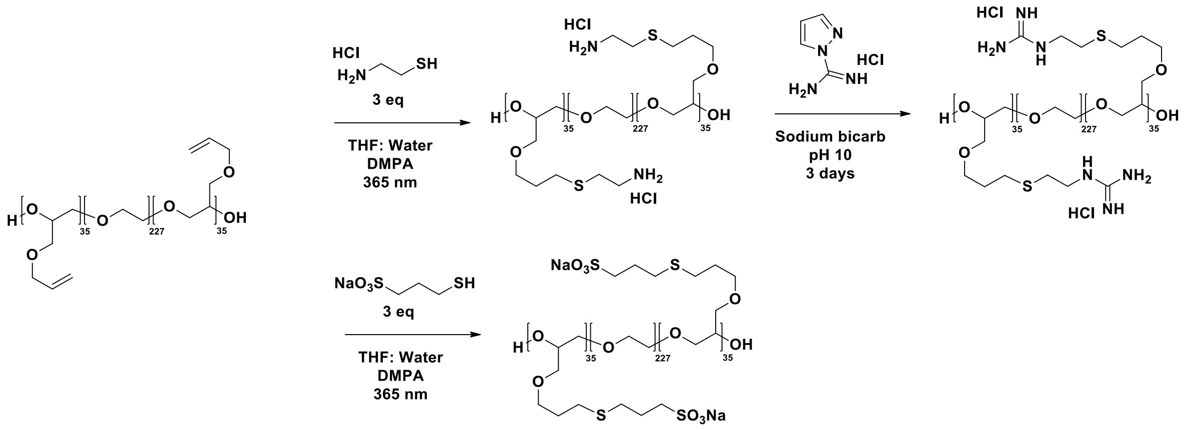

Scheme 4.1: Post functionalization of PAGE-PEO-PAGE to achieve ionic end blocks (G-PEO-G and S-PEO-S) via thiolene chemistry. Synthetic procedure based on literature reference.[13]

Synthesis of P(Guan)$_{35}$-b-P(EO)$_{227}$-b-P(Guan)$_{35}$ triblock copolymer: P(AGE)$_{35}$-b-P(EO)$_{227}$-b-P(AGE)$_{35}$ triblock copolymer (1.97 g, 7.7 mmol of alkene units) was dissolved in 100 mL THF and combined with cysteamine hydrochloride (2.76 g, 24.3 mmol, 3.2 eq per alkene) in 100 mL DI water, followed by 2,2-Dimethoxy-2-phenylacetophenone, DMPA (100 mg, 0.390 mmol, 0.05 eq per alkene) in a 250 mL RB flask with a stir bar and capped with a rubber septa. The mixture was degassed using argon for 30 min and irradiated under 365 nm light while stirring for 10 hours or until the reaction was complete by 1H-NMR ppm. THF was removed by rotary evaporation and the solution was dialyzed (MWCO: 3 kDa) in DI water to remove excess cysteamine salt. To convert the ammonium groups to guanidinium groups, the ammonium triblock was reacted with pyrazole carboximidamide hydrochloride (3.56 g, 24.4 mmol, 3.2 eq per ammonium group) in 150 mL solution buffered to pH 10 using sodium bicarbonate for 3 days at RT. The polymer was purified by dialysis (MWCO: 3 kDa) in DI water. The polymer was freeze dried to yield 2.37 g of light yellow solid (75 % yield).

^{1}H-NMR of P(Guan)$_{35}$-b-P(EO)$_{227}$-b-P(Guan)$_{35}$ triblock copolymer (500 MHz, D_2O reference set to δ_H*: 4.79* ppm) δ_H: copolymer 1.91 (m, 2H), 2.68 (t, 2H), 2.81 (t, 2H), 3.44 (t, 2H), 3.6–3.8 (br m, chain backbone and pendant ether groups) ppm.

Synthesis of P(Sulf)$_{35}$-b-P(EO)$_{227}$-b-P(Sulf)$_{35}$ triblock copolymer: Using similar reaction conditions as the ammonium triblock synthesis, the P(AGE)$_{35}$-b-P(EO)$_{227}$-b-P(AGE)$_{35}$ triblock polymer (2.10 g, 8.2 mmol of alkene units) in 100 mL THF was reacted with sodium 3-mercaptopropane-1-sulfonate (4.38 g, 24.5 mmol, 3 eq per alkene) in 100 mL DI water in a 250 mL RB flask with a stir bar. Then, 2,2-Dimethoxy-2-phenylacetophenone, DMPA (105 mg, 0.408 mmol, 0.05 eq per alkene) was added, the vessel capped and mixture degassed and irradiated under 365 nm light while stirring until reaction complete. After purification by dialysis, the polymer was freeze dried to yield 3.13 g of white solid (88 % yield).

^{1}H-NMR of P(Sulf)$_{35}$-b-P(EO)$_{227}$-b-P(Sulf)$_{35}$ triblock copolymer: (500 MHz, D_2O reference set to *4.79* ppm) δ_H: 1.95 (m, 2H), 2.09 (m, 2H), 2.73 (t, 2H), 2.78 (t, 2H), 3.09 (t, 2H), 3.6–3.8 (br m, chain backbone and pendant ether groups) ppm.

5.4.3 Preparation of microgels by microfluidic device with flow-focusing geometry

Device fabrication: Microfluidic flow focusing devices were fabricated following a literature procedure[10] to produce PDMS molds bonded to glass slides using soft lithography.[36] The device inner channels were treated with Aquapel to render the channel surface hydrophobic and favor aqueous droplet formation.[37] Devices with the same geometry but different channel widths (approximately 25, 40, 50 and 70 μm) were fabricated.

Microfluidic microgel generation: Four flow focusing devices with different channel widths were used to yield microgels with diameters approximately 25, 40, 50 and 70 μm. See Figure E4.1 for a representative device geometry (50 μm channels) containing flow resistors and a curved collection outlet. In the general procedure, aqueous solutions of microgel precursors (triblock copolymers) dissolved in ultra high purity MiliQ water were loaded into 1 mL syringes (BD Luer-Lok Disposable Syringes). Polyethylene tubing connected the syringes with the droplet device inlets. A mixture of 1 wt % surfactant, containing diblock copolymers of oligomeric perfluorinated polyether-*b*-poly(ethylene oxide), PFPE-PEO and triblock copolymer PFPE-PEO-PFPE in perfluorinated carbon oil (3M Novec 7500 Engineered Fluid) was used as the outer phase.[29] Flow rates, denoted by Q_{phase}, were controlled by syringe pumps, such that $Q_{polymer}/Q_{water}/Q_{continuous}$ were 60/30/600 μL hr^{-1}. The microgel dispersion was collected into vials and analyzed by optical microscopy.

Particle size analysis: For each histogram, the diameters of two hundred microgel particles were measured via ImageJ. Optical images were taken on a Nikon Eclipse E600 light microscope at 20x magnification. Fluorescent images of microgels loaded with hydroxypyrene trisulfonate (pyranine), were obtained on an Olympus BX 41 microscope with an objective lens at 10x magnification.

Concentration study: Approximately 5 wt %, 10 wt %, and 20 wt % polymer feed were used in the flow focusing microfluidic set up with 50 μm wide channels. The following flow rates were used (denoted by Q_{phase}) $Q_{polymer}/Q_{water}/Q_{continuous}$ at 60/30/600 μL hr^{-1}. Microgels could not be obtained from 20 wt % feed due to macroscopic gelation at the droplet junction. To transfer the gels from the oil phase into solution, fluorinated alcohol was added to reduce the surface tension of the perfluorinated oil (1 wt % heptadecafluoro-1-decanol in Novec 7500). 100μL of the microgel dispersion and 50μL of the fluorinated alcohol solution were transferred to a 500 μL solution of PBS buffer (10 mM, pH 7.4) at room temperature. At specific times, aliquots of this dispersion were dropcast between a cover slip and glass slide to obtain optical images.

Preparation of microgels loaded with dye: To maintain charge balance with the 10 wt % cationic polymer feed during microgel preparation, the following anionic feed solutions containing 10 mol % dye (relative to carrier), were used: 9.5 wt % sulfonate triblock with either 0.9 wt % fluorescein carboxylate or 0.85 wt % orange II; and 7.4 wt % sulfonate triblock with 1.3 wt % hydroxypyrene trisulfonate (pyranine).

5.4.4 Release experiments of dye loaded microgels

Encapsulation efficiency of microgels loaded with dye: Encapsulation efficiency was calculated as the percent of mass of dye remaining in the microgels after rinsing, relative to the mass of dye loaded. Specifically, 100μL of the microgel dispersion and 50 μL of 1 wt % fluorinated alcohol solution were mixed and transferred to a 1 mL solution of deionized water to remove unbound dye. The concentration of unbound dye in the solution and concentration of dye remaining/bound in the microgels were determined by UV-Vis absorbance measurements. Absorbance of Fluorescein: λ = 460 nm; Orange II: λ = 485 nm, Pyranine: λ = 465 nm.

To determine the amount of encapsulated dye, the centrifuged microgels were redispersed in water and then disintegrated by breaking the ionic coavervate crosslinks. In the case of microgels containing fluorescein or pyranine, this was achieved by adding 2M NaOH to the microgel dispersion to adjust the pH to 12. The resulting solution was investigated by UV-Vis and the absorbance of the respective dye was compared to a corresponding calibration curve at the same basic pH (see SI). This gave the mass of encapsulated dye. It is noteworthy that for breaking the microgels, the addition of base was selected over acid due to the reduced fluorescence signal of fluorescein and pyranine under acidic pH. Conversely, orange II dye was more susceptible to oxidation under basic conditions so microgels containing orange II dye were subject to acidic conditions to disrupt the network and liberate the incorporated dye. Here, 2M HCl was added to the microgel dispersion to adjust the pH to 1. To calculate the mass of embedded dye, the corresponding calibration curves of orange II at the same acidic pH were measured (see SI).

Based on these values, the encapsulation efficiency of these microgels were calculated as follows: 47±7% for fluorescein, 43±5% for orange II, and 45±3% for pyranine; based on n=3 samples.

Release experiments with microgels containing dye: 100μL of the microgel dispersion and 50 μL of 1 wt % fluorinated alcohol solution were mixed and transferred to a 1 mL solution of deionized water to remove unbound dye. Next, this dispersion was centrifuged and transferred to 10 mL solution of PBS buffer 10 mM at 37 °C for several days.

At specified time points, 250 μL aliquots were removed from the solution and centrifuged at 4000 rpm, for 3 minutes. The concentration of dye released into the supernatant was measured by UV-Vis or Fluorescence spectroscopy in a plate reader. (Absorbance of

Fluorescein: λ = 460 nm; Orange II: λ = 485 nm, Pyranine: λ = 465 nm; and fluorescence of Pyranine: $\lambda_{excitation}$ = 454 nm, $\lambda_{emission}$ = 515 nm)

The percentage of dye released at a specific time point was calculated by normalizing the concentration of the dye in the supernatant with that of the total dye within the microgel, following a literature protocol.[1]

5.5 References

1. Murthy, N.; Xu, M.; Schuck, S.; Kunisawa, J.; Shastri, N.; Frechet, J. M. J. **2003**, *Proc. Natl. Acad. Sci. 100*, 4995–5000.
2. Eichenbaum, G. M.; Kiser, P. F.; Dobrynin, A. V.; Simon, S. A; Needham, D. *Macromolecules* **1999**, *32*, 4867–4878.
3. Steinhilber, D.; Rossow, T.; Wedepohl, S.; Paulus, F.; Seiffert, S.; Haag, R. *Angew. Chem. Int. Ed. Engl.* **2013**, *52*, 13538–13543.
4. Slaughter, B. V; Khurshid, S. S.; Fisher, O. Z.; Khademhosseini, A.; Peppas, N. A. *Adv. Mater.* **2009**, *21*, 3307–3329.
5. Das, M.; Zhang, H.; Kumacheva, E. *Annu. Rev. Mater. Res.* **2006**, *36*, 117–142.
6. Lyon, L. A.; Fernandez-Nieves, A. *Annu. Rev. Phys. Chem.* **2012**, *63*, 25–43.
7. Klinger, D.; Landfester, K. *Polym. (United Kingdom)* **2012**, *53*, 5209–5231.
8. Duncanson, W. J.; Lin, T.; Abate, A. R.; Seiffert, S.; Shah, R. K.; Weitz, D. A. *Lab Chip* **2012**, *12*, 2135–2145.
9. Seiffert, S. *Angew. Chemie Int. Ed.* **2013**, *52*, 11462–11468.
10. Utech, S.; Prodanovic, R.; Mao, A. S.; Ostafe, R.; Mooney, D. J.; Weitz, D. a. *Adv. Healthc. Mater.* **2015**, *4*, 1628–1633.
11. Bradley, M.; Grieser, F. *J. Colloid Interface Sci.* **2002**, *251*, 78–84.
12. Loxley, A.; Vincent, B. *Colloid Polym. Sci.* **1997**, *275*, 1108–1114.
13. Kumacheva, E.; Garstecki, P. *Microfluidic Reactors for Polymer Particles*; John Wiley & Sons, Ltd:

New York, 2011.

14. Tumarkin, E.; Kumacheva, E. *Chem. Soc. Rev.* **2009**, *38*, 2161–2168.
15. Fitzgerald, P. A.; Amalvy, J. I.; Armes, S. P.; Wanless, E. J. *Langmuir* **2008**, *24*, 10228–10234.
16. Wang, L. Y.; Ma, G. H.; Su, Z. G. *J. Control. Release* **2005**, *106*, 62–75.
17. Cohen, B.; Pinkas, O.; Foox, M.; Zilberman, M. *Acta Biomater.* **2013**, *9*, 9004–9011.
18. Kim, J. H.; Jeon, T. Y.; Choi, T. M.; Shim, T. S.; Kim, S.-H.; Yang, S.-M. *Langmuir* **2014**, *30*, 1473–1488.
19. Zhang, H.; Tumarkin, E.; Peerani, R.; Nie, Z.; Sullan, R. M. A.; Walker, G. C.; Kumacheva, E. *J. Am. Chem. Soc.* **2006**, *128*, 12205–12210.
20. Zhou, X.; Liu, B.; Yu, X.; Zha, X.; Zhang, X.; Chen, Y.; Wang, X.; Jin, Y.; Wu, Y.; Chen, Y.; Shan, Y.; Chen, Y.; Liu, J.; Kong, W.; Shen, J. *J. Control. Release* **2007**, *121*, 200–207.
21. Rossow, T.; Heyman, J. A.; Ehrlicher, A. J.; Langhoff, A.; Weitz, D. A.; Haag, R.; Seiffert, S. *J. Am. Chem. Soc.* **2012**, *134*, 4983–4989.
22. Sikorski, P.; Mo, F.; Skjåk-Bræk, G.; Stokke, B. T. *Biomacromolecules* **2007**, *8*, 2098–2103.
23. Waite, J. H.; Andersen, N. H.; Jewhurst, S.; Sun, C. *J. Adhes.* **2005**, *81*, 297–317.
24. Srivastava, A.; Waite, J. H.; Stucky, G. D.; Mikhailovsky, A. *Macromolecules* **2009**, *42*, 2168—2176.
25. Shao, H.; Stewart, R. J. *Adv. Mater.* **2010**, *22*, 729–733.
26. Hwang, D. S.; Zeng, H.; Srivastava, A.; Krogstad, D. V; Tirrell, M.; Israelachvili, J. N.; Waite, J. H. *Soft Matter* **2010**, *6*, 3232–3236.
27. Hunt, J. N.; Feldman, K. E.; Lynd, N. A.; Deek, J.; Campos, L. M.; Spruell, J. M.; Hernandez, B. M.; Kramer, E. J.; Hawker, C. J. *Adv. Mater.* **2011**, *23*, 2327–2331.
28. Inoue, K.; Takeuchi, Y.; Miki, D.; Odo, S.; Harayama, S.; Waite, J. H. *Eur. J. Biochem.* **1996**, *239*, 172–176.
29. Holtze, C.; Rowat, A. C.; Agresti, J. J.; Hutchison, J. B.; Angilè, F. E.; Schmitz, C. H. J.; Köster, S.; Duan, H.; Humphry, K. J.; Scanga, R. A.; Johnson, J. S.; Pisignano, D.; Weitz, D. A. *Lab Chip* **2008**, *8*, 1632–1639.
30. Song, H.; Tice, J. D.; Ismagilov, R. F. *Angew. Chemie, Int. Ed. English* **2003**, *42*, 768–772.
31. Zhang, B.; Tao, H.; Wei, B.; Jin, Z.; Xu, X.; Tian, Y. *PLoS One* **2014**, *9*, e114634.

32. Costa, E.; Lloyd, M. M.; Chopko, C.; Aguiar-Ricardo, A.; Hammond, P. T. *Langmuir* **2012**, *28*, 10082–10090.
33. Yang, C. C.; Huang, K. S.; Chang, J. Y. *Biomed. Microdevices* **2007**, *9*, 253–259.
34. Xu, Q.; Hashimoto, M.; Dang, T. T.; Hoare, T.; Kohane, D. S.; Whitesides, G. M.; Langer, R.; Anderson, D. G. *Small* **2010**, *5*, 1575–1581.
35. Fedosov, S. N.; Brask, J.; Xu, X. *J. Am. Oil Chem. Soc.* **2012**, *89*, 2155–2163.
36. Xia, Younan; Whitesides, G. M. *Angew. Chemie - Int. Ed.* **1998**, *37*, 550–575.
37. Seo, M.; Paquet, C.; Nie, Z.; Xu, S.; Kumacheva, E. *Soft Matter* **2007**, *3*, 986.

6 Conclusion and Outlook

Drawing from the design principles used by nature to assemble robust and complex nanostructures, three bioinspired assembly methods for polymeric nanomaterials were presented. The chemical versatility and ease of processing of synthetic polymers makes them attractive building blocks for tunable thin films and nanoparticles.

In the first system, a catechol functionalized polyacrylamide binder was used to prepare robust multilayered nanocomposite coatings on a variety of substrates. The catechol group, a key component in the adhesive mussel foot proteins of the marine mussel, enabled incorporation of SiO_2 and TiO_2 nanoparticles. Existing literature supports our assumption that the catechol group can undergo hydrogen bonding or form a metal transfer complex to coordinate with these oxide materials. Layer-by-layer assembly of the binder and nanoparticles enabled control over the thickness and refractive index of composite thin films. These composites were resistant to organic solvent and stable against degradation under acidic and basic solutions over the course of days.

In the second system, a mixture of surfactants was used to direct the orientation of block copolymer domains relative to a droplet interface. Solvent evaporation based assembly of PS-b-P2VP in the presence of binary mixtures of surfactants yielded spherical “onion”-like particles in the case of preferential wetting conditions, and conversely under non-preferential wetting conditions particles with an axially-stacked lamellae morphology were produced. In the latter case, we observed particle elongation into ellipsoids, where the BCP particle aspect ratio could be tuned by the BCP molecular weight.

Selective, covalent cross-linking of the P2VP domains after ellipsoidal particle assembly, enabled the fabrication of pH responsive swelling of the 2VP domains. Under acidic conditions, dispersions of the crosslinked particles appear iridescent. This motivated us to pursue the fabrication of larger ellipsoidal nanoparticles using a simplified extrusion set up to assemble PS-P2VP. Besides interfacial engineering to direct the BCP phase separation, other important parameters to achieve the desired morphology include the ratio of droplet to continuous phase and rate of solvent evaporation to avoid kinetically trapped particle structures. The results presented are promising for future development of stimuli responsive photonic colloids that could find application for low energy displays. Narrow particle size distributions will be important in order to prepare ellipsoids containing similar numbers of internal “Bragg stacks” for finer control over reflectivity and particle packing or alignment. However, the use of chloroform droplets and charged surfactants for particle assembly make it challenging to apply standard microfluidic techniques used to generate uniform droplets. To address this, our collaborators in the Soh Lab are pursuing purification strategies of our assembled particles using an integrated microfluidic platform that combines high speed microscopy with automated image analysis to sort particles by size and shape.

Finally, well defined microgels with controlled size and stability were produced by ionic crosslinking of two PEO based triblock copolymers within a microfluidic device. Microfluidic flow focusing enabled model cargo to be loaded into these microgels carriers. These functional payloads consist of anionic dyes that associate with the polyelectrolyte domains within the gel. By varying the cargo affinity for the carrier network, either through different functional groups on the dye or varying the ionic strength of the media, we observed different cargo release profiles. Microgel dimensions may also be used to tune diffusion of the cargo, as higher surface area to volume ratio (smaller particle dimensions) accelerated dye release from particles. This work may serve as a model release system for future development in controlled delivery.

Potential directions for this work include extension of microgel payloads to encapsulate bulky, neutral cargo within the PEO mesh. Based on our hypothesis that the charged small molecules segregate into coacervate domains within the microgel, simultaneous incorporation of bulky cargo would result in a dual component delivery vehicle with independent cargo release rates. Engineering such multicomponent vehicles would expand microgels from simple structural supports into programmable scaffolds for biomedical research.

Collectively, all the strategies presented in this work represent simple and scalable methods to access nanostructured polymeric thin films and colloidal materials for a wide range of applications.

7 Appendix

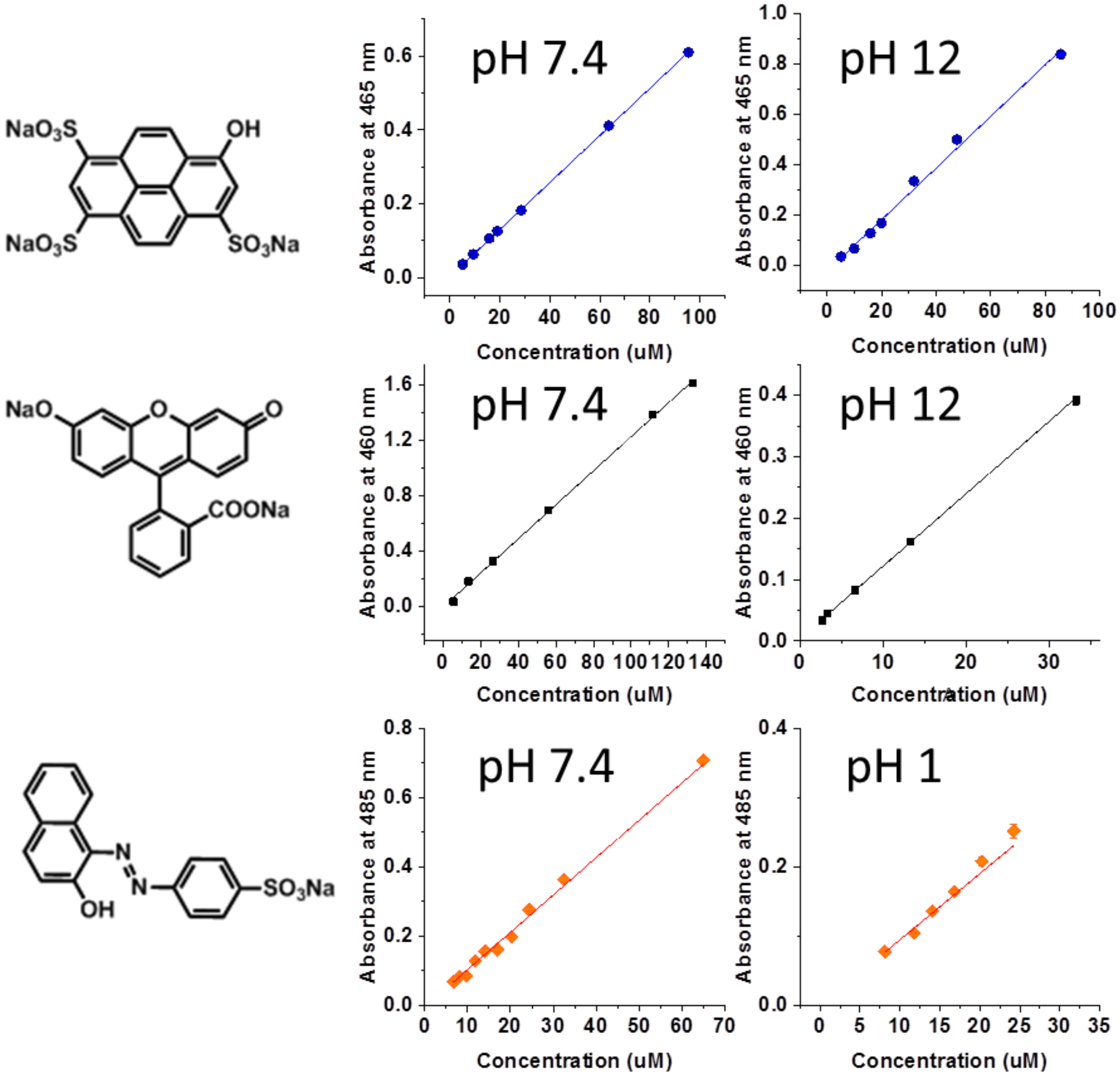

Figure 7.1. Calibration curves used to determine amount of dye in supernatant and degraded microgels in 10 mM PBS buffer. The stock solutions for pH 12 were prepared by the addition of 2 M NaOH to adjust the pH of fluorescein or HPTS? stock solutions and the solutions for pH 1, by addition of 2 M HCl to adjust the pH of orange II solutions. The samples were prepared in triplicate and the average absorbance plotted against concentration.

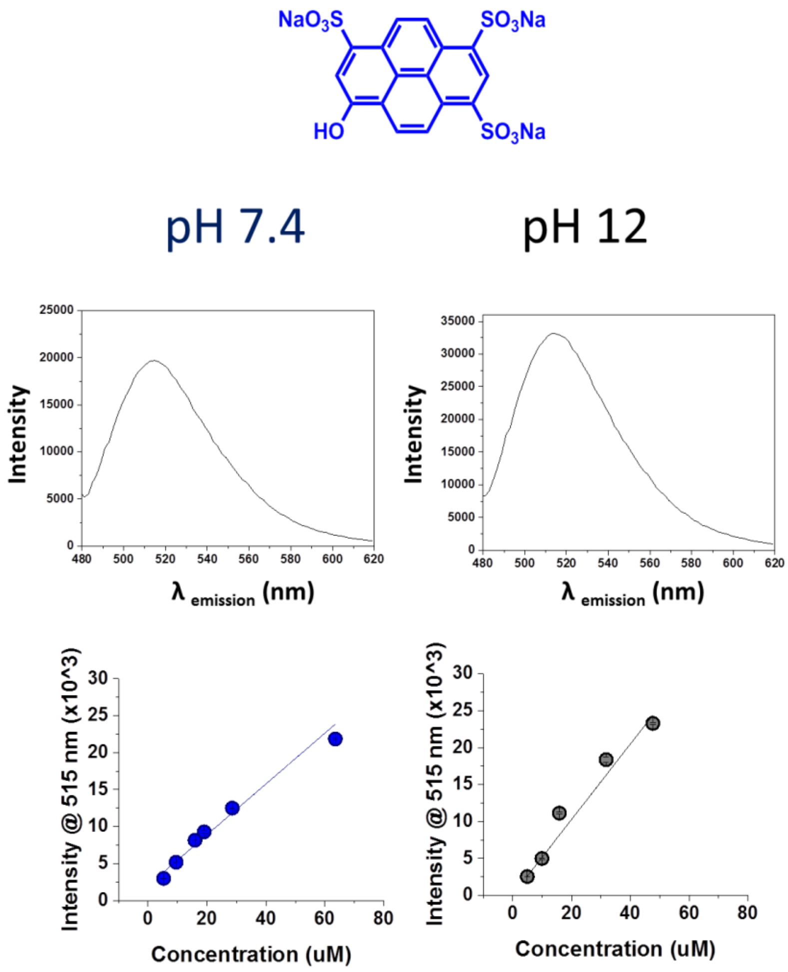

Figure 7.3. Fluorescence emission of pyranine and calibration curves.